NUMERICAL METHODS FOR SINGLE-PHASE AND TWO-PHASE FLOWS

A Thesis

Submitted to the Faculty

of

Purdue University

by

Sri Harsha Challa

In Partial Fulfillment of the

Requirements for the Degree

of

Master of Science

December 2018

Purdue University

West Lafayette, Indiana

THE PURDUE UNIVERSITY GRADUATE SCHOOL
STATEMENT OF THESIS APPROVAL

Dr. Suchuan Dong, Co-chair

Department of Mathematics

Dr. Gregory A. Blaisdell, Co-chair

School of Aeronautics and Astronautics

Dr. Tom I. Shih

School of Aeronautics and Astronautics

Dr. Arezoo M. Ardekani

School of Mechanical Engineering

Approved by:

Dr. Tom I. Shih

Head of the Departmental Graduate Program

Dedicated to my parents Lakshmi Narasaiah Challa and Sailaja Bandreddy, and my brother Phani Kiran Challa.

ACKNOWLEDGMENTS

First and foremost, I would like to thank Professor Suchuan Dong, for his support and guidance throughout the last two years which helped me in completing this thesis. I am also grateful to my other thesis committee members - Professor Gregory Blaisdell, Professor Tom Shih, and Professor Arezoo Ardekani- for their time and inputs on my thesis and research.

Lastly, I would also like to thank my family and my friends for their constant support and encouragement.

The research carried out in this thesis was partially supported by NSF DMS-1318820 and DMS-1522537.

TABLE OF CONTENTS

LIST OF TABLES

LIST OF FIGURES

Figure Page

ABSTRACT

M.S, Purdue University, December 2018. Numerical methods for single-phase and two-phase flows. Major Professor: Suchuan Dong. Professor.

Incompressible single-phase and two-phase flows are widely encountered in and underlie many engineering applications. In this thesis, we aim to develop efficient methods and algorithms for numerical simulations of these classes of problems. Specifically, we present two schemes: (1) a modified consistent splitting scheme for incompressible single-phase flows with open/outflow boundaries; (2) a three-dimensional hybrid spectral element-Fourier spectral method for wall-bounded two-phase flows.

In the first part of this thesis, we present a modified consistent splitting type scheme together with a family of energy stable outflow boundary conditions for incompressible single-phase outflow simulations. The key distinction of this scheme lies in the algorithmic reformulation of the viscous term, which enables the simulation of outflow problems on severely-truncated domains at moderate to high Reynolds numbers. In contrast, the standard consistent splitting scheme is observed to exhibit a numerical instability even at relatively low Reynolds numbers, and this numerical instability is in addition to the backflow instability commonly known to be associated with strong vortices or backflows at the outflow boundary. Extensive numerical experiments are presented for a range of Reynolds numbers to demonstrate the effectiveness and accuracy of the proposed algorithm for this class of flows.

In the second part of this thesis, we present a numerical algorithm within the phase-field framework for simulating three-dimensional (3D) incompressible two-phase flows in flow domains with one homogeneous direction. In this numerical method, we represent the flow variables using Fourier spectral expansions along the homogeneous direction and C^0 spectral element expansions in the other directions. This is

followed by using fast Fourier transforms so that the solution to the 3D problem is obtained by solving a set of decoupled equations about the Fourier modes for each flow variable. The computations for solving these decoupled equations are performed in parallel to efficiently simulate the 3D two-phase flows. Extensive numerical experiments are presented to demonstrate the performance and the capabilities of the scheme in simulating this class of flows.

1. INTRODUCTION

1.1 Incompressible Single-Phase Flows with Open Boundaries

The development of numerical methods for simulating single-phase flow problems in unbounded domains has become an important research topic over the past few decades [1–5]. These type of flow situations commonly occur in wakes behind bluff bodies, fluid jets, pipe flows, and boundary layers. The motion of the unsteady, viscous, incompressible single-phase flows can be described mathematically by the Navier-Stokes equations, which are a system of partial differential equations based on the conservation laws of mass, momentum, and energy. Directly solving this system of equations is computationally expensive as the velocity and the pressure variables in these equations are coupled together by the incompressibility constraint. Also, to perform numerical simulations of physically unbounded flows, we need to truncate the domain to a finite size by using artificial boundaries. These artificial boundaries are referred to as the open or outflow boundaries. However, if we merely restrict the domain size, we end up compromising the accuracy of the results as well as the stability of the computations. To obtain computationally efficient simulations of this class of flow problems, we need: (1) a numerical scheme which decouples the computations of different flow variables (velocity and pressure) in the Navier-Stokes equations; (2) efficient boundary conditions on the outflow boundary which provide stable computations and give accurate results.

1.1.1 Projection Methods

The projection methods are the prominently discussed class of schemes for decoupling the calculations of the flow variables. These schemes are time-discretization

methods of the Navier-Stokes equations. The idea behind these schemes is to account for the viscous effects and the incompressibility of the flow in two sub-steps within a time step. The first projection schemes can be dated back to about five decades and have been introduced independently in [6] and [7]. These schemes stimulated the interest of the researchers in this area, and many modifications were proposed over the past few decades to improve the accuracy of the results. These modifications led to three sub-classes of the projection schemes namely pressure-correction schemes [2, 8–13], velocity-correction schemes [3, 11, 14] and consistent splitting schemes [15, 16]. In the pressure-correction schemes we compute an auxiliary velocity by treating the pressure explicitly in the first sub-step and then correct the pressure in the second sub-step [15]. In the velocity-correction schemes, we make the viscous term explicit in the first sub-step and then correct the velocity in the second sub-step [17]. Although the pressure-correction and velocity-correction schemes successfully decouple the calculations of the velocity and pressure, they can only provide either first-order or 3/2-order accuracy in time on the L^2-norm for the vorticity and pressure on general flow domains [11, 17–19]. The consistent splitting schemes have been developed to overcome this issue in [15]. In these schemes, the pressure is treated explicitly in the first sub-step, and it is updated by solving a Poisson equation in the weak form in the second sub-step. These schemes are free of splitting errors and are capable of providing second-order accuracy in the L^2-norm for the velocity, pressure and the vorticity.

However, the standard consistent splitting scheme is observed to be computationally unstable for simulating moderate to high Reynolds number flows [16]. A two-level consistent splitting scheme was proposed in [16] to overcome this difficulty. In this scheme, a non-linear equation is solved in a coarser mesh and a linear problem is solved in a finer mesh in the first sub-step and the pressure is updated by solving a Poisson equation in the second sub-step. An interesting property of this scheme is that it is computationally more efficient than the standard consistent splitting scheme. However, this scheme has a first order convergence rate in time. In [20], a projection

scheme based on a consistent splitting strategy has been developed by enforcing a divergence-free condition on the velocity after the first sub-step. This scheme was demonstrated to have an improved convergence rate in time. However, this scheme alone fails to provide stable computations at high Reynolds numbers.

1.1.2 Outflow Boundary Conditions

Over the past few decades, researchers have proposed several outflow boundary conditions for single-phase flows with open boundaries. The commonly used open boundary conditions are the convective boundary condition [21–25] and the traction-free condition [18, 26–31]. However, the convective boundary condition and the traction-free condition fail to provide stable computations at moderate to high Reynolds numbers. The reason for this is the backflow instability. It is a numerical instability associated with strong vortices or backflows at the open boundary which makes the computations unstable, and the simulations blow up instantly [32–34]. Some ways to deal with this issue are to use a large computational domain or coarsen the grid in the wake region so that the vortices are dissipated before they reach the outflow boundary [33]. However, this approach is not efficient because at high Reynolds numbers the computational domain needed will become extremely large and the computational cost increases significantly. An efficient approach is to develop outflow boundary conditions which can tackle the issue of backflow instability.

A convective-like energy-stable open boundary condition has been proposed in [3] to overcome the backflow instability at high Reynolds numbers. We use this open boundary condition in this thesis. The principal advantage of using this outflow boundary condition is that it provides control over the velocity on the outflow boundary by limiting the upper bound of the total energy. We refer the reader to [2, 34–37] for details about other boundary conditions to deal with backflow instability.

In this thesis, we aim to develop a consistent splitting type numerical algorithm to decouple the computations of the flow variables in the Navier-Stokes equations together with the convective-like energy-stable outflow boundary condition.

1.2 Incompressible Two-Phase Flows

The second part of this thesis focuses on the incompressible two-phase flows. Particularly, we consider the two-phase flows which deal with the motion of two immiscible fluids in three-dimensional domains with one homogeneous direction. This class of two-phase flows can be observed in flow configurations where the boundary effects of the domain are negligible in one direction (e.g., flow through pipelines, channels). We aim to use this homogeneity property to develop a numerical method which can efficiently compute three-dimensional simulations for two-phase flows.

When the two immiscible fluids come in contact with each other, a common boundary is formed between them, and this boundary is called an interface. The interactions of the fluid-fluid interface with a solid wall are commonly studied phenomena [38, 39]. A moving contact line is formed when the fluid-fluid interface of the two-phase flow system comes in contact with a solid wall. We need a mathematical model which can describe the motion of interface to numerically simulate the contact line problem. In classical hydrodynamics the fluid-fluid interface is assumed to be a narrow zone of zero-thickness (sharp interface model) across which the density and the tangential velocity are discontinuous and a no-slip condition is used at the interface. However, this assumption is not valid when the order of the length scales are comparable to the interface thickness which is usually the case when topological changes occur in the interface [40]. Due to this reason, the numerical simulations of contact line problems using the sharp interface model are complicated by an unbounded stress tensor, which can give rise to an unbounded shear force near the contact line [40]. The current numerical models can be broadly classified into two categories: (1) interface-capturing methods such as volume of fluids [41–43], level

set [44–46] and phase field approach [47–49], and (2) interface tracking methods such as the front tracking method [50–52] are developed for dealing with contact line problems. We use a phase field based approach in this thesis as this approach is physically motivated and can account for topological changes of the interface [47, 48, 53, 54].

1.2.1 Phase Field Approach

The idea that interface has a finite thickness was first discussed in [55] and [56]. In [56], it was suggested that based on the thermodynamic equilibrium at the contact line the two immiscible fluids do mix at molecular levels so that they are in a steady state of motion and not at a state of rest. These ideas have formed the basis for the phase-field approach.

In the phase field approach, we replace the sharp fluid interface with a diffuse-interface and a phase field function is used to represent the two-phase system. This field function has a unique value in the bulk of each different fluid and it varies continuously over the diffuse interface with values bounded between the unique values of the different fluids. Cahn and Hilliard [57] used the concept of the diffuse interface to derive equations for the free energy of the system. In [47,48] an energetic variational formulation has been used to derive Cahn-Hilliard phase field models for the two-phase system. In this model, the governing equations for the two-phase system are obtained by taking the effect of the coupling between the diffusion and the mechanics of the flow (i.e, coupling the Cahn-Hilliard equation with the Navier-Stokes) by the introduction of an extra stress term to the momentum equation and a transport term to Cahn-Hilliard equation.

Many numerical algorithms have been proposed to solve the coupled system of Cahn-Hilliard and Navier-Stokes equations [47, 58–62]. However, these models assume that the densities of the two flows are either equal or very small and therefore these schemes cannot simulate flows with large density ratios. In [63], an energy stable scheme has been presented for two-phase flows with variable densities. An important

point to be noted is that the mixture viscosity and the mixture density (for variable density methods) in the coupled Cahn-Hilliard and Navier-Stokes equations are dependent on the phase-field function. Since the phase-field function varies with time, the mixture viscosity and density are also time-dependent. The coefficient matrices of the algebraic systems for the pressure and velocity in the methods specified above contain the mixture density and viscosity terms and are therefore time-dependent. These coefficient matrices have to be updated at every time step and this causes computational performance issues. In [53], the pressure and the viscous terms in the momentum equations have been reformulated in a way such that these coefficient matrices are time-independent. However, the numerical method in [53] has been implemented using C^0 spectral elements for spatial discretization in all directions and the simulation of three-dimensional problems will be computationally expensive.

1.3 Objectives of this thesis

In the context of the single-phase flows, the objective of this thesis is *to develop a numerical algorithm for simulating single-phase flows with outflow boundaries at high Reynolds numbers*. The main idea relies on the reformulation of the viscous term together with the consistent splitting strategy [15] and the choice of the outflow boundary condition [3] which enables simulations at high Reynolds numbers in the presence of strong vortices or backflows at the outflow boundary. The proposed numerical algorithm is implemented using C^0 spectral elements for the spatial discretization.

In the context of two-phase flows, the objective of the thesis is *to develop a numerical algorithm for efficiently simulating three-dimensional two-phase flows in flow domains with one homogeneous direction*. The main idea relies on the strategy presented in [53] to obtain constant coefficient terms in the differential equations after time-discretization of the governing equations, thus enabling the use of fast Fourier transforms to reformulate the three-dimensional (3D) problem into a set of decoupled

two-dimensional problems about the Fourier modes. The computations for the solutions of these decoupled two-dimensional problems can be performed efficiently by using parallel processors. We use Fourier spectral method for the spatial discretization along the homogeneous direction and C^0 spectral elements in the other directions. We have also imposed the static contact angle boundary conditions according to the methods proposed in [38, 54, 64].

1.4 Spectral Element Methods - An Overview

In this section, we briefly discuss the background and salient features of the spectral element method for the spatial discretization of the governing equations (both single-phase and two-phase flows) in this thesis.

Finite element methods divide the domain into a number of smaller sub-domains (elements) and the weak formulation of the original differential equation is solved in each sub-domain. The smaller sub-domains are referred to as finite elements. The variational method (weak form) to approximate the partial differential equation in each sub-domain has been introduced in [65]. Each sub-domain is then assembled together by an automatic process called *global assembly*.

A large number of research contributions to the field of finite element methods have been made in the context for analyzing linear plane elasticity problems in the 1960s [66]. Most of these methods used a low order polynomial expansion(linear or quadratic) as the basis functions and have been used in the field of computational aerodynamics which involves complex geometries and unstructured meshes.

The requirement of accurate resolution of vortex structures and the boundary layers paved the way for high-order discretization methods. Spectral methods are similar to finite-element methods, but in this case, the domain is not divided. Instead, the solution to the partial differential equation is approximated by a truncated series expansion throughout the domain using global basis functions which consist of high-order polynomials. However, these methods create difficulties in handling

complex geometries. To overcome this issue, spectral element methods were developed in [67]. These methods use the best features of both the finite element methods and the spectral methods i.e., in spectral element method the domain is divided into a number of sub-domains which are referred to as spectral elements and the functions are approximated using series expansions whose basis are high-order orthogonal polynomials. This enables the representation of complex geometries using unstructured meshes and also to obtain accurate solutions to problems which require high resolutions as mentioned above. The usual basis functions for the spectral element methods are Legendre polynomials [68] because of the inherent orthogonality property [66] and increasing the order of the polynomials in the basis functions increases the overall accuracy, however, the disadvantage is increased computational cost.

The selection of proper basis functions for the spectral element method is required to increase computational efficiency and stability. In general, the expansion basis with a low condition number and better sparsity of the system matrix (both mass matrix and the stiffness matrix) are considered to be efficient [69, 70] as they result in faster convergence. For example, when the basis functions using Legendre polynomials are used in structured elements the resultant stiffness matrix is a diagonal matrix which is a good choice. However, for unstructured grid elements, the condition number of the system matrix increases exponentially as we increase the element order [70] which is not a desired property. Over the past few decades, several bases been developed to improve the sparsity of the system matrix as well as the conditioning of elemental and global matrix. A review of different bases and their properties of conditioning and sparsity of the system matrix has been presented in [71]. Also, in [71] an eigen-based expansion basis has been developed for spectral element methods which involve structured elements (quadrilateral in 2D and hexahedral in 3D) and it was demonstrated that using this basis results in a weak relationship between the number of iterations to converge and the element order i.e., we can use high element orders for the basis functions and still get the converged results in a reasonable time unlike other traditional bases. This basis was also compared with several other bases and was shown

to be numerically efficient. For the spectral element discretization in this thesis, we use Jacobi polynomial-based expansion basis [66] and the NekTar spectral element solver library [72].

1.5 Outline of this thesis

The organization of this thesis is as follows:

- In Chapter 2, we first discuss the governing equations for the incompressible single-phase flows and the energy-stable outflow boundary condition. We then present the modified consistent-splitting scheme and its implementation using C^0-continuous high order spectral element methods. Further, to demonstrate the capabilities of this scheme, we present numerical tests for single-phase incompressible flows with open boundaries for several Reynolds numbers.

- In Chapter 3, we first discuss the governing equations for the two-phase system using phase field approach and the existing numerical algorithm for solving this system of equations. Then we present the hybrid spectral element-Fourier spectral method for the spatial discretization of the governing equations. Further, to demonstrate the performance of the proposed spatial discretization technique, we present several numerical tests for various two-phase flow problems.

- Finally concluding remarks and future research direction are presented in Chapter 4.

2. MODIFIED CONSISTENT SPLITTING SCHEME FOR SINGLE-PHASE FLOWS WITH OPEN/OUTFLOW BOUNDARIES

2.1 Governing Equations and Outflow boundary condition

In this section, we briefly discuss the governing equations which describe the motion of single-phase incompressible flows and the convective-like outflow boundary condition imposed at the open boundary.

For the context of this chapter, we use Ω to denote the flow domain in two or three dimensions and $\partial\Omega$ to denote its boundary. The domain boundary is represented as a combination of two parts:

$$\partial\Omega = \partial\Omega_d \cup \partial\Omega_o,\ \partial\Omega_d \cap \partial\Omega_o = \emptyset \tag{2.1}$$

where $\delta\Omega_d$ is used to represent the Dirichlet boundary on which we specify the velocity and $\delta\Omega_o$ is used to denote the open boundary on which both the velocity $\mathbf{u}$ and the pressure p are unknown.

The motion of the single-phase flows is described by incompressible Navier-Stokes equation in non-dimensional form on this domain(see e.g. [2, 3]):

$$\frac{\partial \mathbf{u}}{\partial t} + \mathbf{u}\cdot\nabla\mathbf{u} + \nabla p - \nu\nabla^2\mathbf{u} = \mathbf{f}(\mathbf{x},\mathbf{t}), \tag{2.2a}$$

$$\nabla\cdot\mathbf{u} = 0 \tag{2.2b}$$

In the above equations, $\mathbf{x}$ denotes the spatial co-ordinate, t denotes the time, $\mathbf{u}(\mathbf{x},\mathrm{t})$ is the normalized velocity field, $\mathbf{p}(\mathbf{x},\mathrm{t})$ is the normalized pressure, $\mathbf{f}(\mathbf{x},\mathrm{t})$ represents an external body force and the term ν is a constant which denotes the normalized viscosity, $\nu = \frac{1}{Re}$, where Re is the Reynolds number which is defined using an appropriate characteristic length scale and a characteristic velocity scale.

We impose the following condition on the Dirichlet boundary:

$$\mathbf{u} = \mathbf{w}(\mathbf{x}, t), on\ \partial\Omega_d \tag{2.3}$$

where $\mathbf{w}$ denotes the boundary velocity which is known. On the outflow boundary $\delta\Omega_o$ we will use the family of convective-like energy stable open boundary conditions in the non-dimensional form as given in [3]:

$$\begin{aligned}\nu D_o \frac{\partial \mathbf{u}}{\partial t} - p\mathbf{n} + \nu \mathbf{n} \cdot \nabla \mathbf{u} - \left[(\theta + \alpha_2)\frac{1}{2}|\mathbf{u}|^2 \mathbf{n} + (1 - \theta + \alpha_1)\frac{1}{2}(\mathbf{n} \cdot \mathbf{u})\mathbf{u} \right] \Theta_0(\mathbf{n}, \mathbf{u}) \\ = \mathbf{f}_b(\mathbf{x}, t), on\ \delta\Omega_o,\end{aligned} \tag{2.4}$$

In the above equation, D_o is a non-negative constant ($\mathrm{D}_o \geq 0$), which is normalized by $\frac{1}{U_o}$, where U_0 is the characteristic velocity scale and $\mathbf{n}$ is the unit vector normal to the outflow boundary $\partial\Omega_o$ and pointing outwards. The prescribed vector function $\mathbf{f}_b$ is used for the purpose of numerical testing only and it is set to $\mathbf{f}_b = 0$ when performing actual simulations. θ, α_1 and α_2 are chosen constants satisfying the following conditions [3]:

$$0 \leq \theta \leq 1, \quad \alpha_1 \geq 0, \quad \alpha_2 \geq 0.$$

$\Theta_0(\mathbf{n}, \mathbf{u})$ is a smoothed step function given which is given by [73]:

$$\Theta_0(\mathbf{n}, \mathbf{u}) = \frac{1}{2}(1 - tanh\frac{\mathbf{n} \cdot \mathbf{u}}{\delta U_o}) \tag{2.5}$$

In the above equation, δ is a non-dimensional positive constant ($\delta > 0$) which controls the sharpness of the smoothed step function. The smaller the δ, the sharper is the smoothed step function and the simulation results will not be affected by δ if it is sufficiently small [73]. The smoothed step function Θ_o will approach the normal step function as $\delta \to 0$ i.e :

$$\lim_{\delta \to 0} \Theta_0(\mathbf{n}, \mathbf{u}) = \Theta_{s0}(\mathbf{n}, \mathbf{u}) = \begin{cases} 1, & \mathbf{n} \cdot \mathbf{u} < 0 \\ 0, & otherwise \end{cases}. \tag{2.6}$$

This outflow boundary condition (2.4) ensures the energy stability of the system even in the presence of strong vortices at the open boundary [3].

We represent the outflow boundary condition (2.4) in a more compact form as:

$$\nu D_o \frac{\partial \mathbf{u}}{\partial t} - p\mathbf{n} + \nu \mathbf{n} \cdot \nabla \mathbf{u} - \mathbf{E}(\mathbf{n}, \mathbf{u}) = \mathbf{f}_b(\mathbf{x}, t), on\ \delta\Omega_o \tag{2.7}$$

where,

$$\mathbf{E}(\mathbf{n}, \mathbf{u}) = \left[(\theta + \alpha_2)\frac{1}{2}|\mathbf{u}|^2\mathbf{n} + (1 - \theta + \alpha_1)\frac{1}{2}(\mathbf{n} \cdot \mathbf{u})\mathbf{u} \right] \Theta_0(\mathbf{n}, \mathbf{u}) \tag{2.8}$$

The governing equations (2.2a)-(2.2b) are also supplemented by the initial condition for the velocity:

$$\mathbf{u}(\mathbf{x}, t = 0) = \mathbf{u}_{in}(\mathbf{x}) \tag{2.9}$$

where $\mathbf{u}_{in}$ is the initial velocity field.

2.2 A Modified Consistent Splitting Method

In this section we are going to present the modified consistent splitting scheme for solving the Navier-Stokes problem. The governing equations (2.2a) and (2.2b) together with the the Dirichlet boundary condition (2.3) on $\partial\Omega_d$, the open boundary condition (2.7) on $\partial\Omega_o$ and the initial condition (2.9) form the system of equations which have to be solved for the purpose of numerical simulations of single-phase flows.

Let us denote the time step index $n \geqslant 0$, and τ^n to denote the value of a generic variable τ at time step n. We define the velocity at time $t = 0$ based on (2.9) i.e., $\mathbf{u}^0 = \mathbf{u}_{in}$.

Initial Pressure Calculation Let $q \in H^1(\Omega)$ denote a test function, where $H^1(\Omega)$ denotes the set of globally continuous and square integrable functions defined on Ω. We obtain an equation in the weak form about the initial pressure P^0 by taking the L^2 inner product between (2.2a) and ∇q and using (2.2b), (2.3) and (2.7) and then enforce the condition $t = 0$ on the resulting equation:

$$\int_\Omega \nabla p^0 \cdot \nabla q + \frac{1}{\nu D_0}\int_{\partial\Omega_0} p^0 q = \int_\Omega \left[\mathbf{f}^0 - \mathbf{N}(\mathbf{u}^0)\right] \cdot \nabla q - \nu \int_{\partial\Omega_d \cup \partial\Omega_0} \mathbf{n} \times (\nabla \times \mathbf{u}^0) \cdot \nabla q - \int_{\partial\Omega_d} \mathbf{n} \cdot \frac{\partial \mathbf{w}}{\partial t}\bigg|^0 q - \frac{1}{\nu D_0}\int_{\partial\Omega_0} \left[\mathbf{f}_b^0 \cdot \mathbf{n} + \mathbf{n} \cdot \mathbf{E}(\mathbf{n}, \mathbf{u}^0) - \nu \mathbf{n} \cdot \nabla \mathbf{u}^0 \cdot \mathbf{n}\right] q,\ \forall q \in H^1_{p0}(\Omega) \tag{2.10}$$

where $\mathbf{N}(\mathbf{u}) = \mathbf{u}\cdot\nabla\mathbf{u}$ and $\frac{\partial \mathbf{w}}{\partial t}\Big|^{0}$ denotes $\frac{\partial \mathbf{w}}{\partial t}$ at time $t = 0$ which is computed using a second-order backward differential formula since we know the boundary velocity $\mathbf{w}(\mathbf{x}, t)$ on $\partial\Omega_d$. We can discretize (2.10) in space using C^0 spectral elements or finite elements. We can therefore obtain the initial pressure by solving (2.10).

Then, for a known $(\mathbf{u}^n, p^n)$, we compute $(\mathbf{u}^{n+1}, p^{n+1})$, successively in a de-coupled fashion as follows:

For $\mathbf{u}^{n+1}$ (velocity sub-step):

$$\frac{\gamma_0\mathbf{u}^{n+1} - \hat{\mathbf{u}}}{\Delta t} + \mathbf{N}(\mathbf{u}^{*,n+1}) + \nabla p^{*,n+1} - \nu_m\nabla^2\mathbf{u}^{n+1} = \mathbf{f}^{n+1} - (\nu - \nu_m)\nabla\times\nabla\times\mathbf{u}^{*,n+1}, \tag{2.11a}$$

$$\mathbf{u}^{n+1} = \mathbf{w}^{n+1} \; on \; \delta\Omega_d, \tag{2.11b}$$

$$\nu D_o\frac{\gamma_0\mathbf{u}^{n+1} - \hat{\mathbf{u}}}{\Delta t} - p^{*,n+1}\mathbf{n} + \nu\mathbf{n}\cdot\nabla\mathbf{u}^{n+1} - \mathbf{E}(\mathbf{n}, \mathbf{u}^{*,n+1}) + \nu(\nabla\cdot\mathbf{u}^{*,n+1}\mathbf{n}) = \mathbf{f}_b{}^{n+1}, \; on \; \delta\Omega_o. \tag{2.11c}$$

For p^{n+1} (pressure sub-step):

$$\frac{\gamma_0\tilde{\mathbf{u}}^{n+1} - \hat{\tilde{\mathbf{u}}}}{\Delta t} + \mathbf{N}(\mathbf{u}^{*,n+1}) + \nabla p^{n+1} = \mathbf{f}^{n+1} - \nu\nabla\times\nabla\times\mathbf{u}^{n+1}, \tag{2.12a}$$

$$\nabla\cdot\tilde{\mathbf{u}}^{n+1} = 0, \tag{2.12b}$$

$$\mathbf{n}\cdot\tilde{\mathbf{u}}^{n+1} = \mathbf{n}\cdot\mathbf{w}^{n+1} on \; \delta\Omega_d, \tag{2.12c}$$

$$\nu D_o\mathbf{n}\cdot\frac{\gamma_0\tilde{\mathbf{u}}^{n+1} - \hat{\tilde{\mathbf{u}}}}{\Delta t} - p^{n+1} + \nu\mathbf{n}\cdot\nabla\mathbf{u}^{n+1}\cdot\mathbf{n} - \mathbf{n}\cdot\mathbf{E}(\mathbf{n}, \mathbf{u}^{n+1}) = \mathbf{f}_b{}^{n+1}\cdot\mathbf{n}, on \; \delta\Omega_o. \tag{2.12d}$$

In the above equations, Δt is the time step size and $\tilde{\mathbf{u}}^{n+1}$ is an auxiliary variable approximating $\mathbf{u}^{n+1}$. $\mathbf{u}^{*,n+1}$ is a J-th order explicit approximation of $\mathbf{u}^{n+1}$ where J denotes the temporal order of accuracy of the algorithm and can either be 1 or 2. The terms $\frac{\gamma_0\mathbf{u}^{n+1} - \hat{\mathbf{u}}}{\Delta t}$ and $\frac{\gamma_0\tilde{\mathbf{u}}^{n+1} - \hat{\mathbf{u}}}{\Delta t}$ are J-th order backward difference approximations of $\frac{\partial \mathbf{u}}{\partial t}|^{n+1}$. The terms $\mathbf{u}^{*,n+1}$, $\hat{\mathbf{u}}$ and γ_0 are given by:

$$\mathbf{u}^{*,n+1} = \begin{cases} \mathbf{u}^n, & J = 1, \\ 2\mathbf{u}^n - \mathbf{u}^{n-1}, & J = 2. \end{cases} \tag{2.13}$$

$$\hat{\mathbf{u}} = \begin{cases} \mathbf{u}^n, & J = 1, \\ 2\mathbf{u}^n - \frac{1}{2}\mathbf{u}^{n-1}, & J = 2, \end{cases} \qquad \gamma_0 = \begin{cases} 1, & J = 1, \\ \frac{3}{2}, & J = 2. \end{cases} \tag{2.14}$$

One can observe that the overall structure of the algorithm presented above resembles that of a consistent-splitting type strategy [15, 17]. The important feature that allows the proposed scheme to give stable computations at high Reynolds numbers unlike a standard consistent splitting scheme, is the introduction of term $\nu_m \nabla^2 \mathbf{u}^{n+1}$ in (2.11a). The parameter ν_m is a specified constant which can be varied to increase the stability of the simulations. Note that when $\nu_m = \nu$, the algorithm presented above becomes a standard consistent splitting scheme. Also, it is important to note that the choice of ν_m only affects the stability of the simulation and not the accuracy of the results, which we will be demonstrating later with the help of simulations in Section 2.4.

As noted in [2, 3], we add an extra term $\nu(\nabla \cdot \mathbf{u})\mathbf{n}$ in Eq. (2.11c) to improve the stability of the simulations when there are no backflows. Also, the terms $\dfrac{\partial \mathbf{u}}{\partial t}$ and $\mathbf{n} \cdot \nabla \mathbf{u}$ in the discrete equation (2.11c) have been treated implicitly and approximated using $\mathbf{u}^{n+1}$ leading to a Robin-type condition for the velocity $\mathbf{u}^{n+1}$ on the outflow boundary $\delta\Omega_o$. We obtain the equation (2.12d) in the pressure sub-step by taking the inner product between the outflow boundary condition (2.7) and the directional vector $\mathbf{n}$ on the outflow boundary $\partial\Omega_0$. The $\dfrac{\partial \mathbf{u}}{\partial t}$ term in the pressure sub-step is also treated implicitly by approximating it using $\tilde{\mathbf{u}}^{n+1}$ leading to a Robin-type condition for the pressure p^{n+1} on the outflow boundary $\delta\Omega_o$ (see (2.12d)). The explicit approximation using u^{n+1} for the $\dfrac{\partial \mathbf{u}}{\partial t}$ term in (2.12d) will not be stable unless D_0 is very small [3].

2.3 Implementation with $\mathbf{C}^0$ Spectral Elements

In this section we will discuss about the implementation of the algorithm (2.11a)-(2.12d), using C^0-continuous high-order spectral elements for spatial discretizations [3, 32, 66, 71, 72]. The advantages of using C^0 spectral elements when compared to C^0 finite elements is that we attain global high-order accuracy and the spatial exponential convergence when using spectral element method. However, the subsequent

formulations discussed below are general and not limited to spectral elements (i.e., we can even use C^0 finite elements).

One of the main issues that arise when using C^0 elements to implement this algorithm is that the higher order terms such as $\nabla\times\nabla\times u$ cannot be readily computed in the discrete function space of C^0 elements [1–3, 53, 73]. To overcome this problem, we develop the weak forms of the algorithm so that the equations to be solved using C^0 elements do not contain terms with derivatives of order two or higher.

Weak form for Velocity Let us denote $\varphi(\mathbf{x}) \in H^1_{u0}(\Omega)$ as the test function, where $H^1_{u0}(\Omega) = \{v \in H^1(\Omega) \ : \ v|_{\partial\Omega_d=0}\}$.

We represent (2.11a) in a compact manner :

$$\frac{\gamma_0}{\nu_m\Delta t}\mathbf{u}^{n+1} - \nabla^2\mathbf{u}^{n+1} = \frac{1}{\nu_m}\mathbf{G}^{n+1} + (1-\frac{\nu}{\nu_m})\nabla\times\omega^{*,n+1} \tag{2.15}$$

where $\omega{=}\nabla\times\mathbf{u}$ is the vorticity,

$$\mathbf{G}^{n+1} = \mathbf{f}^{n+1} - \mathbf{N}(\mathbf{u}^{*,n+1}) + \frac{\hat{\mathbf{u}}}{\Delta t} - \nabla p^{*,n+1} \tag{2.16}$$

Then, taking L^2 inner product between the test function φ and (2.15) and then integrating by parts, we obtain:

$$\begin{aligned}\frac{\gamma_0}{\nu_m\Delta t}\int_\Omega \mathbf{u}^{n+1}\varphi + \int_\Omega \nabla\varphi\cdot\nabla\mathbf{u}^{n+1} &= \frac{1}{\nu_m}\int_\Omega \mathbf{G}^{n+1}\varphi \\ + (1-\frac{\nu}{\nu_m})\left[\int_\Omega \omega^{*,n+1}\times\nabla\varphi + \int_{\partial\Omega_o}\mathbf{n}\times\omega^{*,n+1}\varphi\right] &+ \int_{\partial\Omega_o}\mathbf{n}\cdot\nabla\mathbf{u}^{n+1}\varphi, \quad \forall\varphi\end{aligned} \tag{2.17}$$

and we have used the divergence theorem and the assumption that $\varphi{=}0$ on the Dirichlet boundary $\partial\Omega_o$. We can further express the term $\mathbf{n}\cdot\nabla\mathbf{u}^{n+1}$ in terms of $\mathbf{u}^{n+1}$ and other explicit quantities using the equation (2.11c) on the outflow boundary $\partial\Omega_o$ so that we get the final weak form for $\mathbf{u}^{n+1}$:

$$\begin{aligned}
&\frac{D_o\gamma_0}{\Delta t}\int\limits_{\partial\Omega_o}\mathbf{u}^{n+1}\varphi+\frac{\gamma_0}{\nu_m\Delta t}\int\limits_{\Omega}\mathbf{u}^{n+1}\varphi+\int\limits_{\Omega}\nabla\varphi\cdot\nabla\mathbf{u}^{n+1}\\
&\quad=\frac{1}{\nu_m}\int\limits_{\Omega}\mathbf{G}^{n+1}\varphi+(1-\frac{\nu}{\nu_m})\left[\int\limits_{\Omega}\omega^{*,n+1}\times\nabla\varphi+\int\limits_{\partial\Omega_o}\mathbf{n}\times\omega^{*,n+1}\varphi\right]\\
&+\frac{1}{\nu}\int\limits_{\partial\Omega_o}\left[\mathbf{f}_b{}^{n+1}+\frac{\nu D_o}{\Delta t}\hat{\mathbf{u}}+p^{*,n+1}\mathbf{n}+\mathbf{E}(\mathbf{n},\mathbf{u}^{*,n+1})-\nu(\nabla\cdot\mathbf{u}^{*,n+1}\mathbf{n})\right]\varphi,\ \forall\varphi
\end{aligned}\tag{2.18}$$

Weak form for Pressure Let us first take the divergence of (2.12a) so that we obtain a pressure Poisson-type equation:

$$\nabla^2 p^{n+1}=\nabla\cdot\left[\mathbf{f}^{n+1}-\mathbf{N}(\mathbf{u}^{*,n+1})\right]\tag{2.19}$$

where (2.12b) has been used. Let $q\in H^1(\Omega)$ denote a test function. Now taking the L^2 inner product between q and (2.19) and re-arranging terms we get:

$$\int\limits_{\Omega}\nabla p^{n+1}\cdot\nabla q=\int\limits_{\Omega}\left[\mathbf{f}^{n+1}-\mathbf{N}(\mathbf{u}^{*,n+1})\right]\cdot\nabla q+\int\limits_{\partial\Omega}\mathbf{n}\cdot\left[\nabla p^{n+1}q-\mathbf{f}^{n+1}+\mathbf{N}(\mathbf{u}^{*,n+1})\right]q\tag{2.20}$$

by using integration by parts and the divergence theorem. To calculate the second integral on the RHS of equation (2.20), we calculate that integral for Dirichlet boundary and the outflow boundary separately and then add them i.e., $\int\limits_{\partial\Omega}=\int\limits_{\partial\Omega_d}+\int\limits_{\partial\Omega_o}$. Taking the inner product between (2.12a) and the directional vector $\mathbf{n}$ and then taking the L^2 inner product of the resulting equation with the test function q over $\partial\Omega_d$ we obtain:

$$\int\limits_{\partial\Omega_d}\mathbf{n}\cdot\left[\nabla p^{n+1}q-\mathbf{f}^{n+1}+\mathbf{N}(\mathbf{u}^{*,n+1})\right]q=\frac{1}{\Delta t}\int\limits_{\partial\Omega_d}\mathbf{n}\cdot\hat{\mathbf{u}}q-\frac{\gamma_o}{\Delta t}\int\limits_{\partial\Omega_d}\mathbf{n}\cdot\mathbf{w}^{n+1}-\nu\int\limits_{\partial\Omega_d}\mathbf{n}\cdot\nabla\times\omega^{n+1}q\tag{2.21}$$

by using equation (2.12c). Next, we take the inner product of (2.12a) with the directional vector $\mathbf{n}$ and then the taking L^2 inner product of the resulting equation with q over $\partial\Omega_o$ we obtain :

$$\int_{\partial\Omega_o} \mathbf{n}\cdot\left[\nabla p^{n+1}q - \mathbf{f}^{n+1} + \mathbf{N}(\mathbf{u}^{*,n+1})\right] q = -\frac{1}{\nu D_o}\int_{\partial\Omega_o} p^{n+1}q - \nu\int_{\partial\Omega_o}\mathbf{n}\cdot\nabla\times\omega^{n+1}q$$

$$-\frac{1}{\nu D_o}\int_{\partial\Omega_o}\left[\mathbf{f}_b^{n+1}\cdot\mathbf{n} - \nu\mathbf{n}\cdot\nabla\mathbf{u}^{n+1}\cdot\mathbf{n} + \mathbf{n}\cdot\mathbf{E}(\mathbf{n},\mathbf{u}^{n+1})\right] q \tag{2.22}$$

and we have used the equation (2.12d). Now using (2.21) and (2.22) in (2.20), we obtain the final weak form for the pressure p^{n+1}:

$$\begin{aligned}\int_{\Omega}\nabla p^{n+1}\cdot\nabla q + \frac{1}{\nu D_o}\int_{\partial\Omega_o} p^{n+1}q = \int_{\Omega}\left[\mathbf{f}^{n+1} - \mathbf{N}(\mathbf{u}^{*,n+1})\right]\cdot\nabla q + \frac{1}{\Delta t}\int_{\partial\Omega_d}\mathbf{n}\cdot\hat{\mathbf{u}}q \\ -\frac{\gamma_o}{\Delta t}\int_{\partial\Omega_d}\mathbf{n}\cdot\mathbf{w}^{n+1} - \nu\int_{\partial\Omega}\mathbf{n}\times\omega\cdot\nabla q \\ -\frac{1}{\nu D_o}\int_{\partial\Omega_o}\left[\mathbf{f}_b^{n+1}\cdot\mathbf{n} - \nu\mathbf{n}\cdot\nabla\mathbf{u}^{n+1}\cdot\mathbf{n} + \mathbf{n}\cdot\mathbf{E}(\mathbf{n},\mathbf{u}^{n+1})\right] q\end{aligned} \tag{2.23}$$

and using the identity,

$$\int_{\partial\Omega}\mathbf{n}\cdot\nabla\times\omega^{n+1}q = \int_{\partial\Omega}\mathbf{n}\times\omega\cdot\nabla q \tag{2.24}$$

It should be noted that the final weak forms i.e., (2.18) and (2.23) do not contain any terms with second or higher order derivatives. So the equations (2.18) and (2.23), together with the Dirichlet boundary condition (2.11b) on $\partial\Omega_d$ are to be discretized using the C^0 spectral elements. Also, auxiliary velocity $\tilde{\mathbf{u}}^{n+1}$ term is eliminated in the weak formulations and it is therefore not computed explicitly by the solver.

Let us denote the flow domain Ω discretized using the spectral element mesh as Ω_h such that $\Omega_h = \cup_{e=1}^{N_{el}}\Omega_h^e$, where N_{el} denotes the total number of elements in the mesh and Ω_h^e $(1 \leq e \leqslant N_{el})$ denotes the element e. Let $\partial\Omega_h$ denote the boundary of Ω_h, such that $\partial\Omega_h = \partial\Omega_{dh}\cup\partial\Omega_{oh}$, where the terms $\partial\Omega_{dh}$ and $\partial\Omega_{oh}$ represent the

discretized $\partial\Omega_d$ and $\partial\Omega_o$ respectively. We denote the linear space of polynomials of degree K by $\prod_K(\Omega_h^e)$. The characteristic i.e the degree of the polynomials K will be referred to as the element order for the rest of this context. Let $H^1(\Omega_h)$ denote the set of globally continuous and square-integrable functions defined on Ω_h. Define function spaces:

$$\begin{cases} X_h = \left\{ \; v \in H^1(\Omega_h) \;\; : \;\; v|_{\Omega_h^e} \in \Pi_K(\Omega_h^e), \; 1 \leqslant e \leqslant N_{el} \; \right\}, \\ X_{h0} = \left\{ \; v \in X_h \;\; : \;\; v|_{\partial\Omega_h} = 0 \; \right\}. \end{cases} \tag{2.25}$$

Let $(.)_h$ denote the discretized version of the variable $(.)$. Then the fully discretized version of the equation (2.18) is: Find $\mathbf{u}_h^{n+1} \in X_h$ such that:

$$\begin{aligned} &\frac{D_o\gamma_0}{\Delta t}\int\limits_{\partial\Omega_{oh}} \mathbf{u}_h^{n+1}\varphi_h + \frac{\gamma_0}{\nu_m\Delta t}\int\limits_{\Omega_h} \mathbf{u}_h^{n+1}\varphi_h + \int\limits_{\Omega_h} \nabla\varphi_h \cdot \nabla {\mathbf{u}_h}^{n+1} \\ &\quad = \frac{1}{\nu_m}\int\limits_{\Omega_h} \mathbf{G}_h^{n+1}\varphi_h + (1-\frac{\nu}{\nu_m})\left[\int\limits_{\Omega_h} \omega_h^{*,n+1}\times\nabla\varphi_h + \int\limits_{\partial\Omega_{oh}} \mathbf{n}_h \times \omega_h^{*,n+1}\varphi\right] \\ &+ \frac{1}{\nu}\int\limits_{\partial\Omega_{oh}} \left[{\mathbf{f}_{bh}}^{n+1} + \frac{\nu D_o}{\Delta t}\hat{\mathbf{u}}_h + p_h^{*,n+1}\mathbf{n}_h + \mathbf{E}_h(\mathbf{n}_h, \mathbf{u}_h^{*,n+1}) - \nu(\nabla\cdot\mathbf{u}_h^{*,n+1}\mathbf{n}_h)\right]\varphi_h, \\ &\qquad\qquad\qquad\qquad\qquad\qquad\qquad\qquad\qquad\qquad\qquad\qquad \forall\varphi_h \in X_{h0}, \end{aligned} \tag{2.26}$$

together with discretized version of the Dirichlet boundary condition (2.11b)

$$\mathbf{u}_h^{n+1} = \mathbf{w}_h^{n+1}, \; on \; \partial\Omega_{dh}. \tag{2.27}$$

The discretized version of (2.23) is: Find $p_h^{n+1} \in X_h$ such that

$$\begin{aligned} \int\limits_{\Omega_h} \nabla p_h^{n+1}\cdot\nabla q_h + \frac{1}{\nu D_o}\int\limits_{\partial\Omega_{oh}} p_h^{n+1}q_h &= \int\limits_{\Omega_h}\left[\mathbf{f}_h^{n+1} - \mathbf{N}_h({\mathbf{u}_h}^{*,n+1})\right]\cdot\nabla q_h + \frac{1}{\Delta t}\int\limits_{\partial\Omega_{dh}} \mathbf{n}_h\cdot\hat{\mathbf{u}}_h q_h \\ &\quad - \frac{\gamma_o}{\Delta t}\int\limits_{\partial\Omega_{dh}} \mathbf{n}_h\cdot\mathbf{w}_h^{n+1} - \nu\int\limits_{\partial\Omega_h} \mathbf{n}_h\times\omega_h\cdot\nabla q_h \\ &\quad - \frac{1}{\nu D_o}\int\limits_{\partial\Omega_{oh}} \left[\mathbf{f}_{bh}^{n+1}\cdot\mathbf{n}_h - \nu\mathbf{n}_h\cdot\nabla\mathbf{u}_h^{n+1}\cdot\mathbf{n}_h + \mathbf{n}_h\cdot\mathbf{E}_h(\mathbf{n}_h, \mathbf{u}_h^{n+1})\right] q_h, \\ &\qquad\qquad\qquad\qquad\qquad\qquad\qquad\qquad\qquad\qquad \forall q_h \in X_h. \end{aligned} \tag{2.28}$$

Solution Algorithm The final solution procedure can be summarized as follows. Within a time step, with known (u_h^n, p_h^n) we compute the variables at next time step (n+1) as follows:

• Solve equation (2.26), together with the Dirichlet condition 2.27 on $\partial\Omega_{dh}$, for $\mathbf{u}_h^{n+1}$;

• Solve equation (2.28), for $\mathbf{p}_h^{n+1}$;

One can observe from (2.26) and (2.28) that the computations for the velocity and the pressure are completely decoupled. Also, different components of the velocity $\mathbf{u}_h^{n+1}$ are not coupled and therefore can be computed separately.

It has been noted in [17,74–76] and the references therein that if the approximation spaces for the discrete velocity and pressure do not satisfy an inf-sup condition for compatibility, there will be spurious pressure modes. However, it has been discussed that one of the exceptions to this condition is the case where we use equal-order approximations for the velocity and pressure [1–3, 12, 15, 66, 74]. Therefore, in the current spectral-element implementation, to approximate the pressure and the velocity, we use equal orders of expansion polynomials so as to avoid the spurious pressure modes.

2.4 Numerical Tests for Single-Phase Flows

In this section we consider two two-dimensional test problems with open boundaries to demonstrate the performance of the numerical method proposed in Section 2.2. We will also discuss the spatial and temporal convergence rates of the proposed algorithm. We consider single-phase incompressible flows for all the subsequent tests in this section.

2.4.1 Convergence Rates

In this subsection we illustrate the spatial and temporal convergence rates of the numerical scheme proposed in Section 2.2 by using an unsteady analytic flow problem.

We consider a two-dimensional flow domain $\Omega = [(x, y) : 0 \leqslant x \leqslant 1; -1 \leqslant y \leqslant 1]$ as shown in Fig. 2.2(a). We also use the following analytic expressions for the flow variables:

$$\begin{cases} u = Acos(\pi y)sin(ax)sin(bt) \\ v = -\dfrac{Aa}{\pi}sin(\pi y)cos(ax)sin(bt) \\ p = A\sin(\pi y)sin(ax)cos(bt) \end{cases} \tag{2.29}$$

where u, v denote the components of the velocity in the x and y direction respectively and A, a and b are user-defined constants. The body force term $\mathbf{f(x,t)}$ in 2.2a is chosen in such a manner that the analytic expressions in (2.29) satisfy the equation (2.2a). The expressions for the velocity inherently satisfy the continuity equation (2.2b). The analytic expressions in (2.29) have been used for the convergence tests in [2, 3].

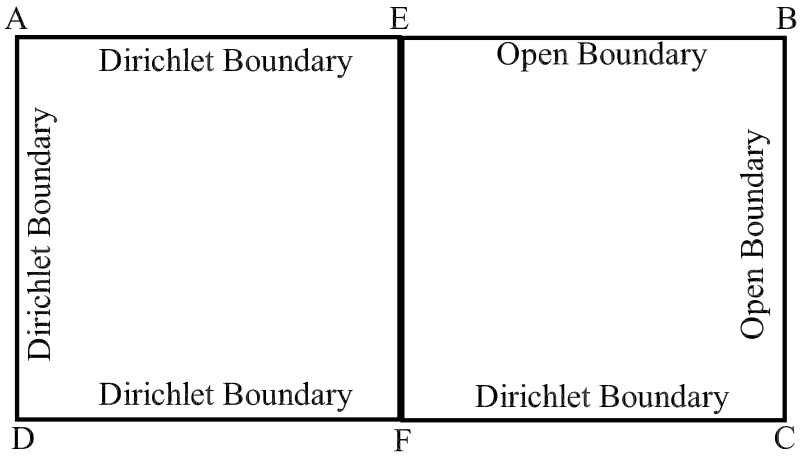

Figure 2.1.: Flow Domain and boundary conditions.

We discretize the domain $\overline{ABCD}$ into two quadrilateral spectral elements of equal size($\overline{ADFE}$ and $\overline{EFCB}$) along the x direction. We impose the Dirichlet condition for the velocity (2.3) on the boundaries $\overline{AE}$, $\overline{AD}$ and $\overline{CD}$ and set the boundary velocity $\mathbf{w}$(x,t) to the analytical expressions given in (2.29). The boundaries $\overline{EB}$ and $\overline{BC}$ are assumed to be open and we impose the outflow boundary condition at

these boundaries. We set $D_0 = 1$ and $\delta = \frac{1}{20}$ in (2.7) and choose the function $\mathbf{f}_b$ such that analytic expressions in (2.29) satisfy the open boundary condition (2.7) at the boundaries $\overline{EB}$ and $\overline{BC}$. We set the non-dimensional viscosity to $\nu = 0.01$ and the ratio $\frac{\nu_m}{\nu} = 2$ for performing simulations. The temporal order is set to $J = 2$. Also the parameters α_1,α_2 and θ in the outflow boundary condition (2.7) are set to 1, 0 and 1 respectively.

We use the scheme presented in Section 2.2 and run the simulations from time $t = 0$ to a specified time $t = t_f$. Then we compute the numerical errors by comparing the simulation results with the analytical solution in (2.29) at time $t = t_f$.

Spatial convergence test To determine the spatial convergence rate of the numerical scheme we use a fixed time step size Δt=0.001 and set the total simulation time to t_f=0.1 and then perform simulations by increasing the element order from 2 to 20 in intervals of 2. Fig 2.2(a) shows the L^∞ and L^2 errors of the flow variables obtained from the numerical simulation as a function of the element order. We observe from the Figure 2.2(a) that the numerical errors for all the flow variables keep decreasing exponentially as the element order increases (while below 12). Beyond element order 14, we observe that the error levels do not change. This is because when the element order becomes large, the temporal truncation error becomes dominant and thus saturating the total error.

Temporal convergence test For the temporal convergence test, we fix the element order to 16 and set the total simulation time to t_f=0.5, and then perform simulations by decreasing the time step size systematically from Δt=0.1 to Δt=0.000390625 (by a factor of 0.5). Figure 2.2(b) shows the L^∞ and L^2 errors of the flow variables as a function of the time step size Δt in logarithmic scales. We observe that the method has a second-order convergence rate in time for all the flow variables when Δt is below 0.025.

The above results indicate that the method proposed in section 2.2 has a spatial exponential convergence rate and a temporal second-order convergence rate.

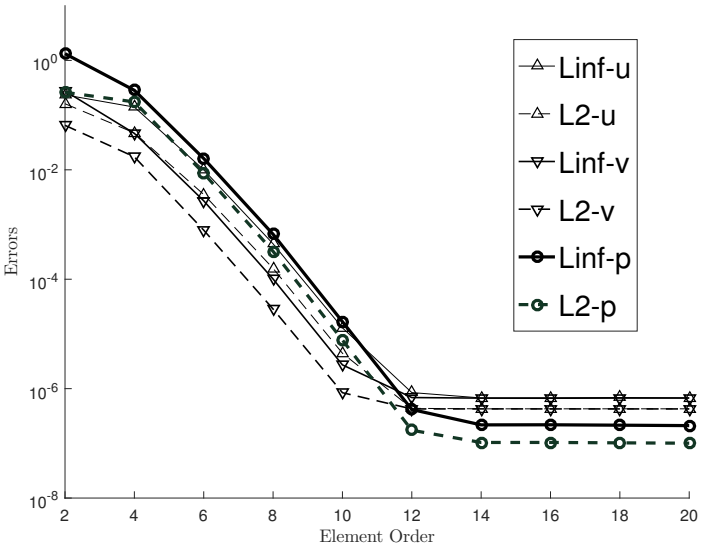

(a)

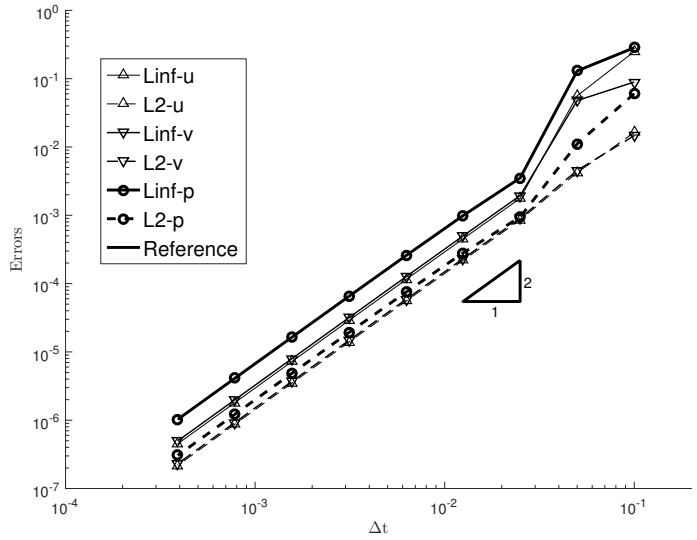

(b)

Figure 2.2.: Spatial and Temporal convergence rates: (a) L^∞ and L^2 errors as a function of element order with fixed Δt=0.001. (b) L^∞ and L^2 errors as a function of Δt with a fixed element order 16.

2.4.2 Flow Past a Circular Cylinder

In this subsection, we are going to use the method developed in section 2.2 to analyze a canonical flow past a two-dimensional circular cylinder. The goal of this subsection is to demonstrate the capability of the method in dealing with strong vortices at the outflow boundary. We performed the simulations for a wide range of Reynolds numbers up to $Re = 5000$. We also demonstrate the accuracy of the method by comparing the results obtained by simulating the test case for a wide range of Reynolds numbers with the experimental data from the literature. This flow problem has also been used in other works related to the current research topic [2,3].

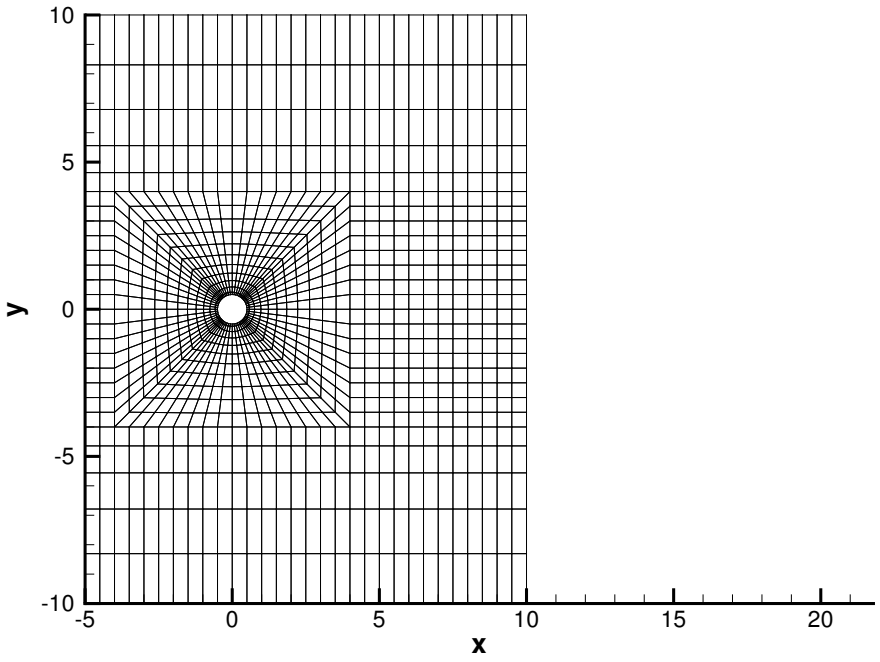

Figure 2.3.: Flow past a circular cylinder: Flow domain showing the spectral-element mesh with 1228 elements

The problem setup is as follows: We consider a circular cylinder with a diameter d, and a rectangular flow domain Ω containing the cylinder defined by $\Omega =$

$\{(x, y) : -5d \leqslant x \leqslant L, -10d \leqslant y \leqslant 10d\}$ (where L is the length of the wake region, as specified below) as shown in in Figure 2.3. The origin of the coordinate system is at the center of the cylinder. A total of five flow domains with different wake-region sizes, specifically $\frac{L}{d} = 3, 5, 10, 15, 20$ have been considered for numerical testing. Fig 2.3 shows the flow domain with $\frac{L}{d} = 10$ and it is assumed that we have used this flow domain for our simulations unless stated explicitly otherwise.

We assume that the flow is periodic on the top side ($\frac{y}{d} = +10$) and the bottom side ($\frac{y}{d} = -10$) of the domain boundary . A uniform inflow enters the domain from the left boundary ($\frac{x}{d} = -5$) with a velocity $\mathbf{u} = (u, v) = (U_0, 0)$, where U_0=1 is the characteristic velocity scale. The flow leaves the domain from the right boundary ($x = L$), which is assumed to be open and we impose the outflow boundary condition (2.7) at this boundary with $\mathbf{f}_b = 0$ and $\delta = 0.01$. We also impose a velocity no-slip condition on the the surface of the cylinder i.e., we use the Dirichlet condition (2.3) and set the boundary velocity $\mathbf{w}$=0. Also note that the diameter of the cylinder is chosen as $d = 1$ for all the simulations.

We use a mesh of quadrilateral spectral elements to discretize the domain. In Figure 2.3 there are 1228 quadrilateral elements. Similarly, as the domain size changes the number of elements vary. The number of quadrilateral elements for the other domain sizes $\dfrac{L}{d} = 3, 5, 15, 20$ are 724, 968, 1488 and 1748 respectively (see Figure 2.4). Also note that the parameters α_1,α_2 and θ in the outflow boundary condition (2.7) are fixed to 1, 0 and 1 respectively for subsequent discussions unless explicitly stated otherwise.

We solve the incompressible Navier-Stokes equations to advance in time as mentioned in section 2.3. Also, the velocity is normalized by the characteristic velocity scale U_0, the length variables are normalized by the diameter of the cylinder d and the time t is normalized by $\frac{d}{U_o}$. We therefore define the Reynolds number Re for this problem as follows:

$$Re = \frac{1}{\nu} = \frac{U_0 d}{\nu_f} \tag{2.30}$$

where ν_f is the kinematic viscosity of the fluid and ν is the non-dimensional viscosity.

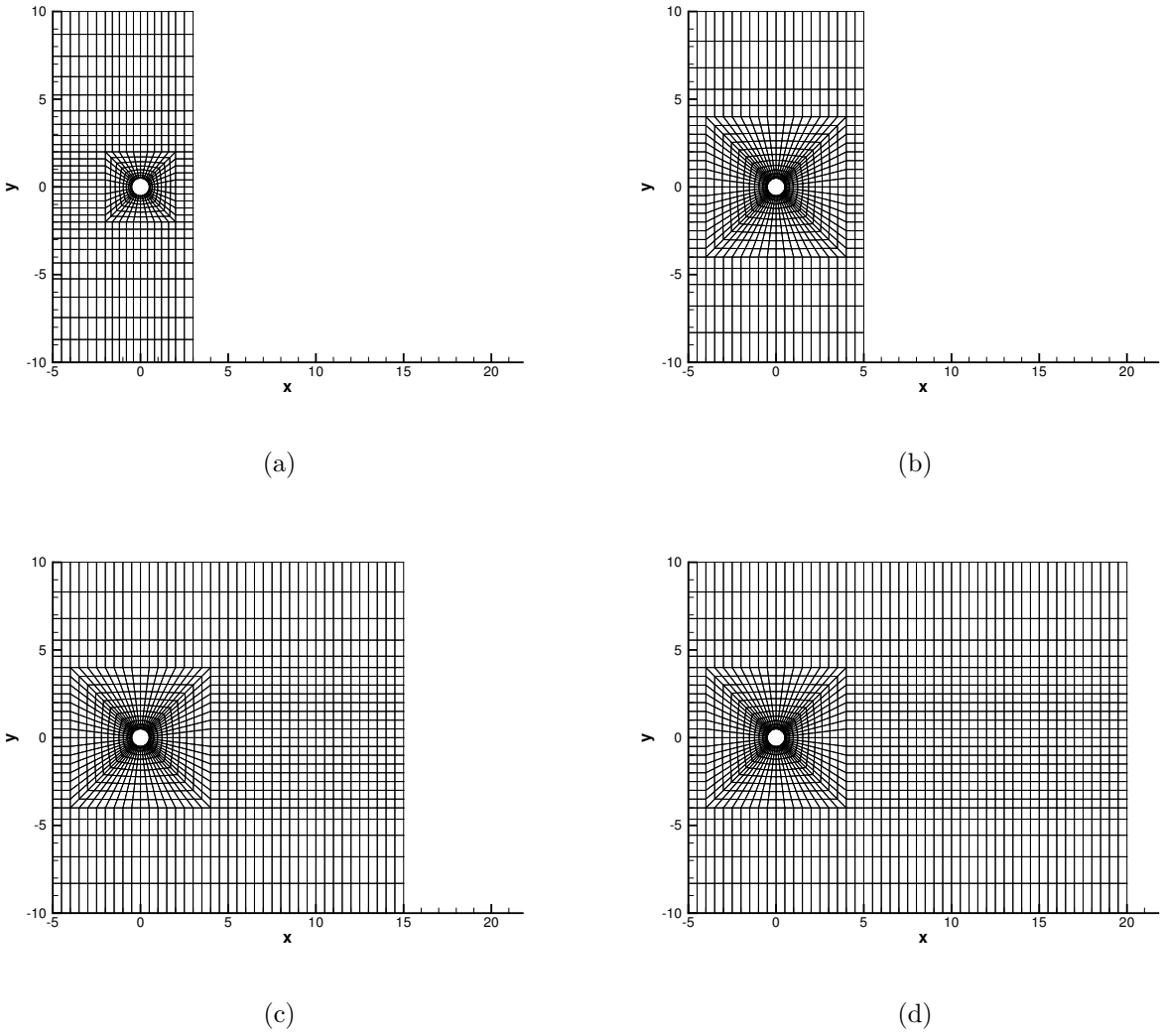

(a) (b)

(c) (d)

Figure 2.4.: Flow past a circular cylinder: (a) Flow domain with $\frac{L}{d} = 3$ and 724 spectral elements. (b) Flow domain with $\frac{L}{d} = 5$ and 968 spectral elements. (c) Flow domain with $\frac{L}{d} = 15$ and 1488 spectral elements. (d)Flow domain with $\frac{L}{d} = 3$ and 1748 spectral elements.

Domain Size Test To study the effect of the size of the wake region on the global flow parameters we have performed simulations for two Reynolds numbers $Re = 30$ and $Re = 100$ on different flow domains. The global flow parameters i.e the mean drag

coefficient (C_d), root-mean-square drag coefficient (C_d) and the root-mean-square lift coefficient (C_L) can be computed as follows:

$$C_d = \frac{\bar{F}_x}{\frac{1}{2}\rho U_0^2}, \quad C_d^{'} = \frac{F_x^{'}}{\frac{1}{2}\rho U_0^2}, \quad C_L = \frac{F_y^{'}}{\frac{1}{2}\rho U_0^2}$$

where $\bar{F}_x$ is the mean drag (x-component of the force on the cylinder) averaged through time, $F_x^{'}$ is the root-mean square of drag, $F_y^{'}$ is the root-mean-square of the lift(y-component of the force on the cylinder) and $\rho = 1$ is the fluid density.

For this test we have used the time step sizes $\Delta t = 2.5 \times 10^{-4}$ and $\Delta t = 5 \times 10^{-4}$ for simulating the flows at $Re = 30$ and $Re = 100$ respectively. We set the element order to 10 and $\frac{\nu_m}{\nu} = 10$ when performing the simulations for both cases of Reynolds number. Table 2.1 lists the global flow parameters obtained from this test. One can observe from this data that the global flow parameters computed from the simulations are influenced as the size of the wake region increases for up to a certain value (around $\frac{L}{d} = 10$). As we increase the size of the wake region beyond this value the global flow parameters do not change, that is, the domain size no longer has a significant effect on the simulation results. Based on this observation, we use the flow domain with $\frac{L}{d} = 10$ for all the subsequent discussions.

Force Test We perform simulations for various Reynolds numbers between $Re = 5$ and $Re = 200$ for this test. The goal of this test is to demonstrate the accuracy of the method by comparing the global force parameters obtained from the simulations with that of the experimental data and other numerical simulations from the literature. Different flow regimes of the circular cylinder wake have been discussed in [77] and it has been mentioned that for Reynolds numbers up to around $Re = 190$ the flow around the cylinder is two-dimensional and beyond this Reynolds number the flow transitions to a three-dimensional regime. Since the simulations performed in the current test problem are for two-dimensional cylindrical flow, we compare the simulation results of the global flow parameters with that of the experiments for Reynolds numbers up to $Re = 200$.

Table 2.1.: Flow past a circular cylinder: Effect of domain size on the global flow parameters for $Re = 30$ and $Re = 100$; C_d: time-averaged mean drag coefficient; $C_d^{'}$: rms drag coefficient; C_L: rms lift coefficient.

Reynolds number	Domain Length	C_d	$C_d^{'}$	C_L
30	3	1.785	0	0
	5	1.913	0	0
	10	1.933	0	0
	15	1.935	0	0
	20	1.935	0	0
100	3	1.096	0	0
	5	1.441	8.486E-3	0.262
	10	1.459	7.638E-3	0.254
	15	1.462	7.692E-3	0.253
	20	1.462	7.698E-3	0.253

We have used the following parameters for performing this test:

$$\Delta t = 5 \times 10^{-4},\ \frac{\nu_m}{\nu} = 10,\ element\ order = 8$$

Table 2.2 lists the global flow parameters obtained from simulations for the range of Reynolds numbers mentioned above. Figure 2.5 compares the mean drag coefficient C_d as a function of the Reynolds number Re between the current numerical simulations and the experimental data obtained from the literature [78–82]. We can see that the current results agree well with that of the experimental data in the two-dimensional flow regime. Therefore, the numerical algorithm proposed in Section 2.2 is capable of simulating single-phase flows with unbounded domain accurately by truncating the domain size to a finite value.

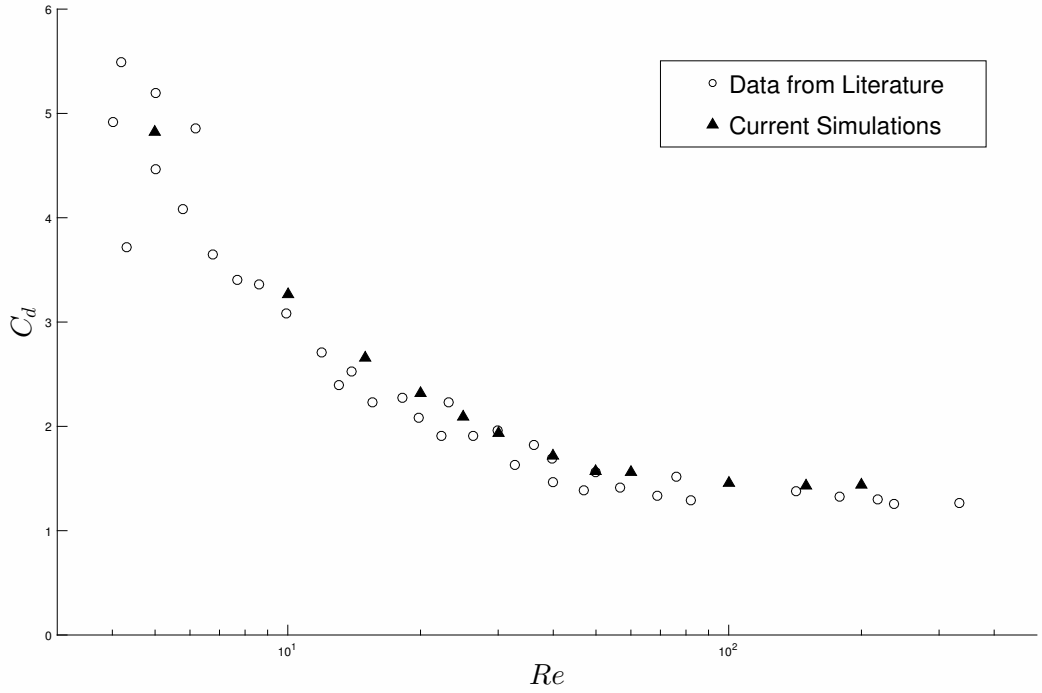

Figure 2.5.: Flow past a circular cylinder: Comparison of the mean drag coefficient as a function of Reynolds number between the current simulations and experimental data from the literature.

Effect of Temporal resolution To study the effect of the non-dimensional time step size Δt, we performed the simulations for different time step sizes, for a fixed Reynolds number ($Re = 30$) till we obtain the steady state. For this test, we set the element order to 8 and $\frac{\nu_m}{\nu} = 10$. Table 2.3 shows the mean drag coefficient at the steady state for different time step sizes. We can observe that decreasing the time step size Δt beyond 5×10^{-3} does not have any significant effect on the mean drag coefficient at steady state.

Table 2.2.: Flow past a circular cylinder: Effect of Reynolds number on the global flow parameters.

Reynolds number	C_d	$C_d^{'}$	C_L
5	4.818	0	0
10	3.262	0	0
15	2.654	0	0
20	2.316	0	0
25	2.094	0	0
30	1.934	0	0
40	1.717	0	0
50	1.572	0	0
60	1.558	1.199E-03	0.113
100	1.459	7.630E-03	0.254
150	1.430	2.140E-02	0.401
200	1.437	3.584E-02	0.526

Table 2.3.: Flow past a circular cylinder: Effect of Δt on mean drag coefficient C_d for Reynolds Number=30.

Δt	C_d
5×10^{-3}	1.935
2×10^{-3}	1.935
1×10^{-3}	1.935
5×10^{-4}	1.934
2.5×10^{-4}	1.933

Effect of Spatial resolution To study the effect of element order i.e the spatial resolution we performed simulations by varying the element order from 4 to 10 in steps of 2, for two Reynolds numbers $Re = 30$ and $Re = 100$. When performing these simulations we set $\frac{\nu_m}{\nu} = 10$ for all the cases and used a time step size $\Delta t = 2.5 \times 10^{-4}$ for $Re = 30$ and $\Delta t = 5 \times 10^{-4}$ for $Re = 100$. The results are tabulated in Table 3.2. From this data, one can observe that as the element order increases beyond 6, there is no significant effect of the element order on the global flow parameters for these Reynolds numbers.

Table 2.4.: Flow past a circular cylinder: Effect of element order on the global flow parameters for $Re = 30$ and $Re = 100$; C_d: time-averaged mean drag coefficient; C_d': rms drag coefficient; C_L: rms lift coefficient.

Reynolds number	Element Order	C_d	C_d'	C_L
30	10	1.933	0	0
	8	1.933	0	0
	6	1.933	0	0
	4	1.930	0	0
100	10	1.459	7.638E-03	0.254
	8	1.459	7.630E-03	0.254
	6	1.458	7.600E-03	0.254
	4	1.463	7.700E-03	0.0.256

Effect of $\frac{\nu_m}{\nu}$ To study the effect of $\frac{\nu_m}{\nu}$ on the global flow parameters, we performed simulations for different ratio of $\frac{\nu_m}{\nu}$ for three cases of Reynolds numbers $Re = 20$, 30 and 100 till we obtain a steady state. The results are tabulated in Table 2.5. From this data one can observe that the effect of $\frac{\nu_m}{\nu}$ on the steady state values is insignificant for $\frac{\nu_m}{\nu} \geqslant 5$, although it should be noted that this ratio is important for

the stability of the simulation especially at high Reynolds numbers. When performing these simulations, the time step size is fixed to $\Delta t = 5 \times 10^{-4}$ for all the cases.

Table 2.5.: Flow past a circular cylinder: Effect of $\frac{\nu_m}{\nu}$ on the global flow parameters for $Re = 20$, $Re = 30$ and $Re = 100$.

Reynolds number	Element Order	$\frac{\nu_m}{\nu}$	C_d	$C_d^{'}$	C_L
20	10	1	2.314	0	0
		5	2.316	0	0
		10	2.316	0	0
		15	2.316	0	0
		20	2.316	0	0
		25	2.316	0	0
30	10	1	1.932	0	0
		5	1.934	0	0
		10	1.934	0	0
		15	1.934	0	0
		20	1.934	0	0
		25	1.934	0	0
100	8	1	1.459	7.623E-03	0.254
		5	1.459	7.626E-03	0.254
		10	1.459	7.630E-03	0.254
		15	1.459	7.630E-03	0.254
		20	1.459	7.630E-03	0.254
		25	1.459	7.630E-03	0.254

The parameters α_1, α_2 and θ in the outflow boundary condition (2.7) were fixed to 1, 0 and 1 respectively in all the previous simulations. To study the effect of change in their values, we performed simulations for different combinations of α_1, α_2 and θ. Table 2.6 shows the effect of different combinations of α_1,α_2, Θ on mean drag coefficient for $Re = 30$. Here the element order used is 8, $\frac{\nu_m}{\nu}$ =10, $\Delta t = 2.5 \times 10^{-4}$. We can see that there is insignificant effect on the steady state results by changing the values of α_1,α_2 and θ.

Table 2.6.: Flow past a circular cylinder: Effect of α_1, α_2, Θ on mean drag coefficient C_d for $Re = 30$.

Θ	α_1	α_2	C_d
1	1	0	1.933
0	0	0	1.933
0	1	0	1.933
1	0	0	1.933
1	0	1	1.933
0.5	0	0	1.933

To demonstrate the capability of the current method in dealing with backflow instabilities and strong vortices, we have performed long time simulations at high Reynolds numbers, specifically for $Re = 2000$, 4000 and 5000. Table 2.7 shows the parameters used for performing these simulations.

Figures 2.6, 2.7 and 2.8 show the time histories of the force components (f_x=drag and f_y=lift) for the Reynolds numbers 2000, 4000 and 5000 respectively. Based on these figures we can observe that the lift and drag forces oscillate with time but remain bounded. We can also see that the force components are uniform for $Re = 2000$, whereas, for $Re = 4000$ and $Re = 5000$ the oscillations are random and much more chaotic due to the presence of strong vortices. From Table 2.7 it should be noted

that, we had to increase the spatial and temporal resolution and also the ratio of $\frac{\nu_m}{\nu}$ to obtain a stable simulations for the higher Reynolds numbers ($Re = 4000$ and $Re = 5000$) when compared to the Reynolds number $Re = 2000$. We can see from these results that using the proposed method is capable of providing stable simulation results at high Reynolds numbers by increasing the value of $\frac{\nu_m}{\nu}$. In contrast, we observe that the standard consistent splitting ($\nu_m = \nu$) method fails to provide stable computations at these Reynolds numbers.

Table 2.7.: Flow past a circular cylinder: Parameters used in the simulations for $Re = 2000$, $Re = 4000$ and $Re = 5000$.

Reynolds number	Δt	Element Order	$\frac{\nu_m}{\nu}$
2000	2.5E-4	10	10
4000	1.0E-4	12	20
5000	1.0E-4	12	20

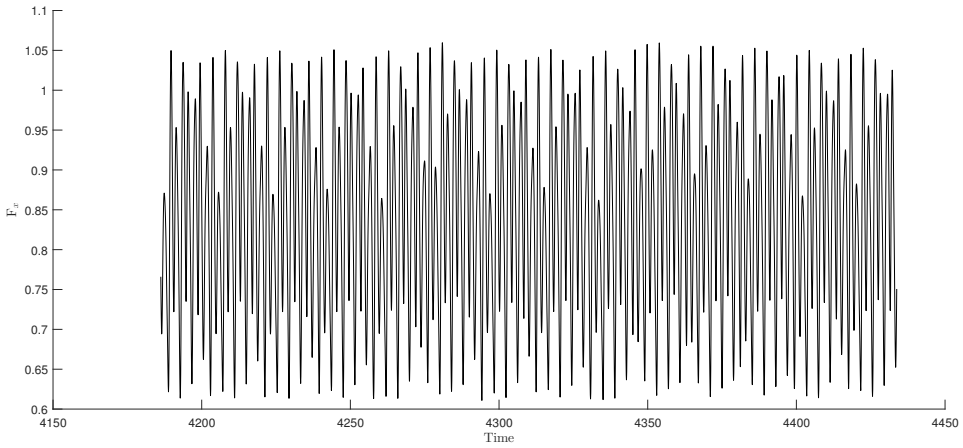

(a) fx

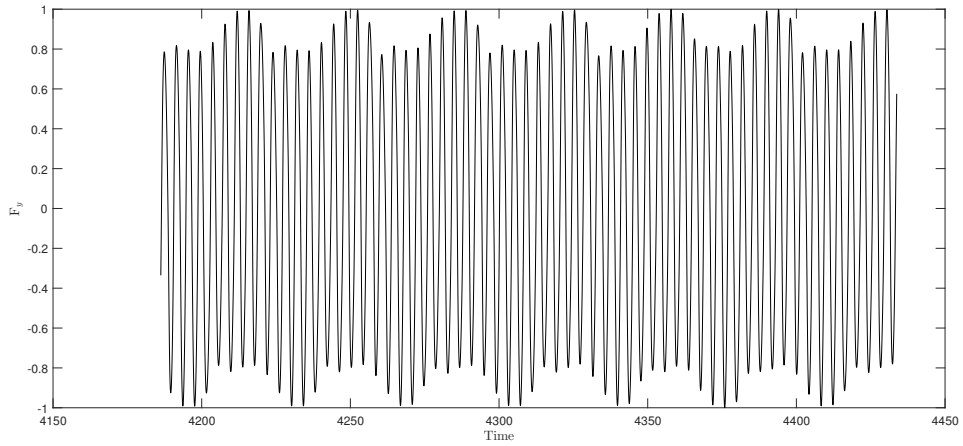

(b) fy

Figure 2.6.: Flow past a circular cylinder: Time histories of (a) drag force and (b) lift force for $Re = 2000$.

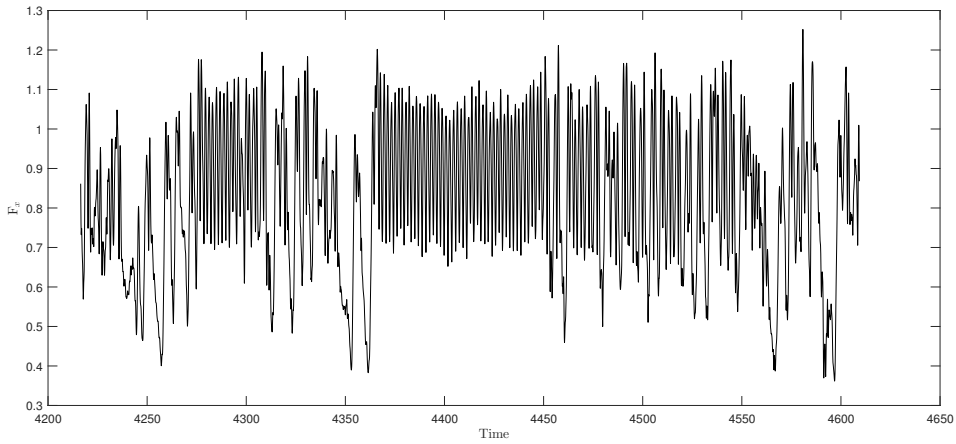

(a) fx

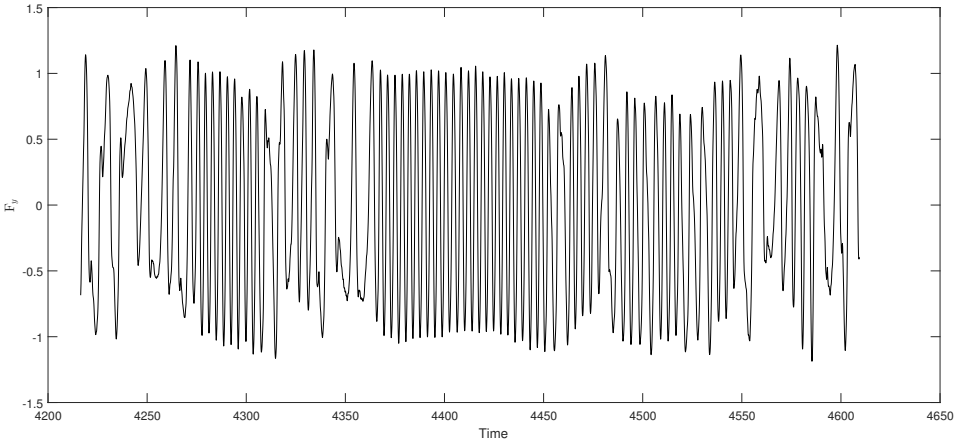

(b) fy

Figure 2.7.: Flow past a circular cylinder: Time histories of (a) drag force and (b) lift force for $Re = 4000$.

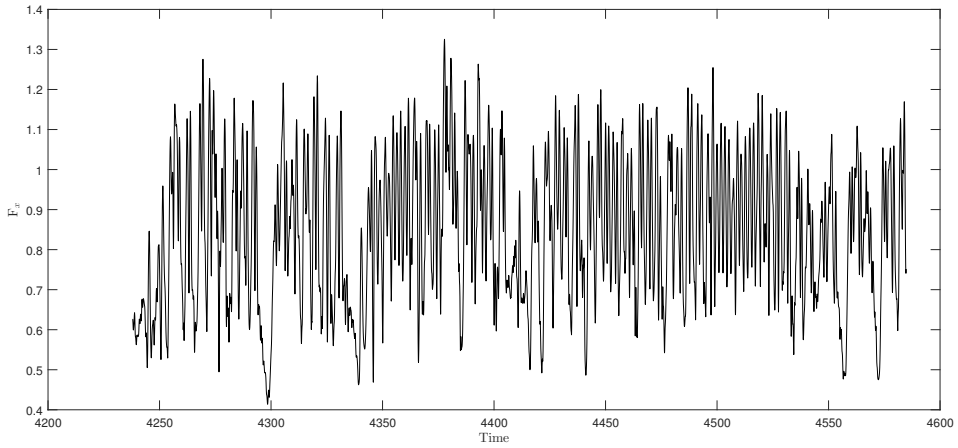

(a) fx

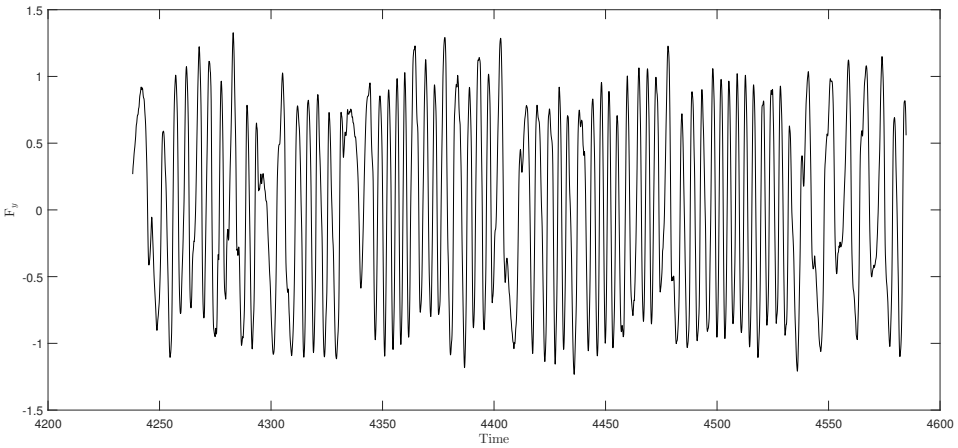

(b) fy

Figure 2.8.: Flow past a circular cylinder: Time histories of (a) drag force and (b) lift force for $Re = 5000$.

Figures 2.9(a)-(c) show the instantaneous velocity distributions obtained from the simulations near the centerline of the domain for Reynolds numbers $Re = 2000$, 4000 and 5000 respectively. From these snapshots, we can observe that, as the Reynolds number increases from $Re = 2000$ to $Re = 5000$ we can see increasingly complex vortex structures behind the cylinder. We can also observe slight deformations of the vortex when the vortex core passes through the open boundary (see Figures 2.9(a) and 2.9(c)). Note that the triangular structure observed in these figures are due to the choice of the non-uniform mesh near the cylinder as shown in Figure 2.3.

Figures 2.10 and 2.11 show the temporal sequence of the snapshots of the velocity distribution for the flows with Reynolds number $Re = 4000$ and $Re = 5000$ respectively. These snapshots illustrate the overall process of the discharge of a pair of vortices (Figures 2.10(a) and 2.11(a)) through the open boundary. As the vortices pass through through the open boundary (Figures 2.10(b) and 2.11(b)), we can observe a small region of backflows (Figures 2.10(b)-(d) and 2.11(b)-(c)). After the vortex core passes through the open boundary, we observe vortex distortions (Figures 2.10(d)-(f) and 2.11(d)-(f)). However, the simulations are still stable due to the choice of the outflow boundary condition. The overall process of the discharge of vortices through the domain appears to occur in a fairly natural way (Figures 2.10(b)-(f) and 2.11(b)-(f)).

From these simulations, we can be sure that when we use the method proposed in Section 2.2 we can obtain long-time stable simulations for flows with high Reynolds numbers even in the presence of backflows and strong vortices.

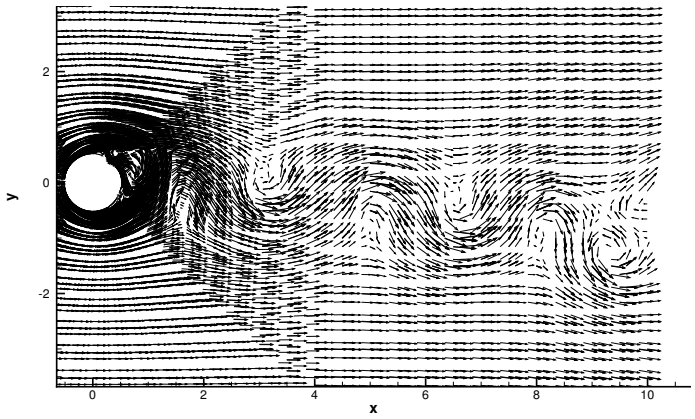

(a)

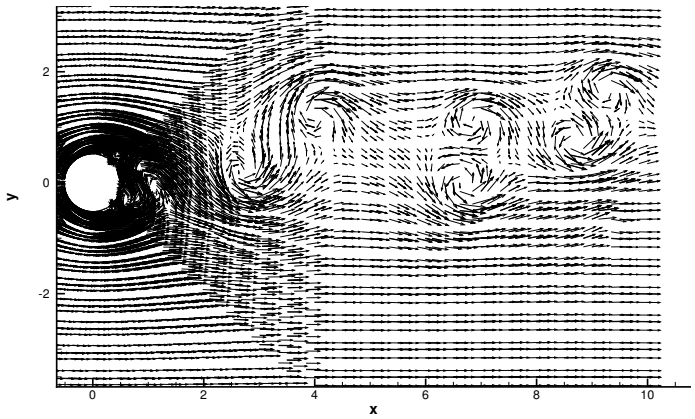

(b)

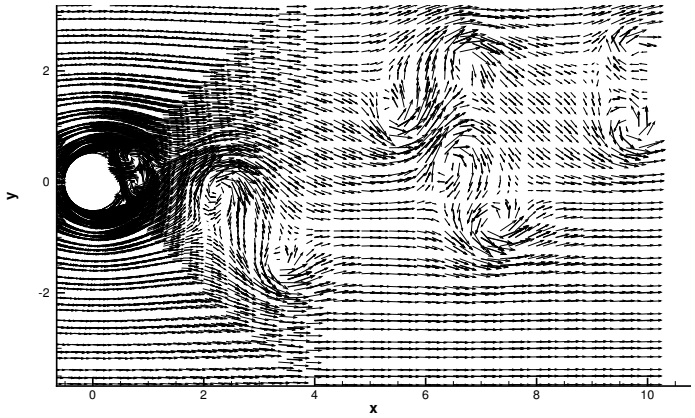

(c)

Figure 2.9.: Flow past a circular cylinder: Instantaneous velocity distribution at (a) $Re = 2000$, (b) $Re = 4000$, and (c) $Re = 5000$.

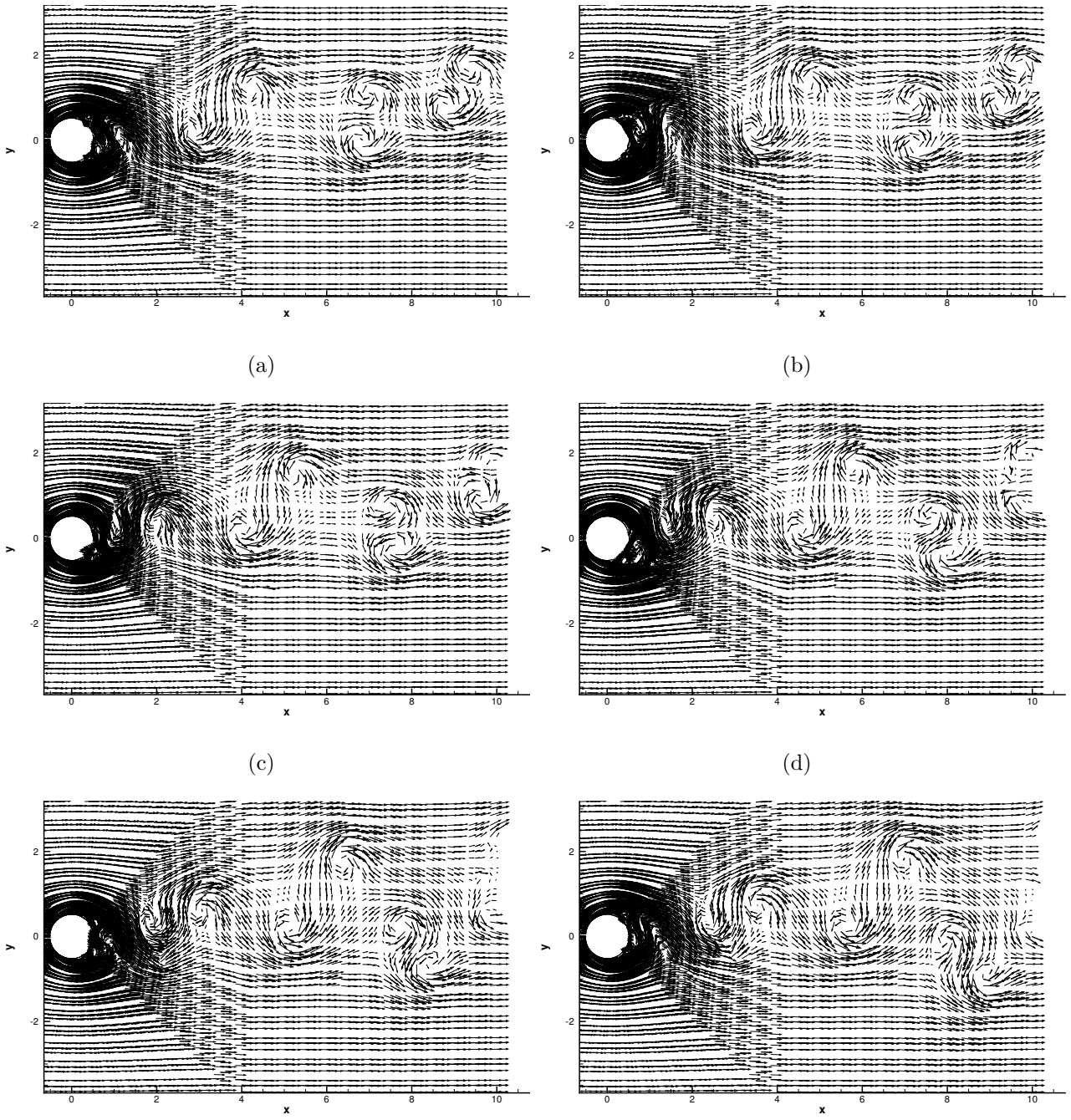

Figure 2.10.: Discharge of vortices at the open boundary(Re = 4000): temporal sequence of snapshots of the velocity fields at (a) t=4529.97, (b) t=4531.47, (c) t=4532.97, (d) t=4534.47, (e) t=4536.97, (f) t=4537.47. Velocity vectors are plotted on every fifth quadrature points in each direction within an element.

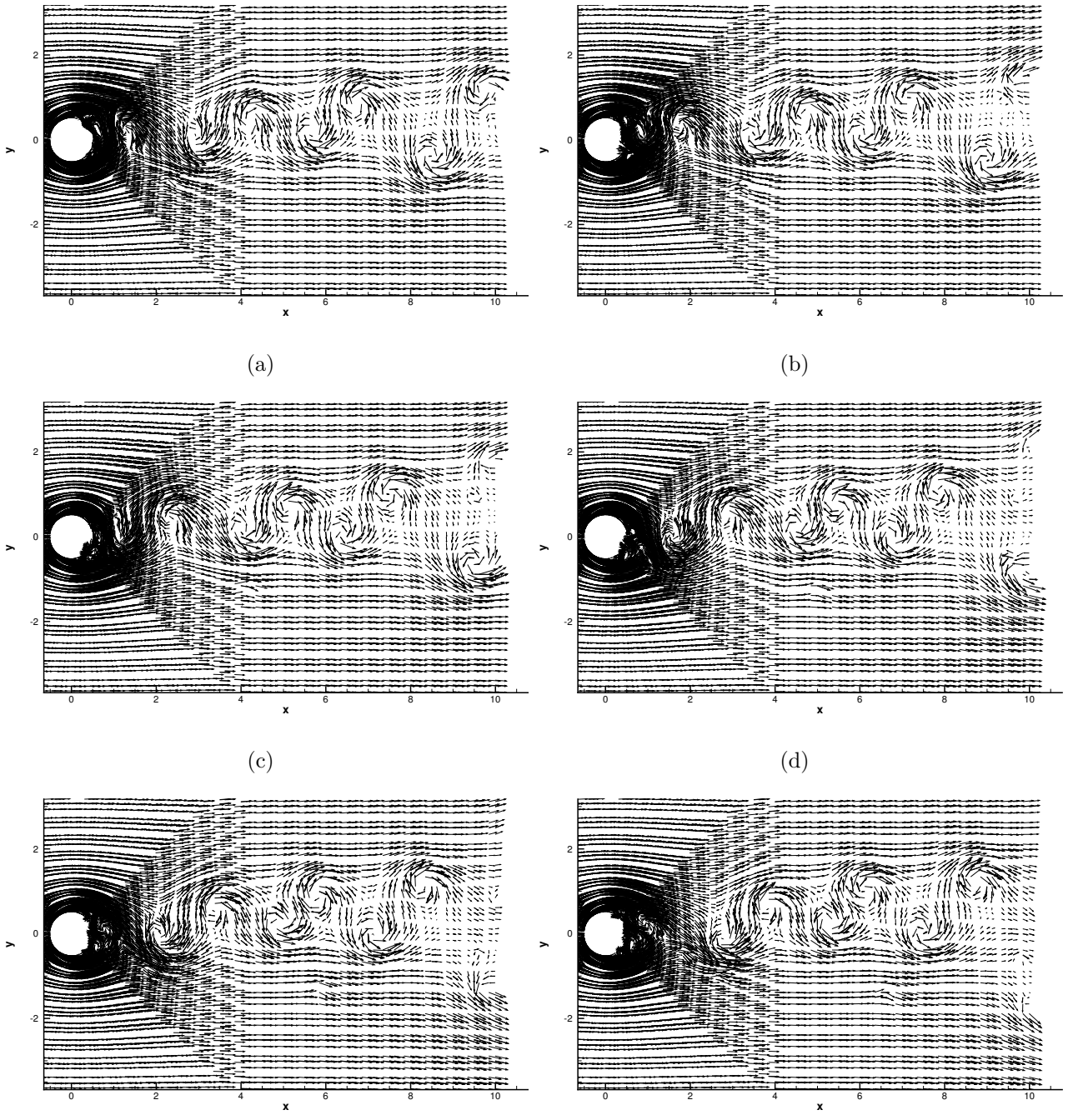

Figure 2.11.: Discharge of vortices at the open boundary(Re = 5000): temporal sequence of snapshots of the velocity fields at (a) t=4530.85, (b) t=4531.63, (c) t=4532.41, (d) t=4533.19, (e) t=4533.97, (f) t=4534.75. Velocity vectors are plotted on every fifth quadrature points in each direction within an element.

2.4.3 Double Shear Flow

In this subsection, we analyze a double shear flow using the method developed in section 2.2. This flow problem is slightly more challenging than the flow past a cylinder because of the physical instability of the shear layers at moderate Reynolds numbers combined with the open boundary. The goal of this section is to demonstrate the capability of the proposed numerical scheme in simulating complex flow phenomena at high Reynolds numbers. Note that this is again a two-dimensional simulation.

We consider a rectangular flow domain $\Omega = \left\{(x, y) : -\frac{5}{2} \leqslant x \leqslant \frac{5}{2}, 0 \leqslant y \leqslant \frac{15}{2}\right\}$ as shown in Figure 2.12 . We have two flows entering the flow domain: a higher velocity flow with an inlet diameter $D = \frac{3}{2}$ and velocity $V_2 = 1.1$ is entering the domain from the bottom covering, $-\frac{3}{4} \leqslant x \leqslant \frac{3}{4}$, where as a lower velocity flow $V_1 = 0.1$, enters the domain through the bottom from either side of the higher velocity fluid, covering the regions $-\frac{5}{2}D \leqslant x \leqslant -\frac{3}{4}$ and $\frac{3}{4} \leqslant x \leqslant \frac{5}{2}$. There are periodic boundary conditions applied on the left ($x = -\frac{5}{2}$) and right($x = \frac{5}{2}$) domain boundary and the flow can leave or enter through the top surface where the open boundary condition (2.7) is used with $D_0 = \frac{5}{3}$, $\mathbf{f}_b = 0$ and $\delta = 0.01$. We use the following velocity profile at the inlet(y=0):

$$\begin{cases} u = 0 \\ v = \frac{1}{2}\left[(V_2 + V_1) + (V_2 - V_1)(1 - H(x, 0))tanh(\frac{(\frac{x}{R0} + 1)}{(\sqrt{2}\epsilon)}) + (V_2 - V_1)tanh(\frac{(1 - \frac{x}{R0})}{(\sqrt{2}\epsilon)})\right] \end{cases} \tag{2.31}$$

where $\epsilon = \frac{D}{60}$ controls the thickness of the shear layer, $R_0 = \frac{D}{2}$, and $H(x, x_0)$ is the Heaviside step function which takes the value of 1 if $x \geq x_0$ and 0 otherwise.

For this problem, we choose the characteristic length scale $L = 1\,m$ and the characteristic velocity scale $U_0 = 1\,m/s$. Then, we normalize all the velocity variables by U_0, all the length variables by D and the time by $\frac{D}{U_0}$. The Reynolds number is calculated according to the equation (2.30), where $d = L$ for this problem. We

discretize the domain into 600 quadrilateral spectral elements of equal size with 30 elements along the y-direction and 20 elements along the x-direction.

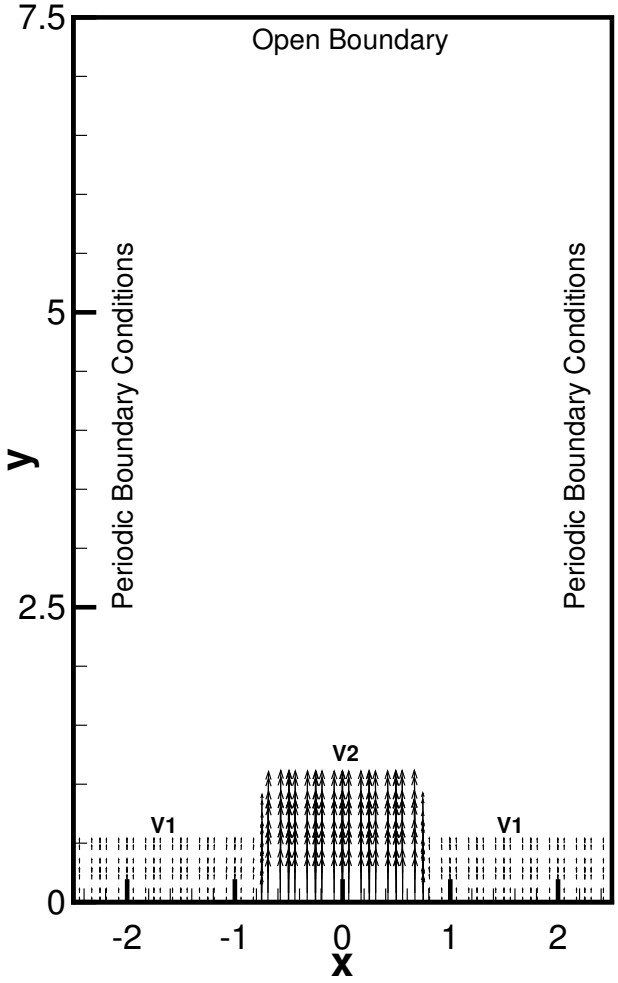

Figure 2.12.: Double Shear flow: Flow configuration and boundary conditions; Inflow velocities V_1 =0.1 and V_2=1.1.

To demonstrate the stability of the method and its capability to overcome the backflow instabilities at high Reynolds numbers, we performed long time simulations at Reynolds numbers 3000, 4000, 5000 and 7500. We have used the following parameters for performing these simulations:

$$\Delta t = 1 \times 10^{-4},\ \frac{\nu_m}{\nu} = 4000,\ \textit{element order} = 10$$

Note that for these simulations a high value of $\frac{\nu_m}{\nu}$ (around 4000) is required when compared to the flow past a circular cylinder flow (around 20) because of the complexity involved in the flow.

Figures 2.13(a)-(d) shows the snapshots of the instantaneous velocity distributions at these at $Re = 3000, 4000, 5000$ and 7500 respectively. In Figure 2.13(a), for $Re = 3000$, we can only observe a pair of vortices which are just about to leave the open boundary at the top domain and there are no vortex formations closer to the inflow boundary ($y = 0$). However, as we increase the Reynolds number the vortex formations start to occur early in the domain and closer to the inflow boundary as illustrated in 2.13(b)-(d). We can also see the formation of strong vortices near the open boundary as we increase the Reynolds number.

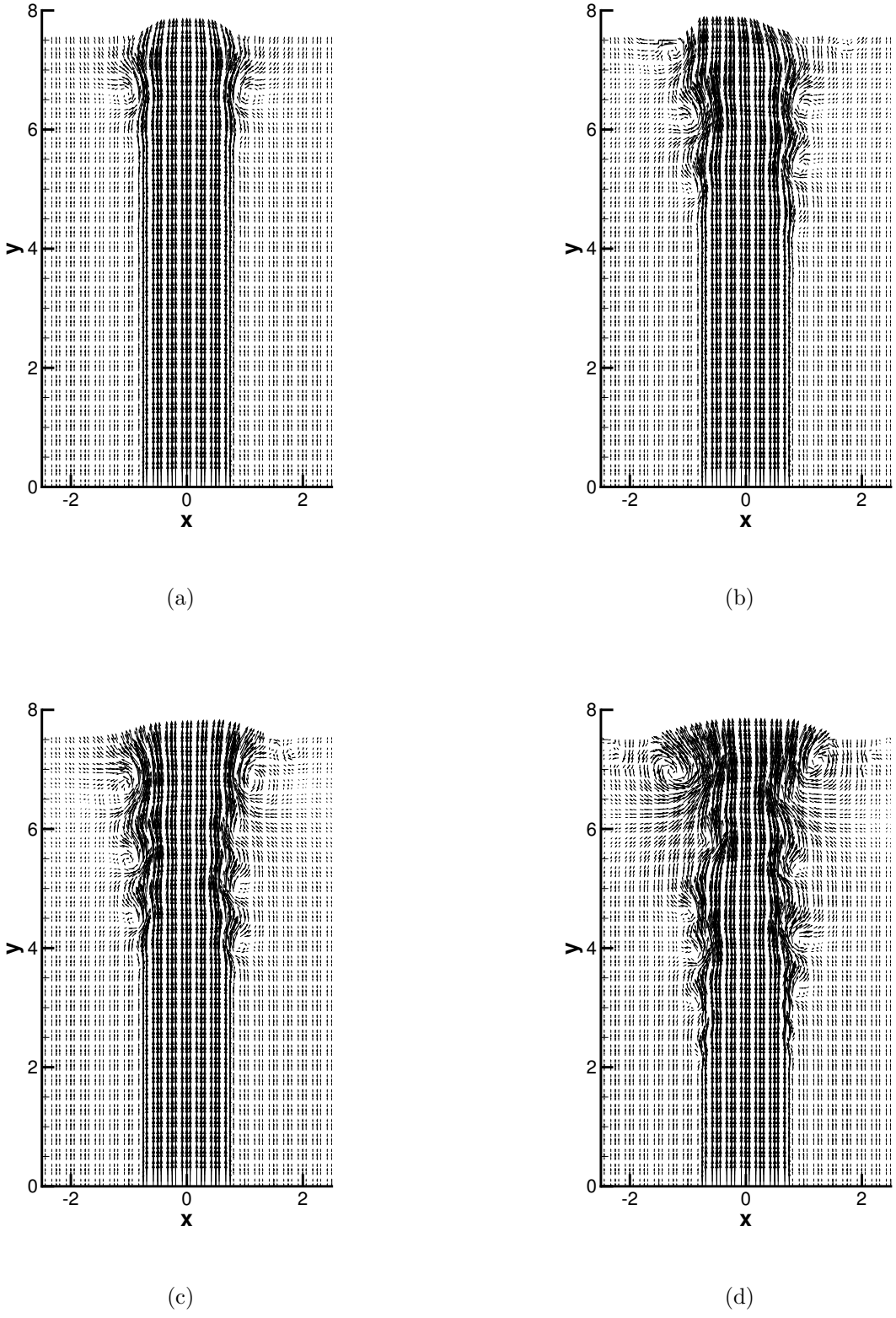

(a)

(b)

(c)

(d)

Figure 2.13.: Double Shear flow: Instantaneous velocity distribution at (a) $Re = 3000$, (b) $Re = 4000$, (c) $Re = 5000$, and (d) $Re = 7500$.

Figure 2.14 illustrates the time histories of the maximum absolute velocities $|u|_{max}$, $|v|_{max}$ (in the entire domain) and the root-mean-square(rms) velocities u_{rms}, v_{rms} (averaged over space) for Reynolds numbers 3000, 4000, 5000 and 7500. For the flow at $Re = 3000$, we observe that the values of $|u|_{max}$ and $|v|_{max}$ vary periodically (Figure 2.14(a)) over a long period of time. However, as the Reynolds number increases we observe that these values change rapidly (Figures 2.14(b)-(d)). A similar behavior can be observed even in the case of rms velocities u_{rms}, v_{rms}. The reason for this can be attributed to the presence of stronger vortices at the open boundary. Overall, we can observe that the maximum absolute velocities and the rms velocities in both the horizontal and vertical directions do not grow exponentially and always stay within a bounded region over a long period of time. This demonstrates that the computations are long-time stable at these Reynolds numbers.

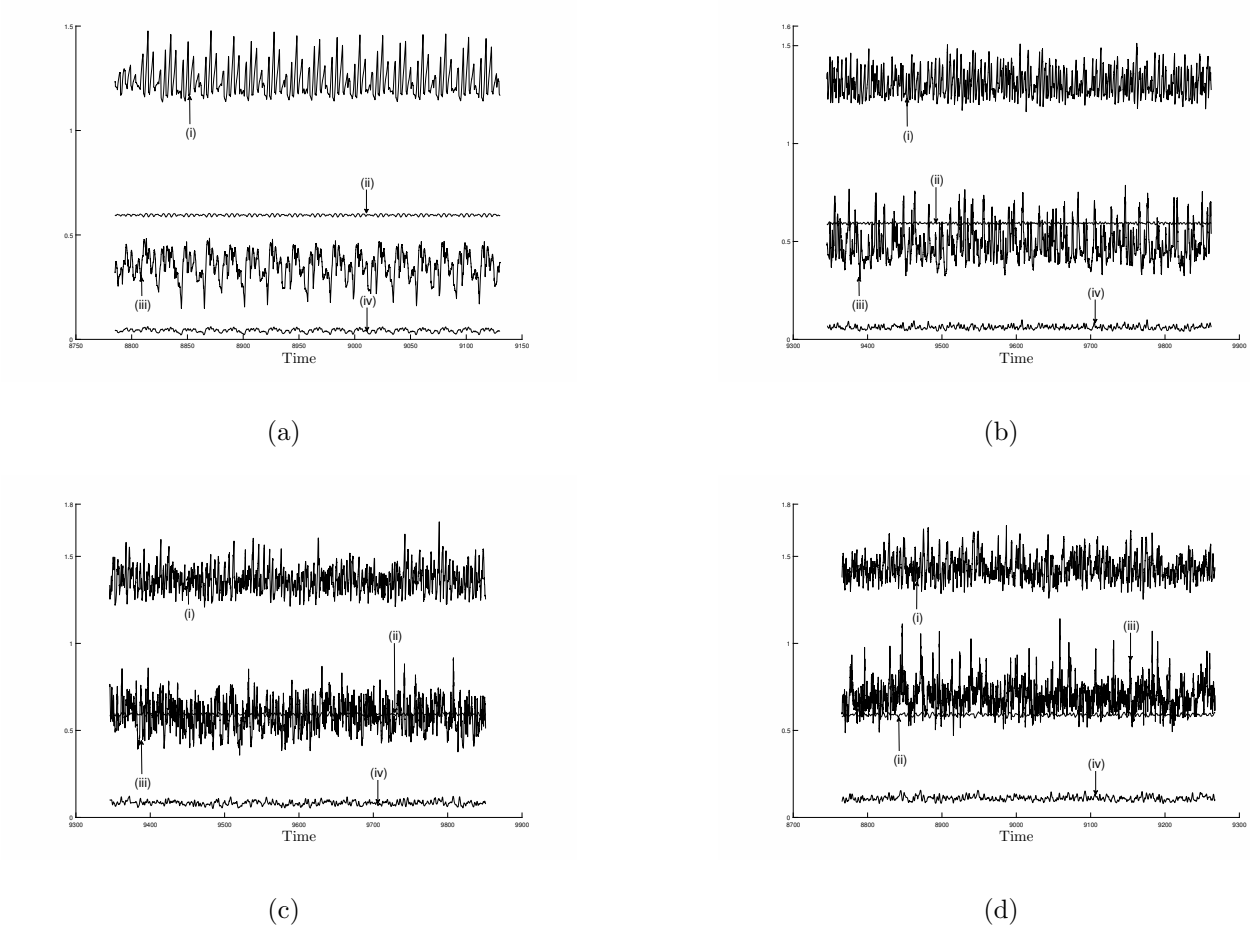

Figure 2.14.: Double Shear flow: (i) $|v|_{max}$, (ii) v_{rms}, (iii) $|u|_{max}$, (iv) u_{rms} for (a) $Re = 3000$, (b) $Re = 4000$, (c) $Re = 5000$, (d) $Re = 7500$

Figure 2.15 illustrates the temporal sequence of the snapshots of instantaneous velocity distribution for the double shear flow at $Re = 7500$. These snapshots illustrate the complex flow characteristics which occur in the double shear flows at high Reynolds numbers. We observe that as the vortex which is near the outflow boundary (Figure 2.15(a)) leaves the domain (Figure 2.15(b)-(c)), a small region of backflow occurs. Distortion to the vortex also occurs as the vortex core passes through the open boundary (Figure 2.15(c)-(f)). We can also observe that the smaller vortices which are present near the center of the domain combine with each other to form a single large vortex before leaving the domain (Figure 2.15(a)-(f)). The overall discharge of the vortices from the domain can be observed to occur almost naturally.

To summarize, in this section, we used the scheme proposed in Section 2.2 to simulate a double shear flow at high Reynolds numbers. Based on the results of the simulations presented in this section we can be sure that the proposed scheme provides long-time stable computations at high Reynolds numbers and also capture certain complex phenomena such as the merging of smaller vortices into a single large vortex.

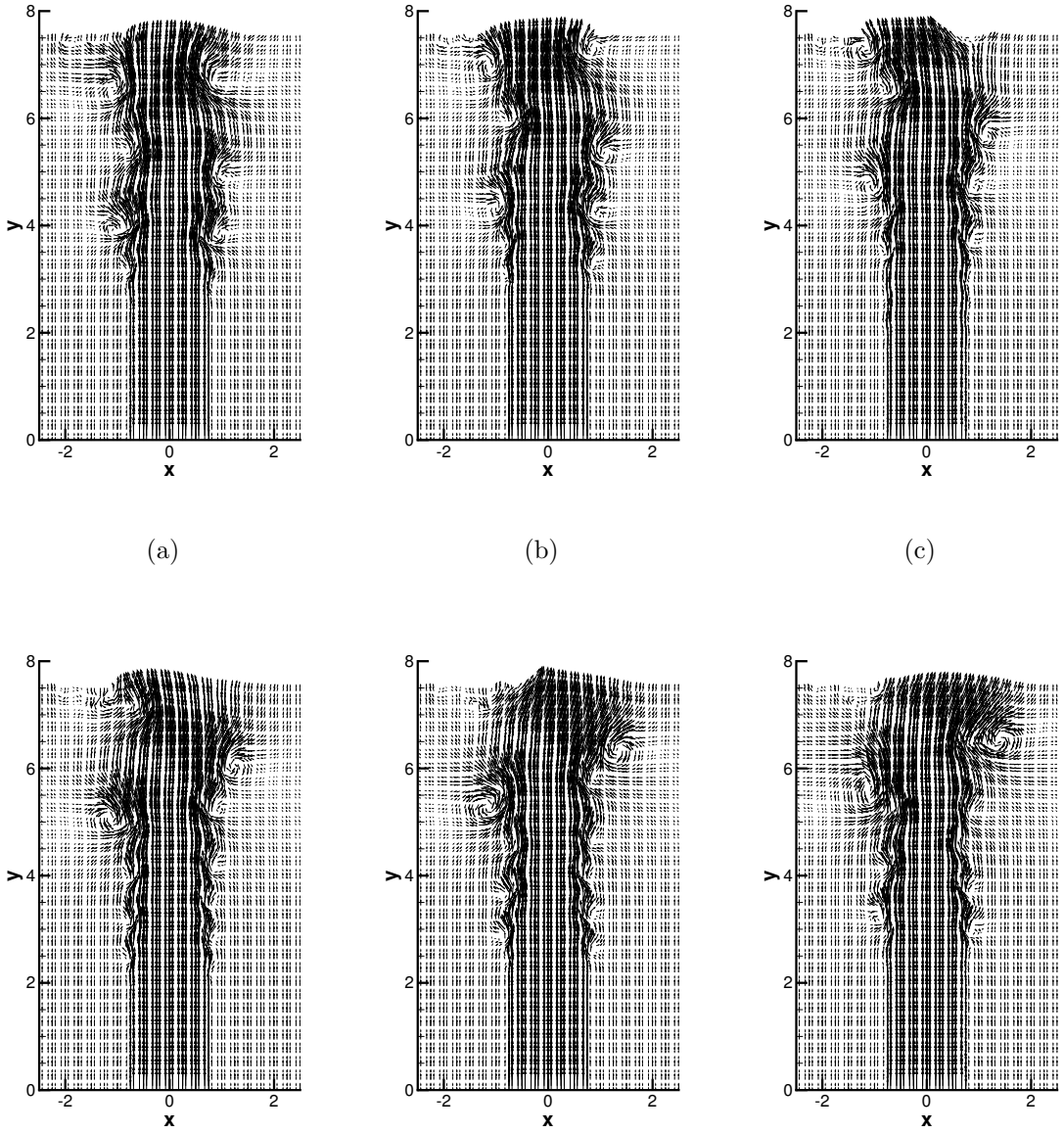

(a) (b) (c)

(d) (e) (f)

Figure 2.15.: Double Shear flow: Discharge of vortices at the open boundary(Re = 7500): temporal sequence of snapshots of the velocity fields at (a) t=9101.3, (b) t=9102.1, (c) t=9102.9, (d) t=9103.7, (e) t=9104.5, (f) t=9105.3. Velocity vectors are plotted on every fifth quadrature points in each direction within an element.

3. THREE-DIMENSIONAL HYBRID SPECTRAL ELEMENT-FOURIER SPECTRAL METHOD FOR WALL-BOUNDED TWO-PHASE FLOWS

3.1 Governing Equations and Boundary Conditions

In this section, we briefly discuss the governing equations for the two-phase flows using the phase-field approach.

For the context of this chapter, we represent the three dimensional (3D) flow domain as Ω, and its boundary is denoted by $\partial\Omega$. The flow domain is assumed to be homogeneous in at least one direction (we choose it as the z direction) and has no constraints on the complexity in the other two directions (i.e., the x and y directions). We consider a mixture of two incompressible and immiscible fluids in Ω. Let ρ_1, ρ_2 denote the density of the first and second fluid respectively, and let μ_1, μ_2 be their dynamic viscosities. In the homogeneous direction, we consider the length of the domain to be L_z such that we have the flow domain is represented as $0 \leq z \leq L_z$ in the z direction. We then assume that at $z = 0$ and $z = L_z$ the field variables and domain are periodic. If we denote the projection of the 3D domain onto the $x - y$ plane as Ω_{2D} and denote $\delta\Omega_{2D}$ as its boundary, then Ω and $\delta\Omega$ can be represented as:

$$\Omega = \Omega_{2D} \otimes [0, L_z], \quad \partial\Omega = \partial\Omega_{2D} \otimes [0, L_z]. \tag{3.1}$$

Let us denote the unit vector normal to the domain boundary $\delta\Omega$ and pointing outwards as $\mathbf{n}$ and the unit vector normal to $\delta\Omega_{2D}$ in the $x - y$ plane and pointing outwards as $\mathbf{n}_{2D}$. Note that $\mathbf{n}$ does not have any components in the homogeneous direction i.e $\mathbf{n} = (\mathbf{n}_{2D}, 0)$

Using the phase-field approach, we can describe the two phase system [47,53,60,83] by the following system of equations,

$$\rho(\frac{\partial \mathbf{u}}{\partial t} + \mathbf{u} \cdot \nabla \mathbf{u}) = -\nabla p + \nabla \cdot [\mu \mathbf{D}(\mathbf{u})] - \lambda \nabla \cdot (\nabla \phi \otimes \nabla \phi) + \mathbf{f}, \tag{3.2a}$$

$$\nabla \cdot \mathbf{u} = 0 \tag{3.2b}$$

$$\frac{\partial \phi}{\partial t} + \mathbf{u} \cdot \nabla \phi = -\lambda \gamma_1 \nabla^2 [\nabla^2 \phi - h(\phi)] + g(\mathbf{x},t). \tag{3.2c}$$

In the above equations, $\mathbf{x}$, t are the spatial coordinate and time respectively. $\mathbf{u}(\mathbf{x},t)$ is the velocity and $p(\mathbf{x},t)$ is the pressure. $\mathbf{D}(\mathbf{u}) = \nabla \mathbf{u} + \nabla \mathbf{u}^T$ (where $(.)^T$ denotes the transpose of $(.)$), $\mathbf{f}(\mathbf{x},t)$ is an external body force. $\phi(\mathbf{x},t)$ is the phase field function, $-1 \leq \phi \leq 1$. The flow regions containing the first and second fluids are denoted by $\phi = 1$ and $\phi = -1$ respectively, and the iso-surface $\phi(\mathbf{x},t) = 0$ denotes the fluid interface at any time t. The function $h(\phi)$ in (3.2c) is given by, $h(\phi) = \frac{1}{\eta^2}\phi(\phi^2 - 1)$, where η is the characteristic length scale of the interface thickness. λ is the mixing energy density, and is given by $\lambda = \frac{3}{2\sqrt{2}}\sigma\eta$ [60], where σ is the surface tension and assumed to be constant. γ_1 denotes the mobility of the interface, and it is also assumed to be constant in the current context. Also, in (3.2a) the symbol $\otimes$ represents the tensor product. The mixture density (ρ) and the dynamic viscosity (μ) are a function of the the phase field function and given by,

$$\rho(\phi) = \frac{\rho_1 + \rho_2}{2} + \frac{\rho_1 - \rho_2}{2}\phi, \mu(\phi) = \frac{\mu_1 + \mu_2}{2} + \frac{\mu_1 - \mu_2}{2}\phi. \tag{3.3}$$

Since ϕ is time dependent, both $\rho(\phi)$ and $\mu(\phi)$ also change with time. The function g($\mathbf{x}$,t) in (3.2c) is a prescribed source term which is given as an input for the purpose of numerical testing only, and is set to 0 in practical simulations.

The flow domain is assumed to be bounded by solid walls(in x and y directions) and we will use the following set of boundary conditions:

$$\mathbf{u} = \mathbf{w}(\mathbf{x},t), \ on \ \partial\Omega \tag{3.4a}$$

$$\mathbf{n} \cdot \nabla[\nabla^2\phi - h(\phi)] = \mathbf{g}_c(\mathbf{x},t),\ on\ \partial\Omega \tag{3.4b}$$

$$\mathbf{n} \cdot \nabla\phi + \frac{1}{\lambda}\mathbf{f}'_w(\phi) + \mathbf{g}_b(\mathbf{x},t) = 0,\ on\ \partial\Omega \tag{3.4c}$$

where $\mathbf{w}$ is the boundary velocity, and $\mathbf{g}_b(\mathbf{x},t)$ and $\mathbf{g}_c(\mathbf{x},t)$ are prescribed source terms for the purpose of numerical testing only and will be set to $g_b = 0$ and $g_c = 0$ when performing the actual simulations. The function $\mathbf{f}'_w(\phi)$ is given as:

$$\mathbf{f}'_w(\phi) = -\frac{3}{4}\sigma\cos(\theta_s)(1-\phi^2). \tag{3.5}$$

where θ_s is the contact angle between the solid wall and the fluid-fluid interface, measured from the side of the first fluid. Note that the boundary condition (3.5) only considers the effect of static contact angles. We refer the reader to [54] where the effects of dynamic contact angle boundary conditions are discussed in detail.

Finally, the governing equations are supplemented by the following set of initial conditions for the velocity and the phase field function:

$$\mathbf{u}(\mathbf{x},0) = \mathbf{u}_{in}(\mathbf{x}), \tag{3.6}$$

$$\phi(\mathbf{x},0) = \phi_{in}(\mathbf{x}). \tag{3.7}$$

3.2 General Algorithm Formulation

The governing equations (3.2a)-(3.2c), the boundary conditions (3.4a)-(3.4c) are the overall system of equations that need to be solved numerically. When numerically solving the governing equations using Fourier spectral expansions we face a difficulty due to the presence of the time-dependent mixture density $\rho(\phi)$ and viscosity $\mu(\phi)$ terms. Without a proper strategy, these terms would result in discrete equations about the Fourier modes involving variable coefficients. These variable coefficient form convolutions with the Fourier modes of the flow variables when we perform fast Fourier Transforms, thus coupling together all the Fourier modes of the unknown variables and nullifying the advantage of using Fourier expansions. To circumvent

this difficulty, we employ a technique developed by [53], to reformulate the pressure and the viscous terms and introduce appropriate constant-coefficient terms in the discrete equations, thus enabling the efficient use of Fourier transforms.

The numerical scheme using the strategy developed in [53] is briefly summarized below.

Equation (3.2a) is first transformed into:

$$\frac{\partial \mathbf{u}}{\partial t} + \mathbf{u}\cdot\nabla\mathbf{u} = -\frac{1}{\rho}\nabla P + \frac{\mu}{\rho}\nabla^2\mathbf{u} + \frac{1}{\rho}\nabla\mu\cdot\mathbf{D}(\mathbf{u}) - \frac{\lambda}{\rho}\left(\nabla^2\phi\right)\nabla\phi + \frac{1}{\rho}\mathbf{f}. \tag{3.8}$$

where $P = p + \frac{\lambda}{2}\nabla\phi\cdot\nabla\phi$ is an auxiliary pressure, which will be called pressure hereafter.

Let $n \geqslant 0$, denote the time step P^n, and $(.)^n$ represent the field variable at the time step n. Then, given $(\phi^n, P^n, \mathbf{u}^n)$, we obtain $(\phi^{n+1}, P^{n+1}, \mathbf{u}^{n+1})$ as follows:

For ϕ^{n+1}:

$$\frac{\gamma_0\phi^{n+1} - \hat{\phi}}{\Delta t} + \mathbf{u}^{*,n+1}\cdot\nabla\phi^{*,n+1} = -\lambda\gamma_1\nabla^2\left[\nabla^2\phi^{n+1} - \frac{S}{\eta^2}\left(\phi^{n+1} - \phi^{*,n+1}\right) - h(\phi^{*,n+1})\right] + g^{n+1}, \tag{3.9a}$$

$$\mathbf{n}\cdot\nabla[\nabla^2\phi^{n+1} - \frac{S}{\eta^2}(\phi^{n+1} - \phi^{*,n+1}) - h(\phi^{*,n+1})] = g_c^{n+1}, \quad on \quad \partial\Omega, \tag{3.9b}$$

$$\mathbf{n}\cdot\nabla\phi^{n+1} = -\frac{1}{\lambda}f_w'(\phi^{*,n+1}) - g_b^{n+1}. \tag{3.9c}$$

For pressure P^{n+1}:

$$\begin{aligned}\frac{\gamma_0\tilde{\mathbf{u}}^{n+1} - \hat{\mathbf{u}}}{\Delta t} + \frac{1}{\rho_0}\nabla P^{n+1} = &-\mathbf{u}^{*,n+1}\cdot\nabla\mathbf{u}^{*,n+1} + (\frac{1}{\rho_0} - \frac{1}{\rho^{n+1}})\nabla P^{*,n+1} - \frac{\mu^{n+1}}{\rho^{n+1}}\nabla\times\nabla\times\mathbf{u}^{*,n+1} \\ &+ \frac{1}{\rho^{n+1}}\nabla\mu^{n+1}\cdot\mathbf{D}(\mathbf{u}^{*,n+1}) - \frac{\lambda}{\rho^{n+1}}\nabla^2\phi^{n+1} + \frac{1}{\rho^{n+1}}f^{n+1},\end{aligned} \tag{3.10a}$$

$$\nabla\cdot\hat{\mathbf{u}}^{n+1} = 0, \tag{3.10b}$$

$$\mathbf{n}\cdot\hat{\mathbf{u}}^{n+1} = \mathbf{n}\cdot\mathbf{w}^{n+1} \quad on \quad \partial\Omega \tag{3.10c}$$

For velocity $\mathbf{u}^{n+1}$:

$$\frac{\gamma_0\mathbf{u}^{n+1} - \gamma_0\tilde{\mathbf{u}}^{n+1}}{\Delta t} - \nu_m\nabla^2\mathbf{u}^{n+1} = \nu_m\nabla\times\nabla\times\mathbf{u}^{*,n+1}, \tag{3.11a}$$

$$\mathbf{u}^{*,n+1} = \mathbf{w}^{*,n+1}, \quad on \quad \partial\Omega. \tag{3.11b}$$

In the above equations Δt is the time step size, $\tilde{\mathbf{u}}$ is an auxiliary variable approximating $\mathbf{u}^{n+1}$ and $\mathbf{D}(\mathbf{u}) = \nabla\mathbf{u} + \nabla\mathbf{u}^T$. If ζ denotes general variable, then ζ^n denotes the value of ζ at time step n and, $\zeta^{*,n+1}$ is a J-th order explicit approximation (where J is the temporal order and can be equal to 1 or 2 for this method) of ζ^{n+1}, given by:

$$\zeta^{*,n+1} = \begin{cases} \zeta^n, & if\ J = 1, \\ 2\zeta^n - \zeta^{n-1}, & if\ J = 2. \end{cases} \tag{3.12}$$

The expressions $\dfrac{1}{\Delta t}(\gamma_0\zeta^{n+1} - \hat{\zeta})$ and $\dfrac{1}{\Delta t}(\gamma_0\tilde{\zeta}^{n+1} - \hat{\zeta})$ denote the J-th order backward differentiation approximation of $\left.\dfrac{\delta\zeta}{\delta t}\right|^{n+1}$, where γ_0 and $\hat{\zeta}$ are given as follows:

$$\hat{\zeta} = \begin{cases} \zeta^n, & if\ J = 1, \\ 2\zeta^n - \frac{1}{2}\zeta^{n-1}, & if\ J = 2, \end{cases} \quad \gamma_0 = \begin{cases} 1, & if\ J = 1, \\ \frac{3}{2}, & if\ J = 2. \end{cases} \tag{3.13}$$

Also, ρ_0 is a constant which is given by $\rho_0 = min(\rho_1, \rho_2)$ and S is a specified constant that satisfies the condition:

$$S \geqslant \eta^2\sqrt{\frac{4\gamma_0}{\lambda\gamma_1\Delta t}} \tag{3.14}$$

ν_m is also a specified constant that satisfies the following condition:

$$\nu_m \geqslant \frac{1}{2}\left(\frac{\nu_1}{\rho_1} + \frac{\nu_2}{\rho_2}\right). \tag{3.15}$$

3.3 Hybrid Spectral Element-Fourier Spectral Discretization and Solution Algorithm

In this section, we focus on how to compute the field variables i.e velocity, pressure, and the phase field function based on the scheme represented by equations (3.9a)–(3.11b) on the 3D domain Ω having a homogeneous z direction. All field variables will be represented by a Fourier spectral expansion along the z direction and a C^0

spectral element expansion within the $x-y$ plane. Note that in the $x-y$ plane, the spectral element bases are real-valued functions and the Fourier bases contain complex functions in the homogeneous z direction. Therefore, the 3D basis and test functions will be complex-valued. Note that we have used the conjugate symmetry property of the Fourier transforms so that the number of Fourier modes will be equal to half the number of Fourier planes used in the homogeneous direction. For performing the spectral element discretizations we require the weak forms of the governing equations. Therefore we first discuss several integral relations which involve the 3D basis and test functions, so that we can use them readily in the subsequent discussions.

Let N_z denote the number of modes in the Fourier spectral expansion in z direction. Let $\Phi_k(z)$ $(-\frac{N_z}{2} \leqslant k \leqslant \frac{N_z}{2}-1)$ denote the k-th Fourier basis function in z, given by

$$\Phi_k(z) = e^{i\beta_k z}, \quad \beta_k = \frac{2\pi k}{L_z}, \quad -\frac{N_z}{2} \leqslant k \leqslant \frac{N_z}{2} - 1. \tag{3.16}$$

The following property holds,

$$\int_0^{L_z} \bar{\Phi}_k(z)\Phi_m(z)dz = L_z\delta_{km}, \quad -\frac{N_z}{2} \leqslant k, m \leqslant \frac{N_z}{2} - 1, \tag{3.17}$$

where the overbar in $\bar{\Phi}_k$ denotes the complex conjugate of Φ_k, and δ_{km} is the Kronecker delta.

Let $f(z)$ denote a generic scalar field function on Ω that is periodic in z with a period L_z. Note that its dependence on x and y have been suppressed for brevity. The Fourier expansion is

$$f(z) = \sum_{k=-\frac{N_z}{2}}^{\frac{N_z}{2}-1} \hat{f}_k \Phi_k(z) \tag{3.18}$$

where $\hat{f}_k$ denotes the k-th Fourier mode of $f(z)$. The following relations can be readily verified based on (3.16)–(3.18):

$$\begin{cases} \displaystyle\int_0^{L_z} f(z)\bar{\Phi}_k(z)dz = L_z\hat{f}_k, \\ \displaystyle\int_0^{L_z} f(z)\frac{\partial\bar{\Phi}_k}{\partial z}dz = -i\beta_k\hat{f}_k L_z, \\ \displaystyle\int_0^{L_z} \frac{\partial f}{\partial z}\bar{\Phi}_k(z)dz = i\beta_k\hat{f}_k L_z, \\ \displaystyle\int_0^{L_z} \frac{\partial f}{\partial z}\frac{\partial\bar{\Phi}_k}{\partial z}dz = \beta_k^2\hat{f}_k L_z, \quad -\dfrac{N_z}{2} \leqslant k \leqslant \dfrac{N_z}{2} - 1. \end{cases} \tag{3.19}$$

Let $\varphi(\vec{x})$, where $\vec{x} = (x, y)$, denote an arbitrary real test (basis) function in the 2D $x - y$ plane. Then the 3D basis functions and test functions are respectively

$$\begin{cases} Q_k(\vec{x}, z) = \varphi(\vec{x})\Phi_k(z), \quad -\dfrac{N_z}{2} \leqslant k \leqslant \dfrac{N_z}{2} - 1; \quad \text{(basis function)} \\ \bar{Q}_k(\vec{x}, z) = \varphi(\vec{x})\bar{\Phi}_k(z), \quad -\dfrac{N_z}{2} \leqslant k \leqslant \dfrac{N_z}{2} - 1. \quad \text{(test function)} \end{cases} \tag{3.20}$$

We represent the gradient in 3D as $\nabla = \left(\nabla_{2D}, \frac{\partial}{\partial z}\right)$, where ∇_{2D} denotes the gradient in the 2D $x - y$ plane and is given by $\nabla_{2D} = \frac{\partial}{\partial \vec{x}} = \left(\frac{\partial}{\partial x}, \frac{\partial}{\partial y}\right)$. Based on the equations (3.18)–(3.19) we can verify the following relations:

$$\begin{cases} \displaystyle\int_\Omega f(\vec{x}, z)\bar{Q}_k(\vec{x}, z)d\Omega = L_z \int_{\Omega_{2D}} \hat{f}_k(\vec{x})\varphi(\vec{x})d\Omega_{2D}, \\ \displaystyle\int_\Omega \nabla f \cdot \nabla\bar{Q}_k d\Omega = L_z \int_{\Omega_{2D}} \left(\nabla_{2D}\hat{f}_k \cdot \nabla_{2D}\varphi + \beta_k^2\hat{f}_k\varphi\right) d\Omega_{2D} \\ \displaystyle\int_{\partial\Omega} f(\vec{x}, z)\bar{Q}_k(\vec{x}, z)dA = L_z \int_{\partial\Omega_{2D}} \hat{f}_k(\vec{x})\varphi(\vec{x})dA, \end{cases} \tag{3.21}$$

where $d\Omega = d\Omega_{2D}dz = d\vec{x}dz = dxdydz$.

Let $\boldsymbol{\chi}(\vec{x}, z) = (\boldsymbol{\chi}_{2D}, \chi_z) = (\chi_x, \chi_y, \chi_z)$ denote a generic vector-valued field function on Ω that is periodic in z with a period L_z, and $\boldsymbol{\chi}_{2D}$ denote its component vector in the 2D $x-y$ plane. Then the following relations hold based on equations (3.18)–(3.19):

$$\begin{cases} \displaystyle\int_\Omega \boldsymbol{\chi} \cdot \nabla\bar{Q}_k d\Omega = L_z \left(\int_{\Omega_{2D}} \hat{\boldsymbol{\chi}}_{2D,k} \cdot \nabla_{2D}\varphi d\Omega_{2D} - i\beta_k \int_{\Omega_{2D}} \hat{\chi}_{z,k}\varphi d\Omega_{2D}\right), \\ \displaystyle\int_{\partial\Omega} (\mathbf{n} \cdot \boldsymbol{\chi})\bar{Q}_k dA = L_z \int_{\partial\Omega_{2D}} \mathbf{n}_{2D} \cdot \hat{\boldsymbol{\chi}}_{2D,k}\varphi dA, \quad -\dfrac{N_z}{2} \leqslant k \leqslant \dfrac{N_z}{2} - 1 \end{cases} \tag{3.22}$$

where $\mathbf{n} = (\mathbf{n}_{2D}, 0)$, and $\hat{\boldsymbol{\chi}}_{2D,k}$ and $\hat{\chi}_{z,k}$ are the Fourier expansion coefficients of $\boldsymbol{\chi}_{2D}$ and χ_z, respectively.

We can now discuss the process of discretization and obtaining the solution for the field variables $(\phi, \mathbf{u}, P)$.

Phase Field Function Equation (3.9a) can be written as

$$\nabla^2 \left[\nabla^2 \phi^{n+1} - \frac{S}{\eta^2} \phi^{n+1} \right] + \frac{\gamma_0}{\lambda \gamma_1 \Delta t} \phi^{n+1} = R_1 + \nabla^2 R_2 = R \tag{3.23}$$

where

$$\begin{cases} R_1 = \dfrac{1}{\lambda \gamma_1} \left[g^{n+1} - \mathbf{u}^{*,n+1} \cdot \nabla \phi^{*,n+1} + \dfrac{\hat{\phi}}{\Delta t} \right] \\ R_2 = h(\phi)^{*,n+1} - \dfrac{S}{\eta^2} \phi^{*,n+1}. \end{cases} \tag{3.24}$$

Under the condition (3.14) for the constant S,we can reformulate equation (3.23) into two de-coupled Helmholtz type equations given by (see [54, 60] for details),

$$\nabla^2 \psi^{n+1} - \left(\alpha + \frac{S}{\eta^2} \right) \psi^{n+1} = R, \tag{3.25a}$$

$$\nabla^2 \phi^{n+1} + \alpha \phi^{n+1} = \psi^{n+1}, \tag{3.25b}$$

where ψ^{n+1} is an auxiliary variable defined by equation (3.25b) and the constant α is given by $\alpha = -\frac{S}{2\eta^2} \left(1 + \sqrt{1 - \frac{4\gamma_0}{\lambda \gamma_1 \Delta t} \frac{\eta^4}{S^2}} \right)$. Using equations (3.9c) and (3.25b), we can transform the boundary condition (3.9b) as follows:

$$\mathbf{n} \cdot \nabla \psi^{n+1} = \mathbf{n} \cdot \nabla R_2 - \left(\alpha + \frac{S}{\eta^2} \right) \left[\frac{1}{\lambda} f_w'(\phi^{*,n+1}) + g_b^{n+1} \right] + g_c^{n+1}, \quad on \quad \partial\Omega \tag{3.26}$$

We now take the L^2 inner product between the 3D test function, $\bar{Q}_k(\vec{x}, z) = \varphi(\vec{x}) \bar{\Phi}_k(z)$ ($\varphi(\vec{x})$ denoting an arbitrary 2D test function), and equation (3.25a), and integrate by part. This leads to

$$\begin{aligned} &\int_\Omega \nabla \psi^{n+1} \cdot \nabla \bar{Q}_k + \left(\alpha + \frac{S}{\eta^2} \right) \int_\Omega \psi^{n+1} \bar{Q}_k = -\int_\Omega R_1 \bar{Q}_k + \int_\Omega \nabla R_2 \cdot \nabla \bar{Q}_k \\ &+ \int_{\partial\Omega} \left[-\left(\alpha + \frac{S}{\eta^2} \right) \left(\frac{1}{\lambda} f_w'(\phi^{*,n+1}) + g_b^{n+1} \right) + g_c^{n+1} \right] \bar{Q}_k, \quad -\frac{N_z}{2} \leqslant k \leqslant \frac{N_z}{2} - 1, \quad \forall \varphi \end{aligned} \tag{3.27}$$

where equation (3.26) has been used. Perform the Fourier spectral expansion of ψ^{n+1} in z, $\psi^{n+1} = \sum_{k=-N_z/2}^{N_z/2-1} \hat{\psi}_k^{n+1}(\vec{x})\Phi_k(z)$. By using the relations (3.19)–(3.21), equation (3.27) can be reduced into

$$\int_{\Omega_{2D}} \nabla_{2D}\hat{\psi}_k \cdot \nabla_{2D}\varphi + \left(\alpha + \frac{S}{\eta^2} + \beta_k^2\right) \int_{\Omega_{2D}} \hat{\psi}_k\varphi = \int_{\Omega_{2D}} \left(\beta_k^2 \hat{R}_{2,k} - \hat{R}_{1,k}\right)\varphi + \int_{\Omega_{2D}} \nabla_{2D}\hat{R}_{2,k} \cdot \nabla_{2D}\varphi + \int_{\partial\Omega_{2D}} \hat{\mathcal{T}}_k\varphi, \quad -\frac{N_z}{2} \leqslant k \leqslant \frac{N_z}{2} - 1, \quad \forall\varphi \quad (3.28)$$

where $\hat{R}_{1,k}$ and $\hat{R}_{2,k}$ are the Fourier coefficients of R_1 and R_2, respectively, and $\hat{\mathcal{T}}_k$ is the Fourier coefficient of the variable $\mathcal{T}$ given by

$$\mathcal{T} = -\left(\alpha + \frac{S}{\eta^2}\right)\left(\frac{1}{\lambda} f_w'(\phi^{*,n+1}) + g_b^{n+1}\right) + g_c^{n+1}. \quad (3.29)$$

Equation (3.28) is the weak form of a Helmholtz type equation about the N_z Fourier modes $\hat{\psi}_k$ in the 2D plane. It is noted that we can explicitly calculate the terms on the right hand side(RHS) of the equation (3.28) and also note that the different Fourier modes are not coupled in the computations.

Taking the L^2 inner product between 3D test function $\bar{Q}_k$ and equation (3.25b) and integrating by part, we have

$$\int_{\Omega} \nabla\phi^{n+1} \cdot \nabla\bar{Q}_k - \alpha \int_{\Omega} \phi^{n+1}\bar{Q}_k = -\int_{\Omega} \psi^{n+1}\bar{Q}_k - \int_{\partial\Omega} \left[\frac{1}{\lambda} f_w'(\phi^{*,n+1}) + g_b^{n+1}\right] \bar{Q}_k, \quad -\frac{N_z}{2} \leqslant k \leqslant \frac{N_z}{2} - 1, \quad \forall\varphi \quad (3.30)$$

where we have used the boundary condition (3.9c). By using the relations (3.19)–(3.21), this equation is reduced to

$$\int_{\Omega_{2D}} \nabla_{2D}\hat{\phi}_k^{n+1}\nabla_{2D}\varphi + \left(-\alpha + \beta_k^2\right) \int_{\Omega_{2D}} \hat{\phi}_k^{n+1}\varphi = -\int_{\Omega_{2D}} \hat{\psi}_k^{n+1}\varphi - \int_{\partial\Omega_{2D}} \hat{\mathcal{M}}_k\varphi, \quad -\frac{N_z}{2} \leqslant k \leqslant \frac{N_z}{2} - 1, \quad \forall\varphi \quad (3.31)$$

where $\hat{\phi}_k^{n+1}$ are the Fourier coefficients of ϕ^{n+1}, and $\hat{\mathcal{M}}_k$ are the Fourier coefficients of the variable $\mathcal{M}$ defined by $\mathcal{M} = \frac{1}{\lambda} f_w'(\phi^{*,n+1}) + g_b^{n+1}$. Equation (3.31) is the weak

form about the N_z Fourier modes $\hat{\phi}_k^{n+1}$ in the 2D $x-y$ plane. Once $\hat{\psi}_k^{n+1}$ are known by solving (3.28), (3.31) can be solved for $\hat{\phi}_k^{n+1}$. It is noted that the different Fourier modes are de-coupled from one another.

Therefore to compute the phase field function, we perform the following two steps: (i) solve equation (3.28) for the $\hat{\psi}_k^{n+1}$, $-N_z/2 \leqslant k \leqslant N_z/2-1$; (ii) solve equation (3.31) for the $\hat{\phi}_k^{n+1}$, $-N_z/2 \leqslant k \leqslant N_z/2-1$.

Pressure Take the L^2 inner product between equation (3.10a) and $\nabla\bar{Q}_k$, where $\bar{Q}_k(\vec{x},z)$ denotes the 3D test function, and we get

$$\int_\Omega \nabla P^{n+1}\cdot\nabla\bar{Q}_k = \rho_0\int_\Omega \mathbf{T}\cdot\nabla\bar{Q}_k - \rho_0\int_{\partial\Omega}\frac{\mu^{n+1}}{\rho^{n+1}}\mathbf{n}\times\omega^{*,n+1}\cdot\nabla\bar{Q}_k - \frac{\rho_0\gamma_0}{\Delta t}\int_{\partial\Omega}\mathbf{n}\cdot\mathbf{w}^{n+1}\bar{Q}_k, \quad -\frac{N_z}{2}\leqslant k\leqslant\frac{N_z}{2}, \quad \forall\varphi \quad (3.32)$$

where $\boldsymbol{\omega}=\nabla\times\mathbf{u}$ is the vorticity, and we have used integration by part, equation (3.10c) and the identity $\frac{\mu}{\rho}\nabla\times\boldsymbol{\omega}\cdot\nabla\bar{Q}_k = \nabla\cdot\left(\frac{\mu}{\rho}\boldsymbol{\omega}\times\nabla\bar{Q}_k\right) - \nabla\left(\frac{\mu}{\rho}\right)\times\boldsymbol{\omega}\cdot\bar{Q}_k$. In this equation,

$$\mathbf{T} = \frac{1}{\rho^{n+1}}\left[\mathbf{f}^{n+1} - \lambda(\psi^{n-1}-\alpha\phi^{n+1})\nabla\phi^{n+1} + \nabla\mu^{n+1}\cdot\mathbf{D}(\mathbf{u}^{*,n+1})\right] + \frac{\hat{\mathbf{u}}}{\Delta t} - \mathbf{u}^{*,n+1}\cdot\nabla\mathbf{u}^{*,n+1} + \left(\frac{1}{\rho_0}-\frac{1}{\rho^{n+1}}\right)\nabla P^{*,n+1} + \nabla\left(\frac{\mu^{n+1}}{\rho^{n+1}}\right)\times\boldsymbol{\omega}^{*,n+1}. \quad (3.33)$$

where we have used equation (3.25b).

Let $\mathbf{J}^{n+1} = (\mathbf{J}_{2D}, J_z) = (J_x, J_y, J_z) = \frac{\mu^{n+1}}{\rho^{n+1}}\mathbf{n}\times\boldsymbol{\omega}^{*,n+1}$ defined on $\partial\Omega$. In light of the relations (3.19)–(3.21), equation (3.32) is reduced to

$$\int_{\Omega_{2D}}\nabla_{2D}\hat{P}_k^{n+1}\cdot\nabla_{2D}\varphi + \beta_k^2\int_{\Omega_{2D}}\hat{P}_k^{n+1}\varphi = \rho_0\int_{\Omega_{2D}}\hat{\mathbf{T}}_{2D,k}\cdot\nabla_{2D}\varphi - i\beta_k\rho_0\int_{\Omega_{2D}}\hat{T}_{z,k}\varphi - \rho_0\int_{\partial\Omega_{2D}}\hat{\mathbf{J}}_{2D,k}^{n+1}\cdot\nabla_{2D}\varphi + i\beta_k\rho_0\int_{\partial\Omega_{2D}}\hat{J}_{z,k}^{n+1}\varphi - \frac{\gamma_0\rho_0}{\Delta t}\int_{\partial\Omega_{2D}}\mathbf{n}_{2D}\cdot\hat{\mathbf{w}}_{2D,k}^{n+1}\varphi, \quad -\frac{N_z}{2}\leqslant k\leqslant\frac{N_z}{2}-1, \quad \forall\varphi \quad (3.34)$$

where $\hat{P}_k^{n+1}$ are the Fourier coefficients of P^{n+1}, $(\hat{\mathbf{T}}_{2D,k}, \hat{T}_{z,k})$ are the Fourier coefficients of $\mathbf{T}^{n+1}$, and $(\hat{\mathbf{J}}_{2D,k}^{n+1}, J_{z,k}^{n+1})$ are the Fourier coefficients of $\mathbf{J}^{n+1}$. This equation is

the weak form about the N_z Fourier modes of the pressure $\hat{P}_k^{n+1}$ in the 2D $x-y$ plane. The terms on RHS can be computed explicitly once ϕ^{n+1} and ψ^{n+1} are computed. To avoid the computing the convolution of the higher order terms in $\mathbf{T}$ and $\mathbf{J}^{n+1}$, we first compute these terms in the physical space, which can then be transformed into the Fourier space for computing the RHS of the equation (3.34).

It should be noted that due to the presence of $i\beta_k$ terms on the RHS of (3.34), the real part (resp. imaginary part) of $\hat{P}_k^{n+1}$ will be affected by the imaginary part (resp. real part) of $\hat{T}_{z,k}$ and $\hat{J}_{z,k}^{n+1}$.

Velocity Summing up equations (3.10a) and (3.11a) leads to

$$\frac{\gamma_0}{\nu_m \Delta t}\mathbf{u}^{n+1} - \nabla^2 \mathbf{u}^{n+1} = \frac{1}{\nu_m}\left[\mathbf{Y} - \nabla\left(\frac{\mu^{n+1}}{\rho^{n+1}}\right) \times \boldsymbol{\omega}^{*,n+1}\right] - \frac{1}{\nu_m}\left(\frac{\mu^{n+1}}{\rho^{n+1}} - \nu_m\right)\nabla \times \boldsymbol{\omega}^{*,n+1} \tag{3.35}$$

where

$$\mathbf{Y} = \mathbf{T} - \frac{1}{\rho_0}\nabla P^{n+1} \tag{3.36}$$

and $\mathbf{T}$ is given by (3.33).

Let $\varphi^{(0)}(\vec{x})$ denote an arbitrary test function in the 2D $x-y$ plane that vanishes on $\partial\Omega_{2D}$, i.e. $\varphi^{(0)}\big|_{\partial\Omega_{2D}} = 0$, and define the test function for 3D

$$\bar{Q}_k^{(0)}(\vec{x}, z) = \varphi^{(0)}(\vec{x})\bar{\Phi}_k(z), \quad -\frac{N_z}{2} \leqslant k \leqslant \frac{N_z}{2} - 1. \tag{3.37}$$

Note that $\bar{Q}_k^{(0)}\Big|_{\partial\Omega} = 0$. Take the L^2 inner product between equation (3.35) and the 3D test function $\bar{Q}_k^{(0)}$, and we have

$$\begin{aligned}\frac{\gamma_0}{\nu_m \Delta t}\int_\Omega \mathbf{u}^{n+1}\bar{Q}_k^{(0)} + \int_\Omega \nabla\bar{Q}_k^{(0)}\cdot\nabla\mathbf{u}^{n+1} = \frac{1}{\nu_m}\int_\Omega \mathbf{Y}\bar{Q}_k^{(0)} - \frac{1}{\nu_m}\int_\Omega\left(\frac{\mu^{n+1}}{\rho^{n+1}} - \nu_m\right)\boldsymbol{\omega}^{*,n+1}\times\nabla\bar{Q}_k^{(0)}, \\ -\frac{N_z}{2} \leqslant k \leqslant \frac{N_z}{2} - 1, \quad \forall\varphi^{(0)}|_{\partial\Omega_{2D}} = 0\end{aligned} \tag{3.38}$$

where we have used integration by part, the property that $\bar{Q}_k^{(0)}\Big|_{\partial\Omega} = 0$, and the identity ($\kappa$ and ξ denoting two scalar functions), $\int_\Omega(\nabla\times\boldsymbol{\omega})\kappa\xi = \int_{\partial\Omega}(\mathbf{n}\times\boldsymbol{\omega})\kappa\xi + \int_\Omega(\boldsymbol{\omega}\times\nabla\kappa)\xi + \int_\Omega(\boldsymbol{\omega}\times\nabla\xi)\kappa$.

Let

$$\mathbf{K}^{n+1} = \left(\frac{\mu^{n+1}}{\rho^{n+1}} - \nu_m\right) \boldsymbol{\omega}^{*,n+1} \tag{3.39}$$

and define ($f(\vec{x})$ denoting a generic function in x-y plane)

$$\nabla_3 = (\nabla_{2D}, -i\beta_k), \quad \nabla_3 f = (\nabla_{2D} f, -i\beta_k f). \tag{3.40}$$

Then the last term on the RHS of equation (3.38) can be transformed into

$$\begin{aligned}\int_\Omega \mathbf{K}^{n+1} \times \nabla \bar{Q}_k^{(0)} &= \sum_{m=-N_z/2}^{N_z/2-1} \left(\int_{\Omega_{2D}} \hat{\mathbf{K}}_m^{n+1} \times \nabla_3 \varphi^{(0)}\right) \left(\int_0^{L_z} \Phi_m(z)\bar{\Phi}_k(z)\right) \\ &= L_z \int_{\Omega_{2D}} \hat{\mathbf{K}}_k^{n+1} \times \nabla_3 \varphi^{(0)}\end{aligned} \tag{3.41}$$

where $\hat{\mathbf{K}}_k^{n+1}$ is the Fourier expansion coefficients of $\mathbf{K}^{n+1}$, and we have used the equation (3.17).

By using the relations (3.19)–(3.21) and (3.41), we can reduce equation (3.38) into

$$\begin{aligned}\left(\frac{\gamma_0}{\nu_m \Delta t} + \beta_k^2\right) \int_{\Omega_{2D}} \hat{\mathbf{u}}_k^{n+1} \varphi^{(0)} + \int_{\Omega_{2D}} \nabla_{2D} \varphi^{(0)} \cdot \nabla \hat{\mathbf{u}}_k^{n+1} = \frac{1}{\nu_m} \int_{\Omega_{2D}} \hat{\mathbf{Y}}_k \varphi^{(0)} \\ - \frac{1}{\nu_m} \int_{\Omega_{2D}} \hat{\mathbf{K}}_k^{n+1} \times \nabla_3 \varphi^{(0)}, \quad -\frac{N_z}{2} \leqslant k \leqslant \frac{N_z}{2} - 1, \quad \forall \varphi^{(0)}|_{\partial\Omega_{2D}} = 0,\end{aligned} \tag{3.42}$$

where $\hat{\mathbf{u}}_k^{n+1}$ and $\hat{\mathbf{Y}}_k$ are the Fourier expansion coefficients of $\mathbf{u}^{n+1}$ and $\mathbf{Y}$, respectively. This is the weak form about the velocity Fourier modes $\hat{\mathbf{u}}_k^{n+1}$ in the 2D x-y plane. It is noted that the three velocity components are not coupled, and the different Fourier modes for any velocity component are also de-coupled. When computing the RHS of this equation, $\mathbf{Y}$ and $\mathbf{K}^{n+1}$ will be first computed in physical space based on equations (3.36) and (3.39), and then their Fourier coefficients can be calculated.

It should be noted that because $\nabla_3 \varphi^{(0)}$ involves an $i\beta_k$ term, the real parts (resp. imaginary parts) of $\hat{\mathbf{K}}_k^{n+1}$ will contribute to the imaginary parts (resp. real parts) of $\hat{\mathbf{u}}_k^{n+1}$. In addition, the cross product in the last term of equation (3.42) will mix up the contributions of this term to different velocity components.

Spectral Element Discretization in 2D x-y Plane Let us now discuss the discretization of the equations (3.28), (3.31), (3.34) and (3.42) using C^0 spectral

elements in the 2D domain Ω_{2D}. We partition Ω_{2D} with a spectral element mesh. Let $\Omega_{2D,h}$ denote the discretized Ω_{2D}, such that $\Omega_{2D,h} = \cup_{e=1}^{N_{el}} \Omega_{2D,h}^e$, where N_{el} is the number of elements in the mesh and $\Omega_{2D,h}^e$ $(1 \leqslant e \leqslant N_{el})$ denotes the element e. Let $\partial\Omega_{2D,h}$ denote the boundary of $\Omega_{2D,h}$. We use $\prod_K(\Omega_{2D,h}^e)$ to denote the linear space of polynomials of degree characterized by K, which will be referred to as the element order hereafter. Let $H^1(\Omega_{2D,h})$ denote the set of globally continuous and square-integrable functions defined on $\Omega_{2D,h}$. We define the following function spaces

$$\begin{cases} X_h = \left\{ \ v \in H^1(\Omega_{2D,h}) \ : \ v|_{\Omega_{2D,h}^e} \in \Pi_K(\Omega_{2D,h}^e), \ 1 \leqslant e \leqslant N_{el} \ \right\}, \\ X_{h0} = \left\{ \ v \in X_h \ : \ v|_{\partial\Omega_{2D,h}} = 0 \ \right\}. \end{cases} \tag{3.43}$$

In what follows, we use $(\cdot)_h$ to denote the discretized version of variable $(\cdot)$, and use $Re(\cdot)$ and $Im(\cdot)$ to denote the real and imaginary parts of a complex-valued variable $(\cdot)$. The fully discretized version of equation (3.28) reads: find $\hat{\psi}_{k,h}^{n+1}$ such that $Re(\hat{\psi}_{k,h}^{n+1}) \in X_h$ and $Im(\hat{\psi}_{k,h}^{n+1}) \in X_h$ and

$$\begin{aligned} &\int_{\Omega_{2D,h}} \nabla_{2D}\hat{\psi}_{kh}^{n+1} \cdot \nabla_{2D}\varphi_h + \left(\alpha + \frac{S}{\eta^2} + \beta_k^2\right) \int_{\Omega_{2D,h}} \hat{\psi}_{kh}^{n+1}\varphi_h = \int_{\Omega_{2D,h}} \left(\beta_k^2 \hat{R}_{2,kh} - \hat{R}_{1,kh}\right) \varphi_h \\ &+ \int_{\Omega_{2D,h}} \nabla_{2D,h}\hat{R}_{2,kh} \cdot \nabla_{2D}\varphi_h + \int_{\partial\Omega_{2D,h}} \hat{\mathcal{T}}_{kh}\varphi_h, \quad -\frac{N_z}{2} \leqslant k \leqslant \frac{N_z}{2} - 1, \quad \forall \varphi_h \in X_h. \end{aligned} \tag{3.44}$$

The fully discretized version of equation (3.31) reads: find $\hat{\phi}_{kh}^{n+1}$ such that $Re(\hat{\phi}_{kh}^{n+1}) \in X_h$ and $Im(\hat{\phi}_{kh}^{n+1}) \in X_h$ and

$$\begin{aligned} \int_{\Omega_{2D,h}} \nabla_{2D}\hat{\phi}_{kh}^{n+1} \nabla_{2D}\varphi_h + \left(-\alpha + \beta_k^2\right) \int_{\Omega_{2D,h}} \hat{\phi}_{kh}^{n+1}\varphi_h = -\int_{\Omega_{2D,h}} \hat{\psi}_{kh}^{n+1}\varphi_h - \int_{\partial\Omega_{2D,h}} \hat{\mathcal{M}}_{kh}\varphi_h, \\ -\frac{N_z}{2} \leqslant k \leqslant \frac{N_z}{2} - 1, \quad \forall \varphi_h \in X_h. \end{aligned} \tag{3.45}$$

The fully discretized version of equation (3.34) reads: find $\hat{P}_{kh}^{n+1}$ such that $Re(\hat{P}_{kh}^{n+1}) \in X_h$ and $Im(\hat{P}_{kh}^{n+1}) \in X_h$ and

$$\int_{\Omega_{2D,h}} \nabla_{2D}\hat{P}_{kh}^{n+1}\cdot\nabla_{2D}\varphi_h+\beta_k^2\int_{\Omega_{2D,h}} \hat{P}_{kh}^{n+1}\varphi_h = \rho_0\int_{\Omega_{2D,h}} \hat{\mathbf{T}}_{2D,kh}\cdot\nabla_{2D}\varphi_h - i\beta_k\rho_0\int_{\Omega_{2D,h}} \hat{T}_{z,kh}\varphi_h$$
$$-\rho_0\int_{\partial\Omega_{2D,h}} \hat{\mathbf{J}}_{2D,kh}^{n+1}\cdot\nabla_{2D}\varphi_h + i\beta_k\rho_0\int_{\partial\Omega_{2D,h}} \hat{J}_{z,kh}^{n+1}\varphi_h - \frac{\gamma_0\rho_0}{\Delta t}\int_{\partial\Omega_{2D,h}} \mathbf{n}_{2D,h}\cdot\hat{\mathbf{w}}_{2D,kh}^{n+1}\varphi_h,$$
$$-\frac{N_z}{2} \leqslant k \leqslant \frac{N_z}{2}-1, \quad \forall\varphi_h \in X_h. \quad (3.46)$$

The fully discretized version of equation (3.42) reads: find $\hat{\mathbf{u}}_k^{n+1}$ such that $Re(\hat{\mathbf{u}}_k^{n+1}) \in [X_h]^3$ and $Im(\hat{\mathbf{u}}_k^{n+1}) \in [X_h]^3$ and

$$\left(\frac{\gamma_0}{\nu_m\Delta t}+\beta_k^2\right)\int_{\Omega_{2D,h}} \hat{\mathbf{u}}_{kh}^{n+1}\varphi_h + \int_{\Omega_{2D,h}} \nabla_{2D}\varphi_h\cdot\nabla\hat{\mathbf{u}}_{kh}^{n+1} = \frac{1}{\nu_m}\int_{\Omega_{2D,h}} \hat{\mathbf{Y}}_{kh}\varphi_h$$
$$-\frac{1}{\nu_m}\int_{\Omega_{2D,h}} \hat{\mathbf{K}}_{kh}^{n+1}\times\nabla_3\varphi_h, \quad -\frac{N_z}{2} \leqslant k \leqslant \frac{N_z}{2}-1, \quad \forall\varphi_h \in X_{h0}. \quad (3.47)$$

The velocity Dirichlet boundary condition (3.11b) also needs to be discretized. Upon Fourier expansion in z direction, the fully discretized version of equation (3.11b) becomes

$$\hat{\mathbf{u}}_{kh}^{n+1} = \hat{\mathbf{w}}_{kh}^{n+1}, \quad -\frac{N_z}{2} \leqslant k \leqslant \frac{N_z}{2}-1, \quad \text{on } \partial\Omega_{2D,h} \quad (3.48)$$

where $\hat{\mathbf{w}}_{kh}^{n+1}$ are the Fourier expansion coefficients of the discretized boundary velocity $\mathbf{w}_h^{n+1}$.

Solution Algorithm Therefore if we know the values of (ϕ_h^n, P_h^n, $\mathbf{u}_h^n$) , we compute the physical variables at the next time step(i.e ϕ_h^{n+1}, P_h^{n+1}, $\mathbf{u}_h^{n+1}$) as follows:

- Solve equations (3.44) for $\hat{\psi}_{kh}^{n+1}$ ($-N_z/2 \leqslant k \leqslant N_z/2-1$);
- Solve equations (3.45) for $\hat{\phi}_{kh}^{n+1}$ ($-N_z/2 \leqslant k \leqslant N_z/2-1$);
- Solve equations (3.46) for $\hat{P}_{kh}^{n+1}$ ($-N_z/2 \leqslant k \leqslant N_z/2-1$);
- Solve equations (3.47), together with boundary condition (3.48), for $\hat{\mathbf{u}}_{kh}^{n+1}$ ($-N_z/2 \leqslant k \leqslant N_z/2-1$).

We can observe that all the equations to be solved using this numerical algorithm are 2D decoupled equations in the $x-y$ plane. This feature provides extensive opportunities for efficient parallel processing. It should also be noted that the linear algebraic systems resulting from these equations involve only constant coefficient matrices which can be precomputed.

3.4 Numerical tests for Two-Phase Flows

In this section we are going to demonstrate the performance of the method proposed in section 3.3 by conducting simulations for several two-phase flow problems. Note that when performing these simulations we consider flow domains(three-dimensional) which are homogeneous in at least one direction. In the first test problem, we illustrate the convergence rates of the method. In the second test problem, we are going to simulate a co-current two-phase flow to demonstrate the accuracy of the method. In the third test problem, we study the effects of the change in static contact angle on the equilibrium shape of a liquid drop on a wall. In the fourth test problem, we study the dynamics of a low-density liquid drop in a container filled with high-density liquid and also simulate the rise of an air bubble in water to demonstrate the capability of the method in dealing with realistic flows.

Before we analyze the results of the numerical simulations, we are going to briefly discuss the normalization of the governing equations and the physical variables and parameters. Note that the non-dimensional form of the governing equations, initial and boundary conditions will retain the same format as the dimensional form if the physical parameters and variables are normalized consistently [54, 84]. Let L, U_0 and ρ_d denote the characteristic length scale, velocity scale, and the density scale respectively. The physical variables and parameters used in the subsequent discussions are consistently normalized using Table 3.1 unless specified otherwise.

Table 3.1.: Normalization constants for physical variables and parameters. L, U_0 and ρ_d denote characteristic scales for the length, velocity and density, respectively.

Variables/parameters	Normalization constant
$\mathbf{x}$, x, y, z, η	L
t, Δt, $g(\mathbf{x}, t)$	L/U_0
$\mathbf{u}$, $\mathbf{w}$	U_0
ρ, ρ_1, ρ_2, ρ_0	ρ_d
μ, μ_1, μ_2	$\rho_d U_0 L$
P, p	$\rho_d U_0^2$
ψ	$1/L^2$
ϕ, θ_s, S, γ_0	1
σ	$\rho_d U_0^2 L$
λ	$\rho_d U_0^2 L^2$
γ_1	$L/(\rho_d U_0)$
$\mathbf{f}$	$\rho_d U_0^2/L$
g_c	L^3
g_b	$1/L$

3.4.1 Convergence Tests

The goal of this subsection is to study the spatial and temporal convergence rates of the method developed in Section 3.3 using a manufactured analytic solution to the governing equations (3.8),(3.2b) and (3.2c).

We consider the flow domain $\Omega = [(x, y, z) : 0 \leq x \leq 2, -1 \leq y \leq 1, 0 \leq z \leq 2]$ as illustrated in Figure 3.1.We use the following analytic solution for the flow variables:

$$\begin{cases} u = A\cos(ax)\cos(by)\cos(cz)\sin(\beta t) \\ v = 0 \\ w = \frac{Aa}{c}\sin(ax)\cos(by)\sin(cz)\sin(\beta t) \\ P = A\sin(ax)\sin(by)\sin(cz)\cos(\beta t) \\ \phi = A_1\cos(a_1 x)\cos(b_1 y)\cos(c_1 z)\sin(\beta_1 t) \end{cases} \tag{3.49}$$

where $A, A_1, b, c, a_1, b_1, c_1, \beta, \beta_1$ are user defined constants(given below), (u,v,w) are the (x, y, z) of the velocity $\mathbf{u}$. ϕ is the phase field function and $\mathbf{P}$ is the effective pressure. The body force terms and the source field terms such as, $\mathbf{f}$ in equation (3.2a), g in equation (3.2c), g_c in (3.4b), g_b in equation (3.4c) and $\mathbf{w}$ in equation (3.4a), are chosen in a way so that the analytical expressions in (3.49) satisfy the governing equations (3.8), (3.2b) and (3.2c), and also satisfy the boundary conditions (3.4a), (3.4b) and (3.4c).

We impose the Dirichlet boundary conditions for the velocity based on the expressions (3.49) and the contact angle boundary conditions (3.4b),(3.4c) for the phase field function on the faces $\overline{ABHG}$, $\overline{DCIJ}$, $\overline{ADKG}$ and $\overline{BCIH}$. We set the initial conditions for the velocity $\mathbf{u}$ and the phase field function ϕ equal to the values obtained by the analytic solution (3.49) at time $t = 0$.

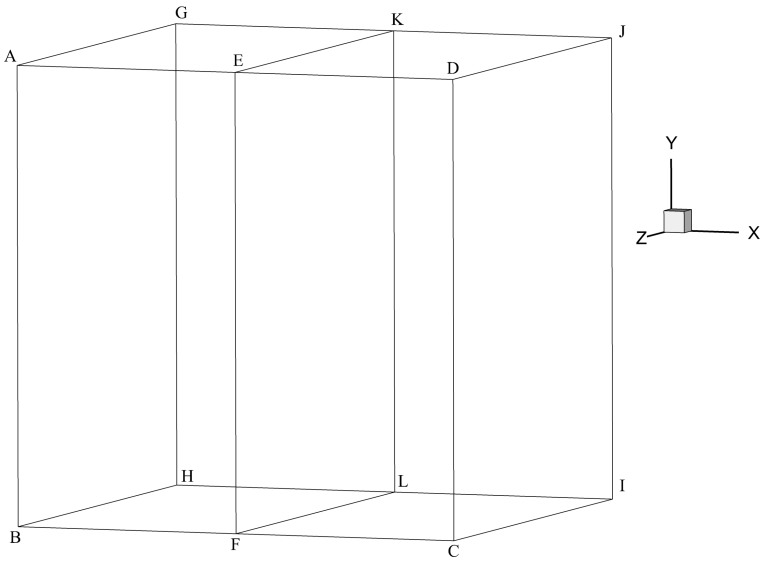

Figure 3.1.: Convergence rates: Test Domain.

The following parameters have been used when performing the subsequent simulations:

$$\begin{cases} A = 1.0,\ a = 1.0\,\pi,\ b = 1.5\,\pi,\ c = 1.0\,\pi,\ a_1 = b_1 = c_1 = 1.0\,\pi, \\ A_1 = 1.0,\ \beta = 1.0,\ \beta_1 = 1.0,\ \mu_1 = 0.01,\ \frac{\rho_2}{\rho_1} = 3.0,\ \frac{\mu_2}{\mu_1} = 2.0,\ J = 2, \\ \eta = 0.1,\ \lambda = 0.001,\ \gamma = 0.001,\ \theta_s = 60^0, \\ \nu_m^* = \dfrac{1}{2}\left(\dfrac{\mu_1}{\rho_1} + \dfrac{\mu_2}{\rho_2}\right) = 8.333 \times 10^{-3},\ \rho_0 = min(\rho_1, \rho_2) = 1.0, \end{cases} \tag{3.50}$$

To simulate this problem we discretize the domain Ω into 8 Fourier planes along the z-direction, and we further divide each Fourier plane along the x-direction into two quadrilateral spectral elements of equal sizes as shown in Figure 3.1. When performing the spatial and temporal convergence tests, we run the simulations from time t=0 to a specified time t=t_f, after which we calculate the numerical errors by comparing the numerical results with the analytical solution(3.49) at the final time t=t_f.

Spatial Convergence Test To determine the spatial convergence rate of the proposed method, we use a fixed time step size Δt=0.001 and set the total integration time t_f=0.1. Then we perform simulations by increasing the element order from 2 to 20 sequentially in steps of 2 and obtain the numerical errors of the flow variables for each element order. Figure 3.2 shows the L^∞ and L^2 errors of the velocity, pressure and the phase field function ϕ as a function of the element order for the spatial convergence test. We observe that the numerical errors for the flow variables decrease exponentially when the element order increases from 2 to 16. However, when the element order increases beyond 16, we can observe that the errors do not further decrease. The reason for this being that at high element orders the total error is dominated by the temporal truncation error.

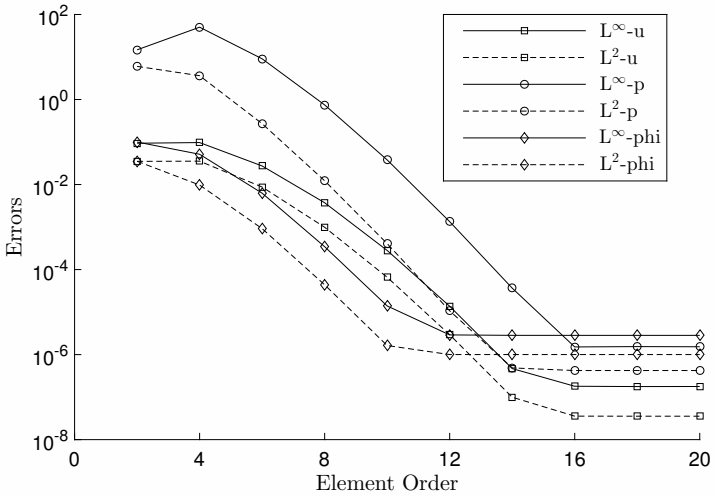

Figure 3.2.: Spatial Convergence rate: L^∞ and L^2 errors as a function of element order with fixed Δt=0.001.

Temporal Convergence Test To determine the temporal convergence rate of the proposed method, we first set the element order to 16 based on the results from the spatial convergence test and also set the total integration time $t_f = 0.5$. Then, we perform simulations by reducing the time step size from Δt=0.1 to Δt=0.0015625 sequentially by a factor of 0.5 and obtain the numerical errors for each time step

size. Figure 3.3 shows the L^∞ and L^2 errors of the velocity, pressure and the phase field function ϕ as a function of the time step size Δt for the temporal convergence test. We can observe that the numerical method has a second-order convergence in time for all the flow variables. Note that when the time step size becomes very small (around $\Delta t = 0.001$) the rate of change in errors (see the L^∞ errors of the pressure and velocity) starts to decrease since the total error will be dominated by the spatial truncation error at these small time steps.

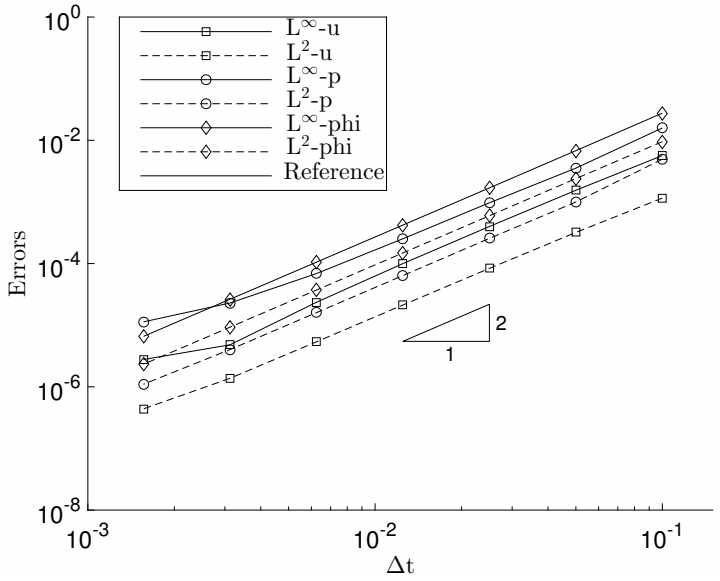

Figure 3.3.: Temporal convergence rate: L^∞ and L^2 errors as a function of Δt with a fixed element order 16.

The above results indicate that the proposed numerical method has a spatial exponential and a temporal second-order convergence rate for three-dimensional problems.

3.4.2 Co-Current Flow of Two Immiscible Fluids in a Pipe

In this subsection, we use the method proposed in section 3.3 to simulate a fully developed laminar co-current flow of two immiscible fluids in a circular pipe. The goal of this test is to demonstrate the accuracy of the proposed method in simulating

steady-state homogeneous two-phase flows, by comparing the simulation results at the steady state with the analytical solution.

We consider a flow domain as illustrated in Figure 3.4, defined by $\Omega = [(x, y, z) : 0 \leq \sqrt{x^2 + y^2} \leq r_2, 0 \leq z \leq \frac{4}{5} r_2]$, where r_2 is the radius of the circular pipe. The first fluid flows in the region $0 \leqslant r \leqslant r_1$ and has a viscosity μ_1. The second fluid flows in the region $r1 \leqslant r \leqslant r_2$ and has a viscosity μ_2. Note that since the flow is fully developed, we only have an axial flow in the pipe. The viscosity of the first and second fluid is given by μ_1, μ_2 respectively. The interfacial instabilities and the gravitational effects are neglected. Also, the two-fluids are assumed to have the same density ρ. The analytical solution to the axial velocity profile for the two fluids as a function of the radial distance(r) is given by (refer to [85]):

$$\frac{w_1(r)}{\bar{w}} = \frac{1 - \delta^2 + \hat{\mu}(\delta^2 - R^2)}{\delta^4(\hat{\mu} - 1) + 1}, \; 0 \leq R \leq \delta \tag{3.51a}$$

$$\frac{w_2(r)}{\bar{w}} = \frac{1 - R^2}{\delta^4(\hat{\mu} - 1) + 1}, \qquad \delta \leq R \leq 1 \tag{3.51b}$$

where w_1 and w_2 represent the axial velocity of the first and second fluid respectively and

$$R = \frac{r}{r_2}; \; \hat{\mu} = \frac{\mu_2}{\mu_1}; \delta = \frac{r_1}{r_2} \tag{3.52}$$

Also, the term $\hat{w}$ is the average flow velocity and is given by:

$$\bar{w} = \frac{\bar{K} r_2^2}{8\mu_2} \left\{ \delta^4(\hat{\mu} - 1) + 1 \right\} \tag{3.53}$$

where $\bar{K}$ is the axial pressure gradient term.

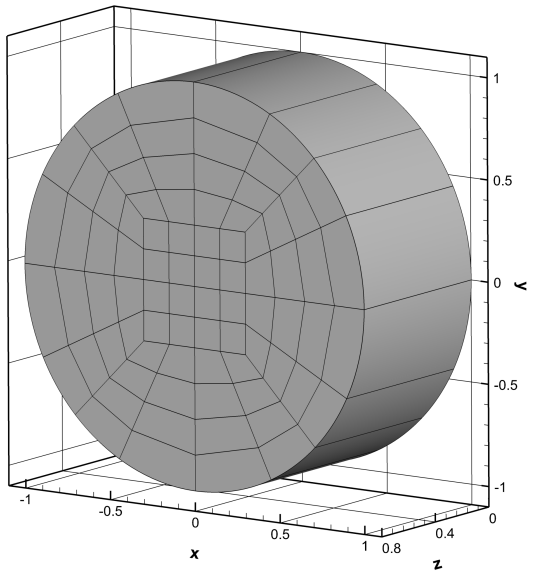

Figure 3.4.: Geometry and mesh of co-current pipe flow with 80 elements in each Fourier plane

We choose the radius of the pipe r_2 as the characteristic length scale, and use the fluid density ρ as the characteristic density scale $\rho_d = \rho_1 = 1kg/m^3$ and set the characteristic velocity scale $U_0 = 10\sqrt{|\bar{K}|L}$, where $|\bar{K}|$ is the absolute value of the pressure gradient in the axial direction. The physical variables and parameters are then normalized using appropriate normalization constants given in Table 3.1.

The flow domain is discretized into 16 Fourier planes along the z-direction and each Fourier plane is further divided into 80 elements in the $x - y$ plane as shown in Figure 3.4. We do not compute the phase field function for this test problem since the surface tension is assumed to be zero. Instead we simply set $\phi(\mathbf{x}) = -tanh\frac{\sqrt{x^2+y^2}-r_1}{\sqrt{2}\eta}$. However, the initial velocity field is set to $\mathbf{u(x,0)}_{in} = 0$ and the simulations are performed till the flow reaches a steady-state.

The following parameters have been used to perform the subsequent simulations in this subsection unless stated explicitly otherwise:

$$\begin{cases} r_1 = 0.5,\ r_2 = 1, \mu_1 = 0.01\ \frac{\mu_2}{\mu_1} = 6; \bar{K} = -0.01, \\ \eta = 0.0005,\ J = 2,\ element\, order = 10, \\ \Delta t = 5 \times 10^{-5},\ \rho_1 = \rho_2 = 1,\ \rho_0 = min(\rho_1, \rho_2) = 1.0. \end{cases} \tag{3.54}$$

Effect of interfacial thickness scale η To study the effect of the parameter η we have performed numerical simulations for various values of η ranging between $\eta = 0.0005$ to $\eta = 0.01$. Figure 3.13 shows the axial velocity profiles for different cases of η obtained from the simulations at steady state. From these velocity profiles, we observe that the magnitude of the peak axial velocity increases initially when η is decreased from 0.01. However, when η becomes small enough (around $\eta = 0.001$), the velocity profile remains unchanged for further decrease in η.

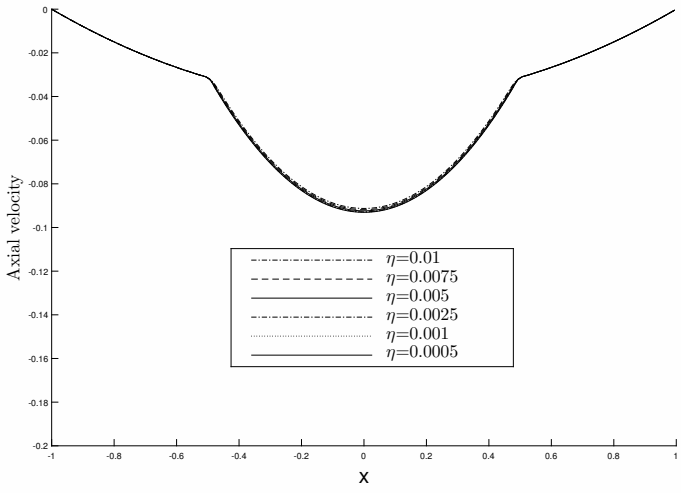

Figure 3.5.: Co-current flow: Steady state axial velocity profiles obtained for different interfacial thickness scale η.

Effect of the element order The goal of this test is to study the effect of the element order on the axial velocity profile obtained at steady state. To perform

this test, we fixed the value of η to 0.0005 (based on the results from the interfacial thickness scale test) and then performed simulations for three element orders 10, 12 and 14. Figure 3.6 shows the effect of the element order on the axial-velocity profile obtained from the simulations at steady state. We observe that the velocity profiles are almost identical for the three cases.

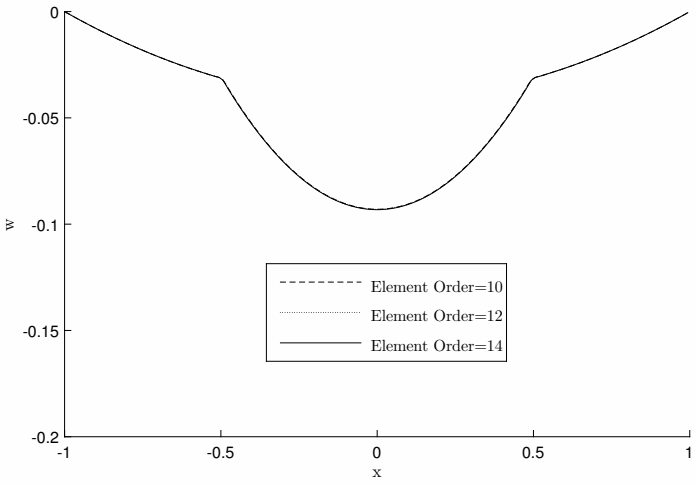

Figure 3.6.: Co-current flow: Steady state axial velocity profiles obtained for different element order.

To demonstrate the accuracy of the scheme we have compared the steady-state axial velocity profile obtained from the simulations with the theoretical profile. For this test, we have used an element order=14 and $\eta = 0.0005$. Figure 3.7 shows the axial-velocity profiles obtained from the simulations at steady state and the analytic solution. We observe that the velocity profile obtained from the simulations is identical to the theoretical predictions.

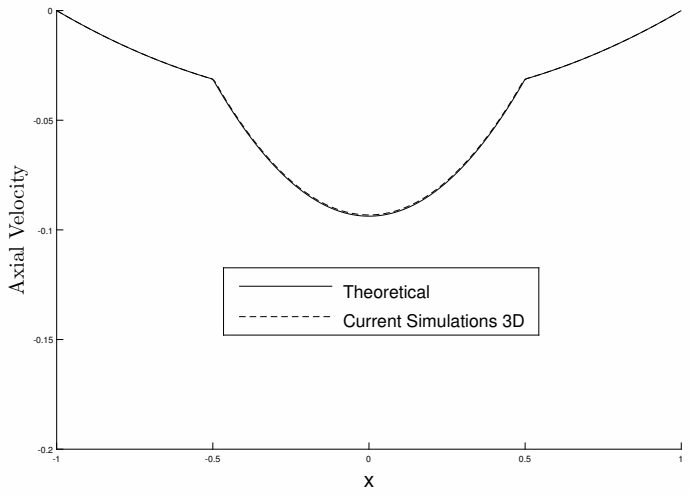

Figure 3.7.: Co-current Flow(80 elements in each Fourier plane): Comparison of the axial velocity profile between the simulation results and the theoretical profile.

We have also performed a similar simulation in which the domain is discretized into 16 Fourier planes along the homogeneous direction and each plane is further divided into 256 quadrilateral elements as shown in Figure 3.8. However, when performing the simulations using this mesh we have set the initial velocity profile to the analytical expressions (3.51a), (3.51b) instead of starting from zero velocity. For the simulation using this mesh, we used an element order=10 and $\eta = 0.0005$. Figure 3.9 shows the axial-velocity profiles obtained from the simulations at steady-state and the analytic solution. We observe that the velocity profile obtained from the simulations is similar to what we expect from the analytic solution.

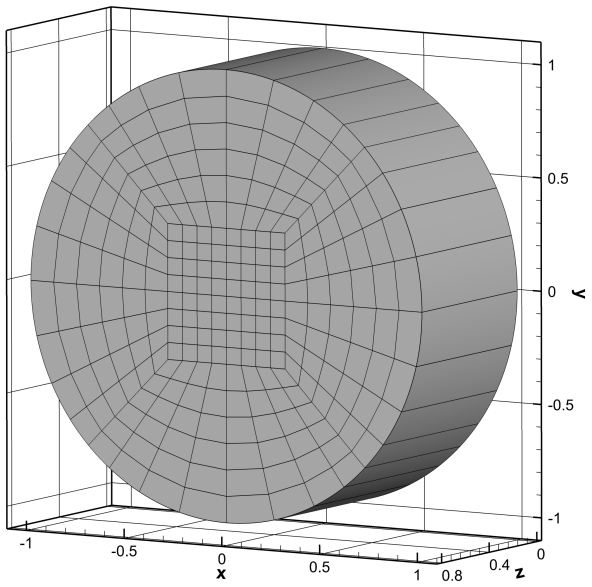

Figure 3.8.: Geometry and mesh of co-current pipe flow with 256 elements in each Fourier plane

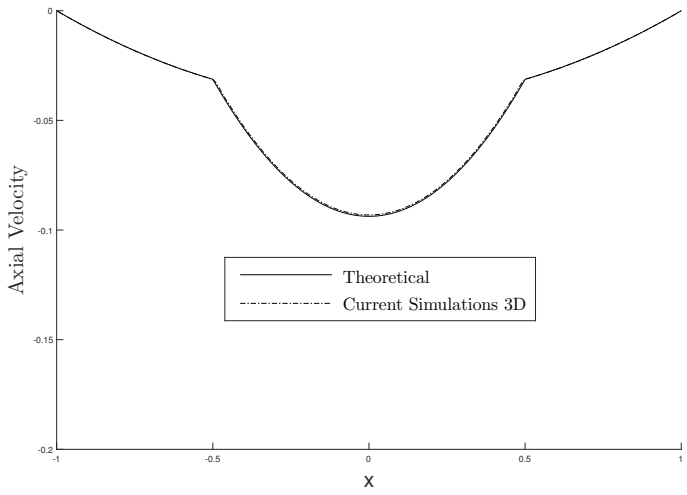

Figure 3.9.: Co-current Flow (256 elements in each Fourier plane): Comparison of the axial velocity profile between the simulation results and the theoretical profile.

Therefore, the method proposed in Section 3.3, can be used for accurately simulating steady-state two-phase flows.

3.4.3 Equilibrium Shape of a Liquid drop on a wall

In this subsection, we used the method proposed in section 3.3 to simulate the equilibrium shape of a liquid drop surrounded by a low density fluid on a horizontal partially wettable wall. We neglect the effect of the gravitational force for this test case. The goal of this test is to study the effects of the change in static contact angle on the equilibrium shape of the liquid drop. We will also demonstrate the accuracy of the method by measuring the spreading length and the height of the drop at equilibrium for different static contact angles and comparing them to the corresponding values obtained from the theory. For this problem, we choose the low-density fluid as the first fluid and the liquid drop as the second fluid.

We consider a non-dimensional flow domain given by $\Omega = [(x, y, z) : -0.5 \leq x \leq 0.5, 0 \leq y \leq 0.5, 0 \leq z \leq 0.8]$ as sketched in Figure 3.10. We choose the characteristic length scale as $L = 1 \times 10^{-2} m$, the characteristic density scale as $\rho_d = \rho_1$ (density of the first fluid) and set the characteristic velocity scale as $U_0 = \sqrt{g_0 L}$, where $g_0 = 1 m/s^2$. The non-dimensional density of the liquid is chosen as $\rho_2 = 5$. The initial shape of the liquid drop is set to be a hemisphere with a radius $R_0 = 0.25$ as shown in Figure 3.10. We denote the spreading length as L_s and the drop height as H. These parameters are illustrated in the Figure 3.10. Initially, the static contact angle is at 90^0 (hemisphere, Figure 3.10) and the drop is assumed to be at rest. When we begin the simulation, the shape of the drop initially changes because of the surface tension between the drop and the surrounding fluid as well as due to the contact angle set at the wall before it becomes a spherical cap at equilibrium (see Figure 3.11) [86]. Let R denote the radius of the spherical cap at equilibrium, and θ_e denote the static contact angle measured from the high-density liquid side (note that $\theta_e = 180^0 - \theta_s$). Then, based on the conservation of the volume of the liquid drop, we can obtain

the theoretical values of the spreading length and the drop height at equilibrium as follows [86]:

$$\frac{R}{R_0} = \sqrt[3]{\frac{2}{(2+cos\theta_e)(1-cos\theta_e)^2}},\ L_s = 2R\,sin\theta_e,\ H = R(1-cos\theta_e) \tag{3.55}$$

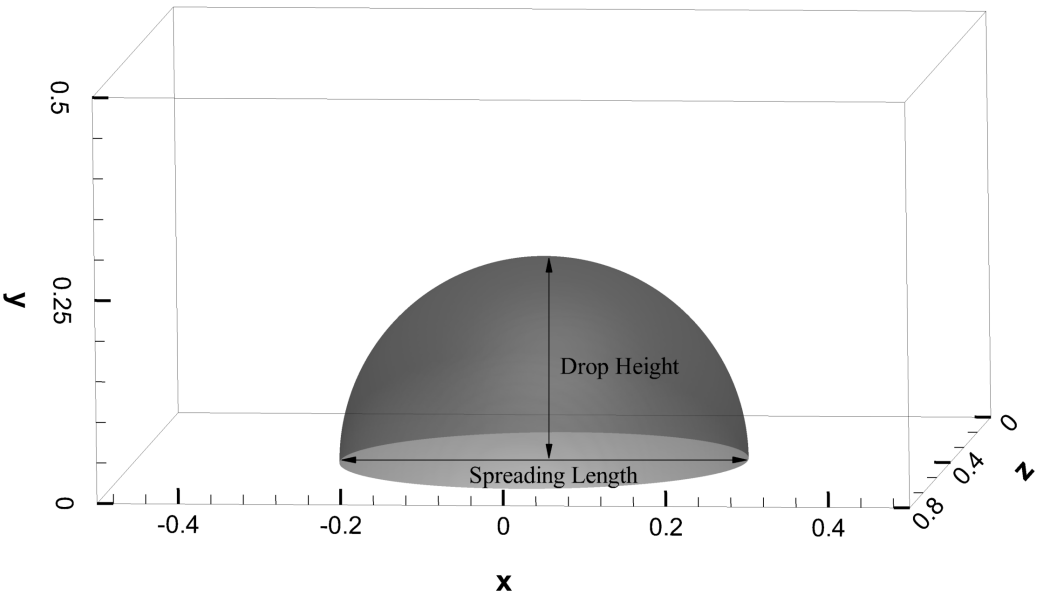

Figure 3.10.: Sketch showing the parameters of the the equilibrium shape of the liquid drop

We set periodic boundary conditions for all the flow variables at the left and right boundaries of the flow domain (the $y-z$ plane at $x=-0.5$ and $x=0.5$). The top and bottom boundaries (the $x-z$ plane at $y=0$ and $y=0.5$) are assumed to be solid walls where we use the no-slip conditions for the velocity and the static contact-angle boundary conditions for the phase field function. The flow domain Ω is discretized into 96 Fourier planes along the z-direction, and each plane is further discretized into

200 quadrilateral elements in the x-y plane. The simulations are then performed for five different static contact angles $\theta_e = 60^0, 75^0, 90^0, 105^0, 120^0$.

The following parameters have been used for performing the tests:

$$\begin{cases} \rho_1 = 1,\ \frac{\rho_2}{\rho_1} = 5,\ \mu_1 = 0.05\ \frac{\mu_2}{\mu_1} = 2; element\, order = 10, \\ \Delta t = 1 \times 10^{-5},\ C_\eta = 0.01,\ \lambda * \gamma_1 = 1.0\, e^{-8}, \\ \nu_m = 0.1, \sigma = 100 \end{cases}$$

Figure 3.11 shows the equilibrium shape of the liquid drop obtained for different contact angles $\theta_e = 60^0, 75^0, 90^0, 105^0, 120^0$. We can observe that as the contact angle θ_e increases, the spreading length of the drop decreases and the drop height increases. We observe that the equilibrium shapes at different contact angle are visually similar to the theoretical shape [86].

Before we make numerical comparisons between the simulations and the theory we briefly discuss the method used to obtain the spreading length and the drop height of the equilibrium shape of the drop from numerical simulations. Figure 3.12 shows the 2D projection of the 3D iso-surface $\phi = 0$ in the $x - y$ plane using Tecplot 360. We label the maximum and minimum y-coordinate of this iso-surface as Y_{max} and Y_{min} respectively (see Figure 3.12). We also label the minimum and the maximum value of the x-coordinate of this iso-surface at $y = Y_{min}$ as X_{min} and X_{max} respectively. We then calculate the spreading length and drop height from the numerical simulations as follows:

$$\begin{cases} Spreading\, Length(Simulation) = |X_{max} - X_{min}|, \\ Drop\, Height(Simulation) = |Y_{max} - Y_{min}| \end{cases}$$

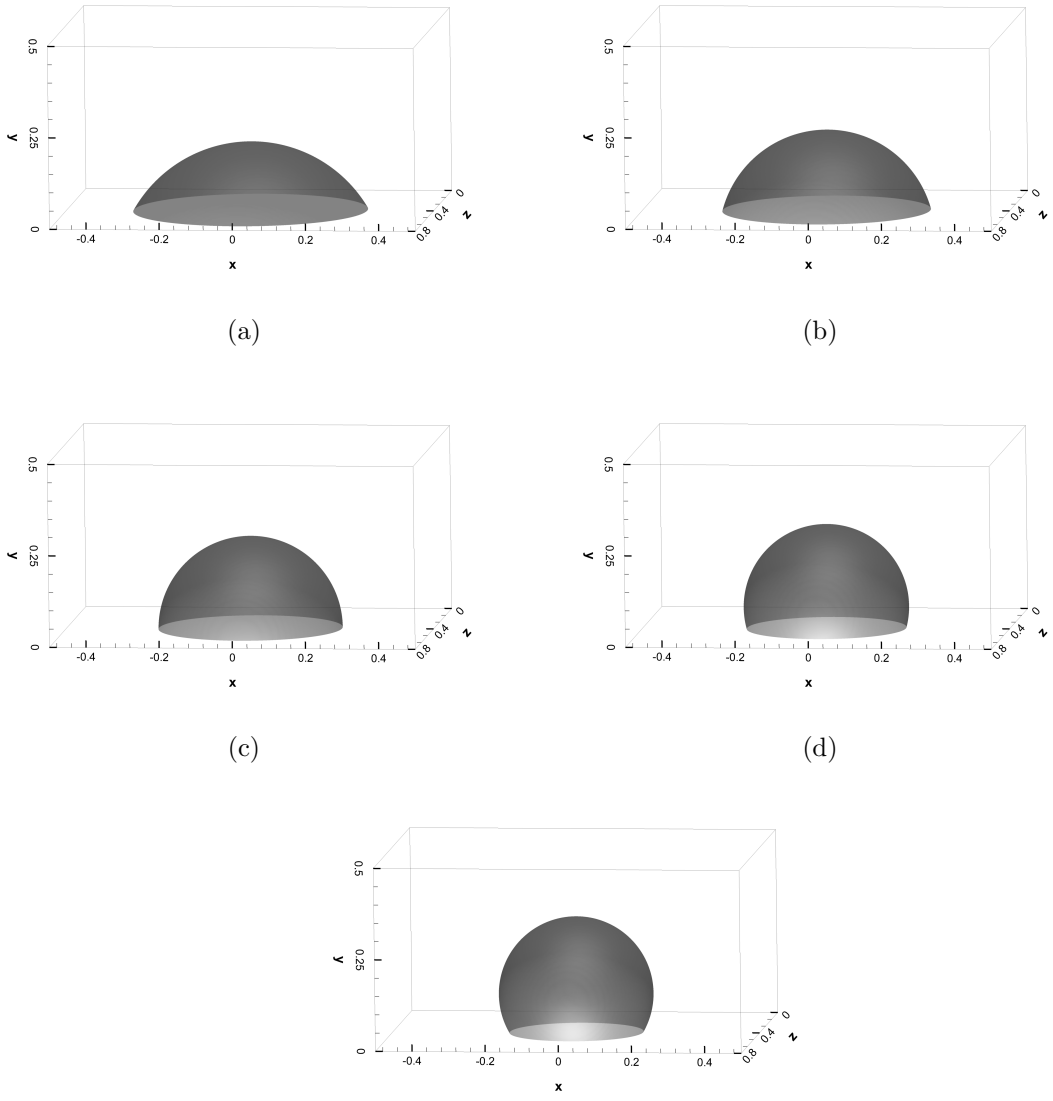

(a) (b)

(c) (d)

(e)

Figure 3.11.: Iso-surface $\phi = 0$ of the equilibrium shape of the liquid drop at (a) $\theta_e = 60^0$, (a) $\theta_e = 75^0$, (a) $\theta_e = 90^0$, (a) $\theta_e = 105^0$, (a) $\theta_e = 120^0$.

We can determine the contact angle actual using equations (3.55), once the spreading length and the drop height are calculated.

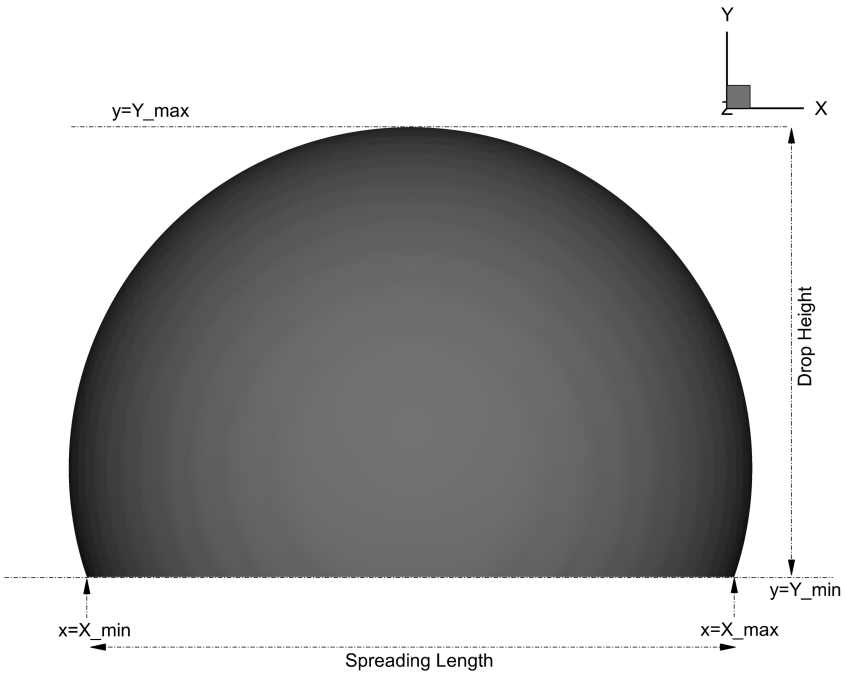

Figure 3.12.: Projection of the Isosurface $\phi = 0$ on the $x - y$ plane for θ_e=105^0

Figure 3.13 shows the comparison of the numerical values of the spreading length and the drop height between the theoretical results from equation (3.55) and the simulation results. We observe that the simulation results are almost identical to what we can predict from the theory.

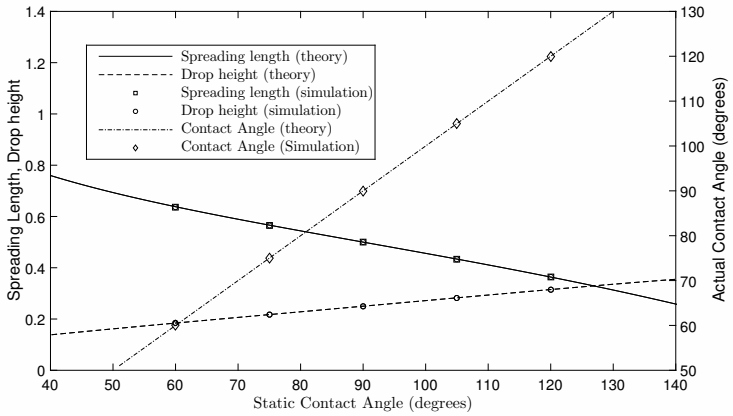

Figure 3.13.: Comparison of the drop height and spreading length (normalized by R_0) between simulation and theory as a function of static contact angle(θ_s). Comparison of the actual contact angle obtained from the simulations with the imposed static contact angle is also shown. The left vertical axis is for the spreading length and drop height, and the right vertical axis is for the contact angle(in degrees)

To study the effect of the element order on the spreading length and the drop height we performed simulations to obtain the equilibrium shape of the liquid drop with liquid side contact angle 105^0 for three different element orders=8, 10 and 12. We fixed the other parameters to that of the previous simulations in this subsection. Table 3.2 lists the results of the simulation for the different element orders and also the theoretical values. We observe that the numerical results are almost similar to the theoretical results and the higher element orders (10 and 12) giving slightly more accurate results for the spreading length when compared to the element order=8.

Overall, from the simulations in this subsection, we observe that the method proposed in Section 3.3 is capable of accurately imposing the static contact angle boundary conditions near the partially wettable wall.

Table 3.2.: Effect of Element Order on the spreading length and the drop height for liquid-side contact angle=105^0.

Element Order	Spreading Length	Drop Height
8	0.432	0.283
10	0.433	0.282
12	0.433	0.282
Theoretical	0.434	0.283

3.4.4 Flow dynamics of a Drop/Bubble in a Heavier Liquid

In this subsection, we use the proposed method to investigate two cases of a low-density liquid drop/bubble (first fluid) rising inside a container filled with a higher density liquid (second fluid). For the first case, we simulate a low-density liquid drop in a higher density liquid, and we choose the liquids such that the density and viscosity ratios between them are at moderate values. For the second case, we simulate an air-bubble in a domain filled with water, and we use the actual physical values for the density and viscosity of both air and water. Therefore, we are essentially simulating a two-phase flow with large density and viscosity ratios for the second case. The goal of performing these two cases is to study the dynamics of the two-phase system under the effect of surface tension and gravity using the method proposed in Section 3.3 and also to demonstrate the capabilities of the method for simulating realistic two-phase flows with large density and viscosity ratios. The effects of the static contact angle will also be investigated for the two cases. Also, we use the same flow domain for simulating the two-test cases.

We consider a non-dimensional flow domain, $\Omega = [(x, y, z) : -\frac{1}{2} \leq x \leq \frac{1}{2}, 0 \leq y \leq \frac{7}{5}, 0 \leq z \leq \frac{7}{5}]$. We set the characteristic length scale $L = 1 \times 10^{-2}m$, the characteristic density scale equal to the density of the first fluid $\rho_d = \rho_1$, and then set

the characteristic velocity scale as $U_0 = \sqrt{g_0 L}$, where $g_0 = 1m/s^2$ is used to normalize the gravitational force. Then we normalize all the physical variables and parameters by choosing appropriate normalization constants from Table 3.1. The low density liquid/bubble is assumed to be initially at rest and has a spherical shape with a non-dimensional radius $R_0 = \frac{1}{4}$ with its center located at $\mathbf{X}_0=(x_0, y_0, z_0)=(0, \frac{1}{2}, \frac{7}{10})$. We assume that the gravity is acting in the negative y direction. We impose periodic conditions at the left and right boundaries of the flow domain (i.e., in the $y-z$ plane at $x = -\frac{1}{2}$ and $x = \frac{1}{2}$) for all the flow variables. The top and bottom boundaries (i.e., the $x-z$ plane at $y = 0$ and $y = \frac{7}{5}$) are assumed to be solid walls and we impose the no-slip conditions for the velocity and the static contact-angle boundary conditions for the phase field function. The initial phase field distribution in the domain is set to:

$$\phi_{in}(\mathbf{x}) = -\tanh \frac{\sqrt{(x-x_0)^2 + (y-y_0)^2 + (z-z_0)^2} - R_0}{\sqrt{2}\eta}, \tag{3.56}$$

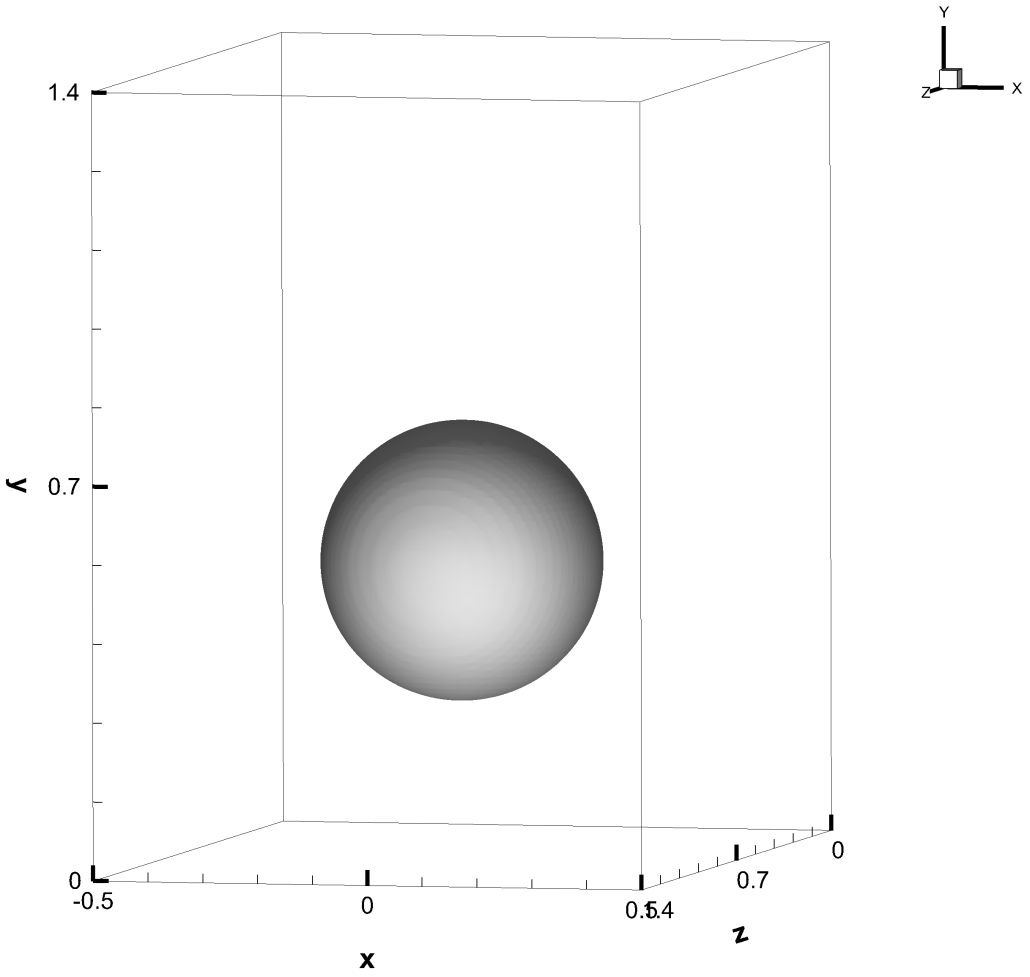

Figure 3.14.: Sketch showing the flow domain of the container.

Low-density liquid drop in a higher density liquid

In this test case, we study the motion of a low-density liquid drop in a higher density liquid. For this test case, we discretize the domain Ω into 64 Fourier planes in the z-direction, and each plane is further divided into 200 quadrilateral spectral elements in the $x-y$ plane. We perform simulations for several static contact angles θ_e=$60^0, 75^0, 90^0$ and 100^0 (where θ_e is the contact angle measured from the high-density liquid side) to study the dynamics of the two-phase system at the solid wall.

We have used the following non-dimensional parameters for performing these tests:

$$\begin{cases} \rho_1 = 1,\ \frac{\rho_2}{\rho_1} = 10,\ \mu_1 = 0.01,\ \frac{\mu_2}{\mu_1} = 3, \\ element\ order = 10,\ \Delta t = 2.5 \times 10^{-5},\ \eta = 0.008, \\ \lambda\gamma_1 = 1.0\, e^{-8},\ \nu_m = \frac{1}{2}\rho_1 \left(\frac{\mu_1}{\rho_1} + \frac{\mu_2}{\rho_2}\right),\ \sigma = 100. \end{cases}$$

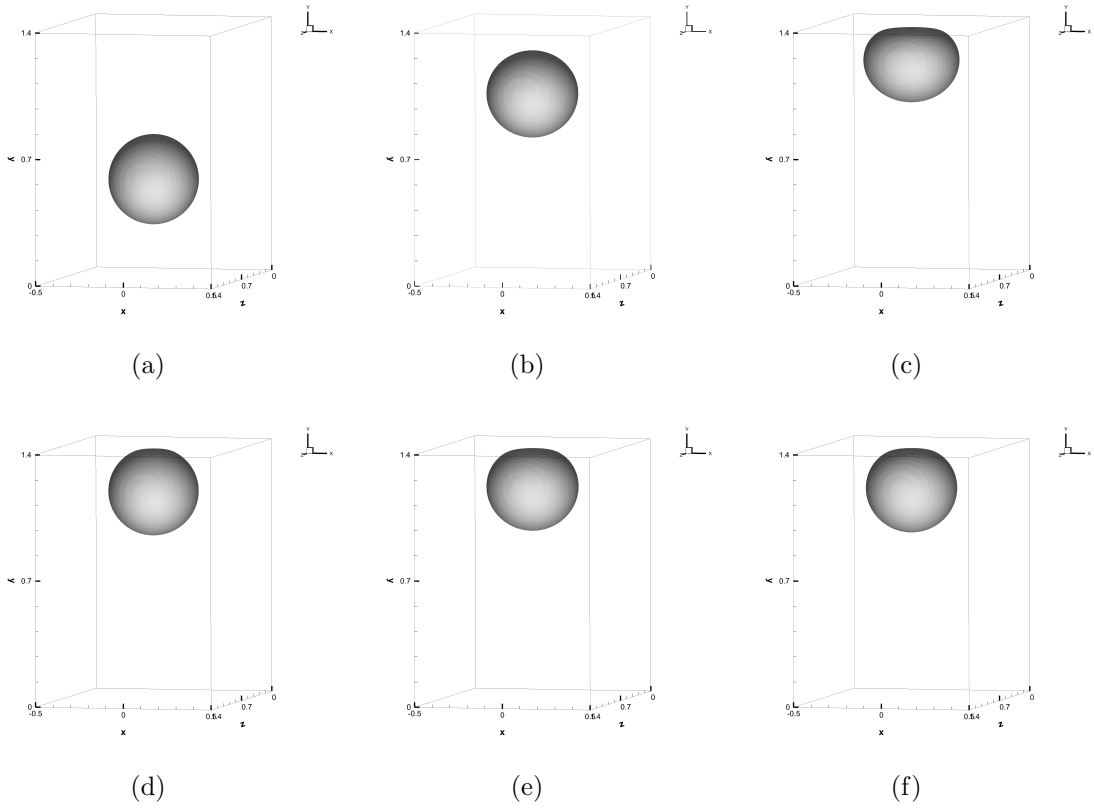

(a) (b) (c)

(d) (e) (f)

Figure 3.15.: Temporal sequence of snapshots of the fluid-fluid interface with $\theta_e = 60^0$: (a) t=0.11 (b) t=0.48 (c) t=0.57 (d) t=0.77 (e) t=0.97 (f) t=1.17.

Figures 3.15,3.16,3.17 and 3.18 show the temporal sequence of the snapshots of the fluid-fluid interface for the θ_e= $60^0, 75^0, 90^0$ and 105^0 respectively. From Figure 3.15(a)-(b) we observe that because of the buoyancy the low-density liquid drop which is initially at rest starts to rise in the flow domain. As the velocity of the liquid drop increases, it starts to deform (see Figure 3.15(a)-(c)). For $\theta_e = 60$, we see that the

drop does not reach the top wall as it could not displace the high-density fluid located near the wall. The liquid drop then slightly oscillates before coming to steady state slightly below the top wall. The dynamics of the drop is observed to be similar for different contact angles when the drop is away from the top wall. However, in the vicinity of the top wall, we observe that for contact angles $\theta_e = 75^0, 90^0, 100^0$ (see Figures 3.16-3.18), the drop is able to displace the higher density liquid at the top wall unlike the case with $\theta_e = 60^0$ (Figure 3.15).

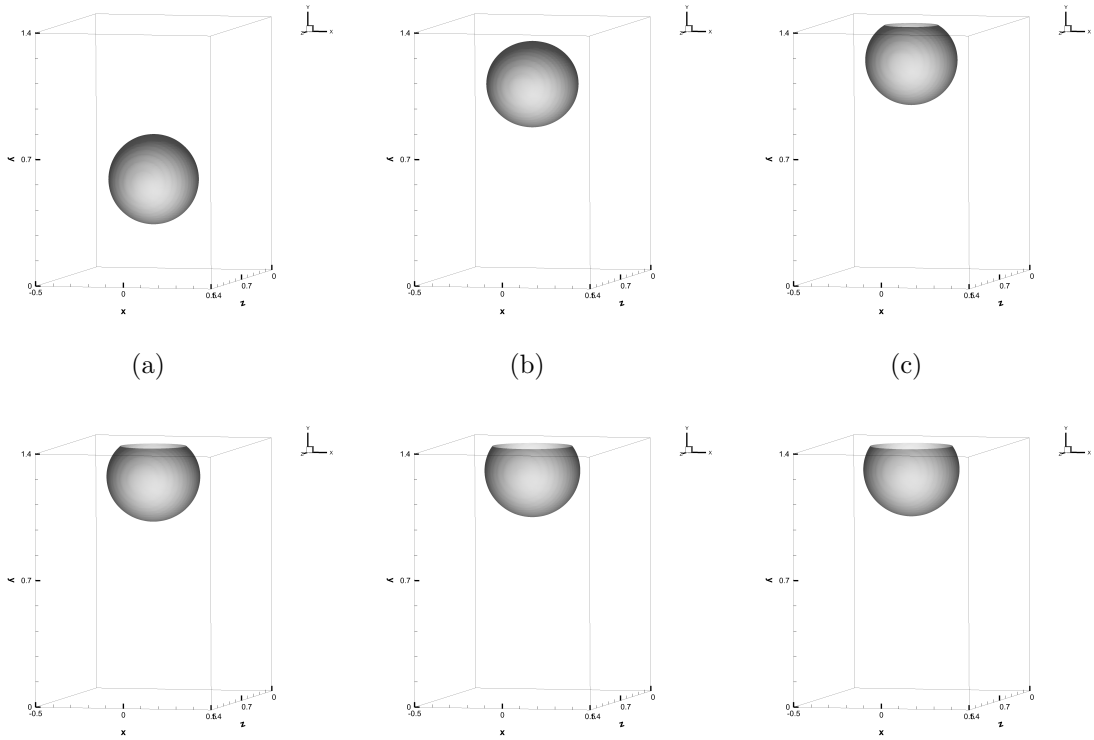

(a) (b) (c)

(d) (e) (f)

Figure 3.16.: Temporal sequence of snapshots of the fluid-fluid interface with $\theta_e = 75^0$: (a) t=0.11 (b) t=0.52 (c) t=0.87 (e) t=0.97 (f) t=1.42 (i) t=2.12.

For the case $\theta_e = 75^0$, we can see that the liquid drop displaces the higher density liquid near the top wall and touches the wall. Then it slowly starts deforming due to the contact angle condition, before it eventually reaches a steady state. However, for

the cases $\theta_e = 90^0$ and $\theta_e = 100^0$, we see that a small portion of the higher density liquid gets trapped inside the lower density drop and the fluid-fluid interface separates into two interfaces (see Figures 3.17(c) and 3.18(d)) with the external interface deforming significantly in the y direction. The external interface then begins to slowly recover its shape in the y-direction, whereas the internal interface slowly develops in the -y direction before the two interfaces finally come to steady state (see Figures 3.17(d)-(f) and 3.18(e)-(i)).

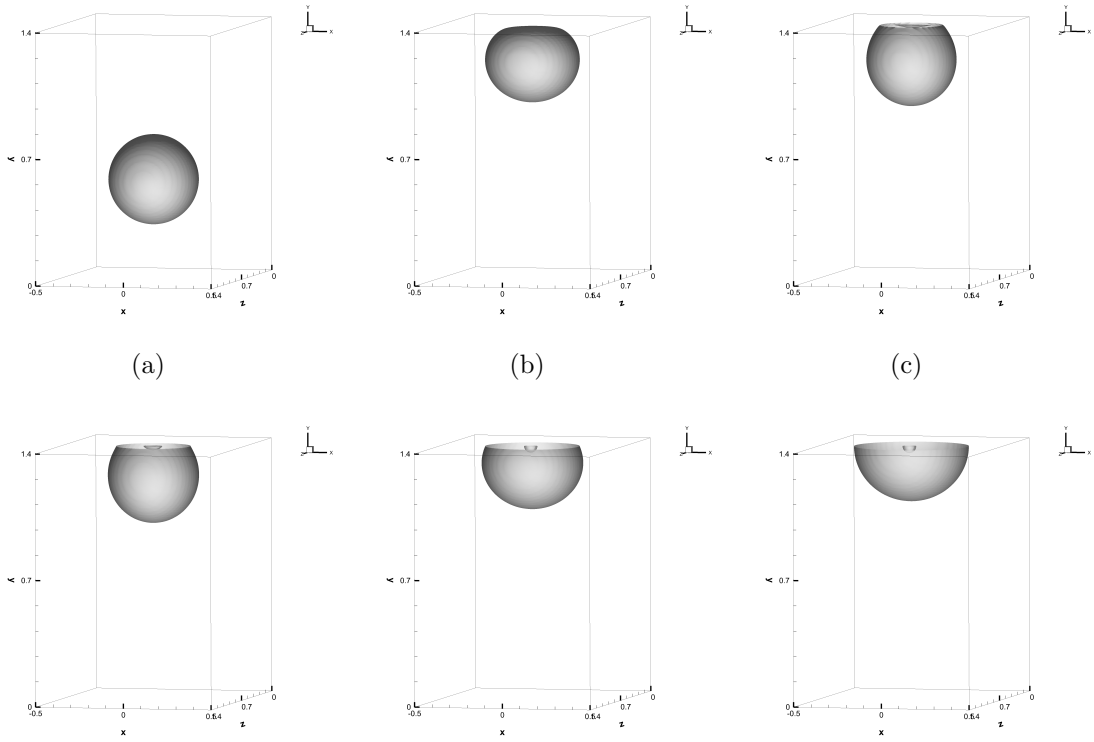

Figure 3.17.: Temporal sequence of snapshots of the fluid-fluid interface with $\theta_e = 90^0$: (a) t=0.11 (b) t=0.67 (c) t=0.73 (d) t=0.77 (e) t=0.87 (f) t=1.43 (g) t=0.70 (h) t=0.85 (i) t=1.95.

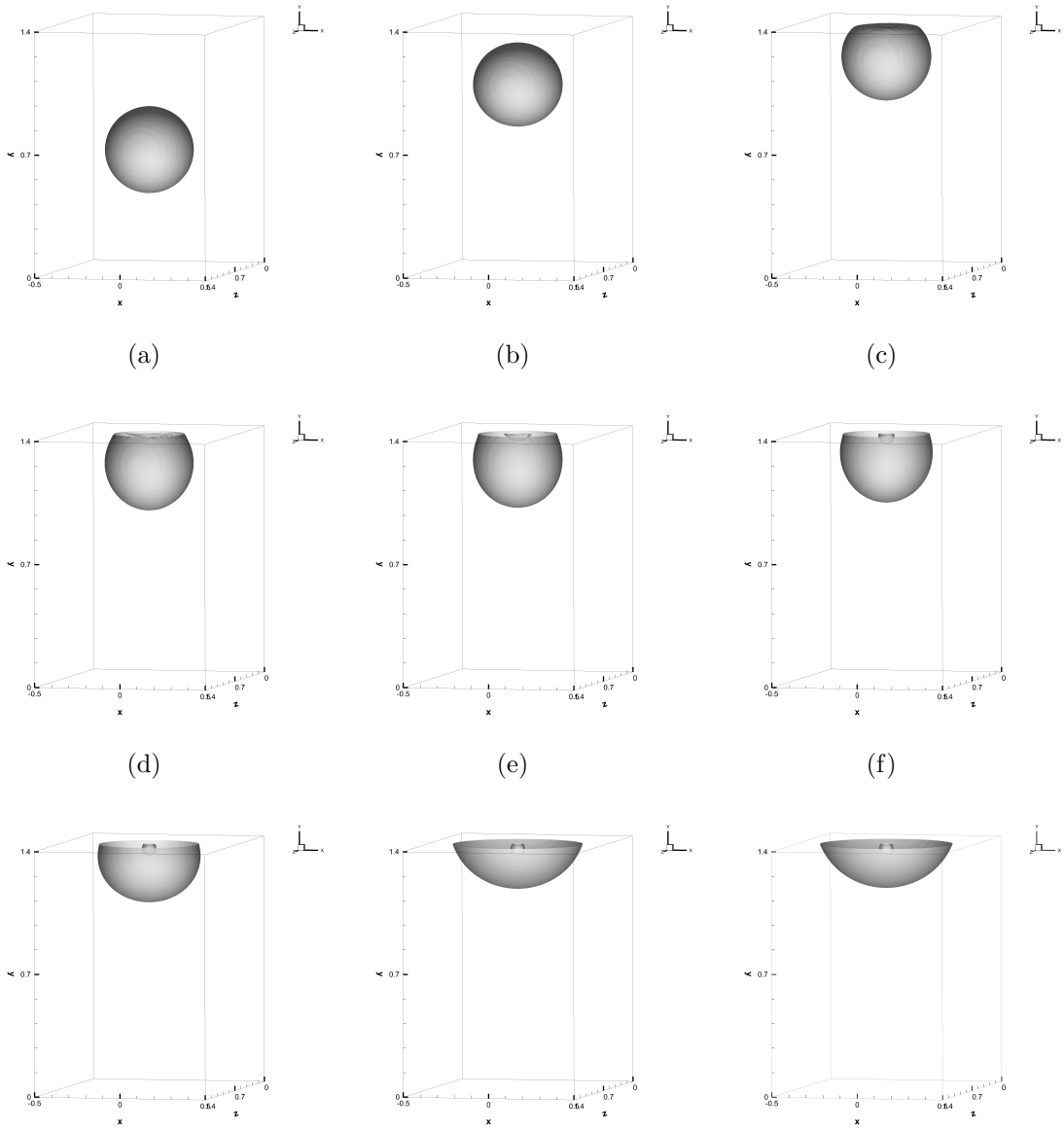

(a) (b) (c)

(d) (e) (f)

(g) (h) (i)

Figure 3.18.: Temporal sequence of snapshots of the fluid-fluid interface with $\theta_e = 100^0$: (a) t=0.26 (b) t=0.51 (c) t=0.69 (d) t=0.71 (e) t=0.73 (f) t=0.76 (g) t=0.81 (h) t=1.01 (i) t=1.31.

From these simulations, we observed that the static contact angle has a significant effect on the dynamics of the two-phase system, and the proposed method is capable of capturing its effect.

Air-bubble in Water

In this test case, we simulate the motion of an air-bubble inside a domain filled with water. We assume the true physical values for all the physical parameters such as the air/water density, viscosity, surface tension involved in this problem. Specifically,

$$\begin{cases} air: & \rho_{air} = 1.2041\, kg/m^3,\ \mu_{air} = 1.78\ \times\ 10^{-5}\, kg/(m\, s), \\ water: & \rho_{water} = 998.207\, kg/m^3,\ \mu_{water} = 1.002\ \times\ 10^{-3}\, kg/(m\, s), \\ surface\ tension: \sigma = 7.28\ \times 10^{-2}\, kg/s^2,\ gravity = 9.8\ m/s^2. \end{cases}$$

For this test case, the flow domain Ω is discretized into 96 Fourier planes along the z-direction, and each plane is divided into 200 quadrilateral spectral elements in the $x-y$ plane. We perform simulations for several static contact angles θ_e=$60^0, 75^0, 90^0$ and 105^0, (where θ_e is the water-side contact angle) to study the different interactions of the air-bubble with the solid wall at the top of the domain.

We have used the following non-dimensional parameters for performing these tests:

$$\begin{cases} \rho_1 = 1,\ \frac{\rho_2}{\rho_1} = 829,\ \mu_1 = 0.0147828,\ \frac{\mu_2}{\mu_1} = 56.29, \\ element\ order = 12,\ \Delta t = 2.5 \times 10^{-5},\ \eta = 0.02, \\ \lambda\gamma_1 = 1.0 \times 10^{-6},\ \nu_m = 0.0147828,\ \sigma = 604.601. \end{cases}$$

Figures 3.19, 3.20, 3.21, and 3.22 show the temporal sequence of the air-water interface for the water-side contact angles $60^0, 75^0, 90^0$ and 105^0 respectively. From Figure 3.19(a)-(b) we observe that because of the buoyancy the air bubble which is initially at rest begins to gain momentum and starts to rise in the flow domain. As the air bubble builds enough momentum, it begins to slowly start deforming and continues to deform just before reaching the top wall as can be seen from Figure 3.19(c)-(d). Note that the dynamics of the air-water interface is same for all the different contact angles just before the interface touches the solid wall at the top boundary(see Figures 3.19(a)-(d),3.20(a)-(d), 3.21 (a)-(d) and 3.22(a)-(d)). This observation is similar to what we have observed in the test case with low-density ratios. However, for this

case, we observe that the air-bubble displaces the water near the top wall even when $\theta_e = 60^0$. The large density ratios between air and water cause the bubble to have more velocity and thus more kinetic energy which is sufficient enough to displace the water.

We observe different interactions for different static contact angles after the interface touches the solid wall. Let us first consider the case with the 60^0 water-side contact angle. From Figure 3.19(e)-(f) we can observe that the air-water interface has been distorted severely. Also, the air-bubble has trapped a small water drop inside it causing the air-water interface to split into two parts. The external interface slowly regains its shape along the vertical direction while the inner interface is still attached to the wall and quickly reshapes to satisfy the static contact angle boundary conditions at the top wall (see Figure 3.19(g)-(h)). The water drop is not able to leave the air-bubble because the surface tension, in this case, is strong enough to counter the gravitational force acting on the water drop. The equilibrium shape of the two air-water interfaces resembles that of a spherical cap and can be seen in Figure 3.19(i).

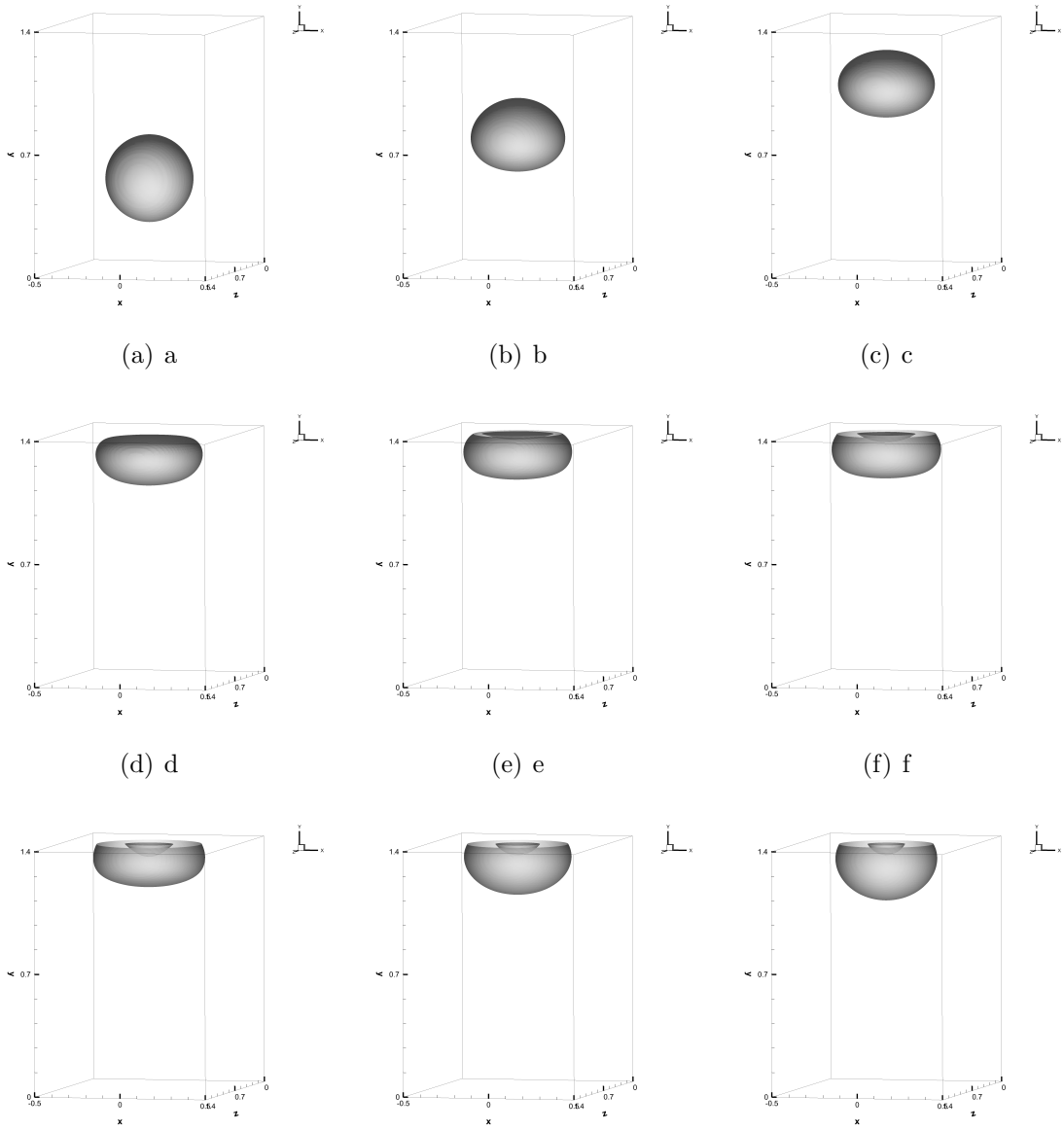

(a) a (b) b (c) c

(d) d (e) e (f) f

(g) g (h) h (i) i

Figure 3.19.: Temporal sequence of snapshots of the air-water interface with $\theta_e = 60^0$: (a) t=0.06, (b) t=0.26, (c) t=0.44, (d) t=0.60, (e) t=0.65, (f) t=0.67, (g) t=0.70, (h) t=0.85, (i) t=1.95.

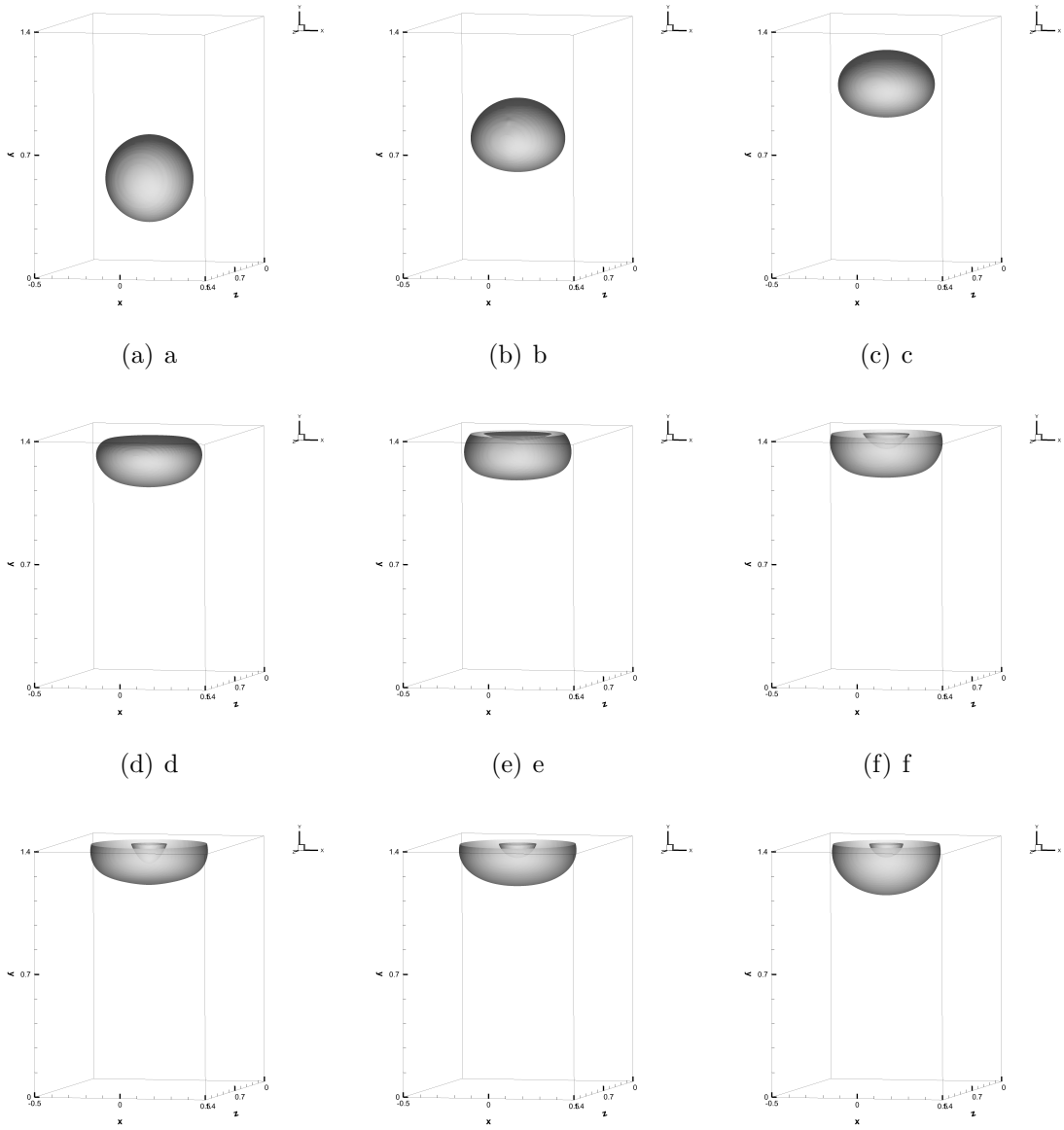

(a) a (b) b (c) c

(d) d (e) e (f) f

(g) g (h) h (i) i

Figure 3.20.: Temporal sequence of snapshots of the air-water interface with $\theta_e = 75^0$: (a) t=0.06, (b) t=0.26, (c) t=0.44, (d) t=0.59, (e) t=0.64, (f) t=0.67, (g) t=0.70, (h) t=0.84, (i) t=1.78.

The air-water interface with 75^0 water-side contact angle shows the similar behavior as the 60^0 contact angle with an exception that the water drop trapped inside yearns to separate from the top wall but fails to do so as can be seen in Figure 3.20(g)-(i). For the 90^0 contact angle some portion of trapped water drop does escape the air bubble (see Figure 3.21(h)-(j)) but fails to do so entirely(see Figure 3.21(k)). The reason for this might be because the surface tension was not enough to carry the massive water drop, but once some of the water escaped the bubble, it was sufficient enough to hold the lighter drop. Throughout the process, the exterior air-water interface remains deformed in the vertical direction only to regain its spherical cap shape after the inside interface stabilizes. For the air-water interface with 105^0 static contact angle, the trapped water drop completely escapes the air-bubble into the flow domain with water, and there is once more only a single air-water interface (see Figure3.22(f)-(k)). An important observation to be noted is that in Figure 3.22(g) when the water drop is escaping the air-bubble, it first separates from the top wall and then leaves the bubble. Failing to first separate from the top wall would result in the separation of the air-bubble into two smaller bubbles as observed in the 2D simulations in the previous works [53]. Overall, we can see that the tendency of the trapped water drop to free itself increases with the increase in water-side contact angle.

From the above simulations, we can be sure that the method proposed herein is capable of effectively simulating air-water interfaces and their complicated interactions such as the interface deformations and capturing specific flow dynamics such as the trapping of the water-drop inside the air-bubble.

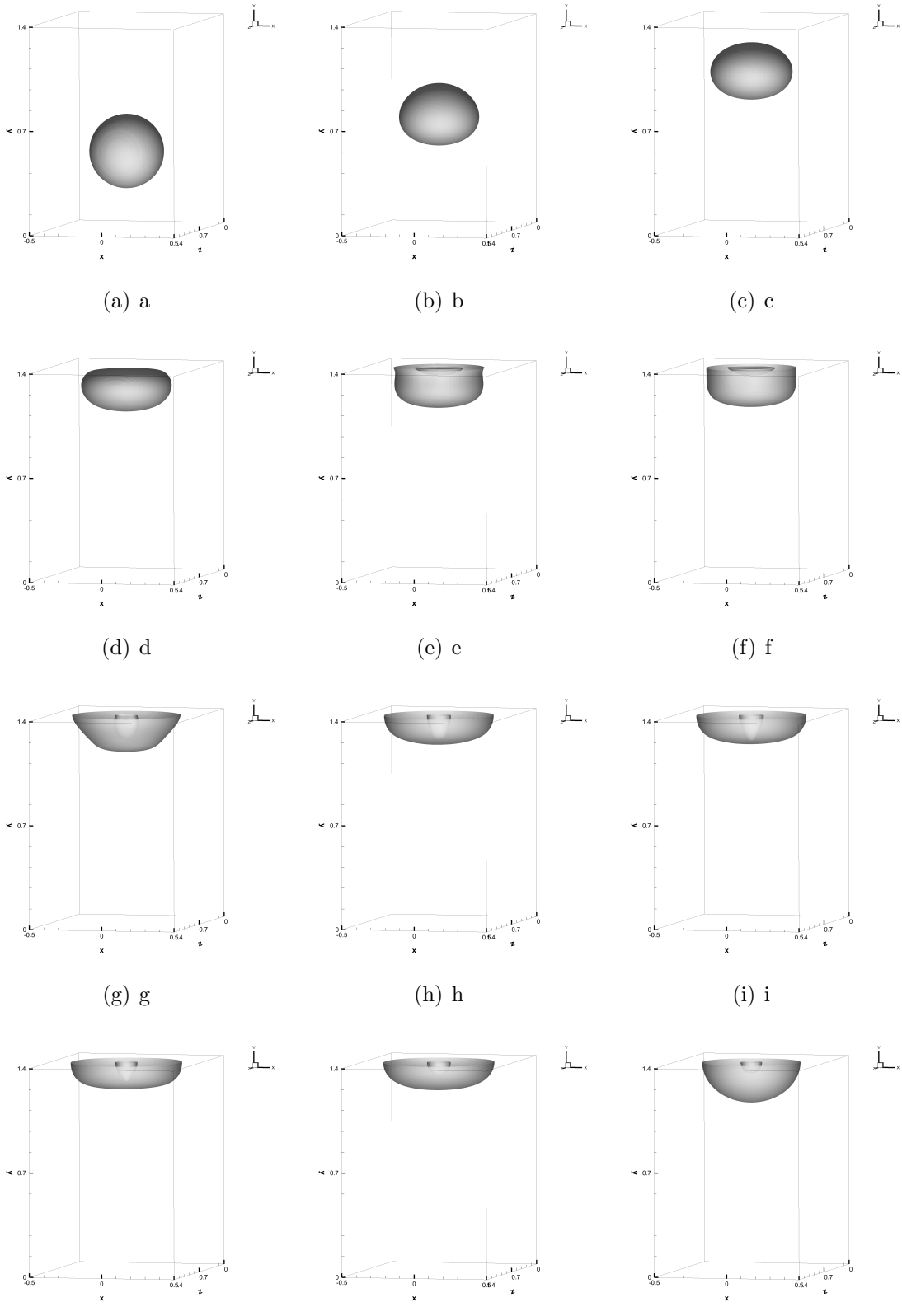

(a) a (b) b (c) c

(d) d (e) e (f) f

(g) g (h) h (i) i

(j) g (k) h (l) i

Figure 3.21.: Temporal sequence of snapshots of the air-water interface with $\theta_e = 90^0$: (a) t=0.06, (b) t=0.26, (c) t=0.44, (d) t=0.60, (e) t=0.63, (f) t=0.64, (g) t=0.66, (h) t=0.73, (i) t=0.74, (j) t=0.78, (k) t=0.85, (l) t=1.45.

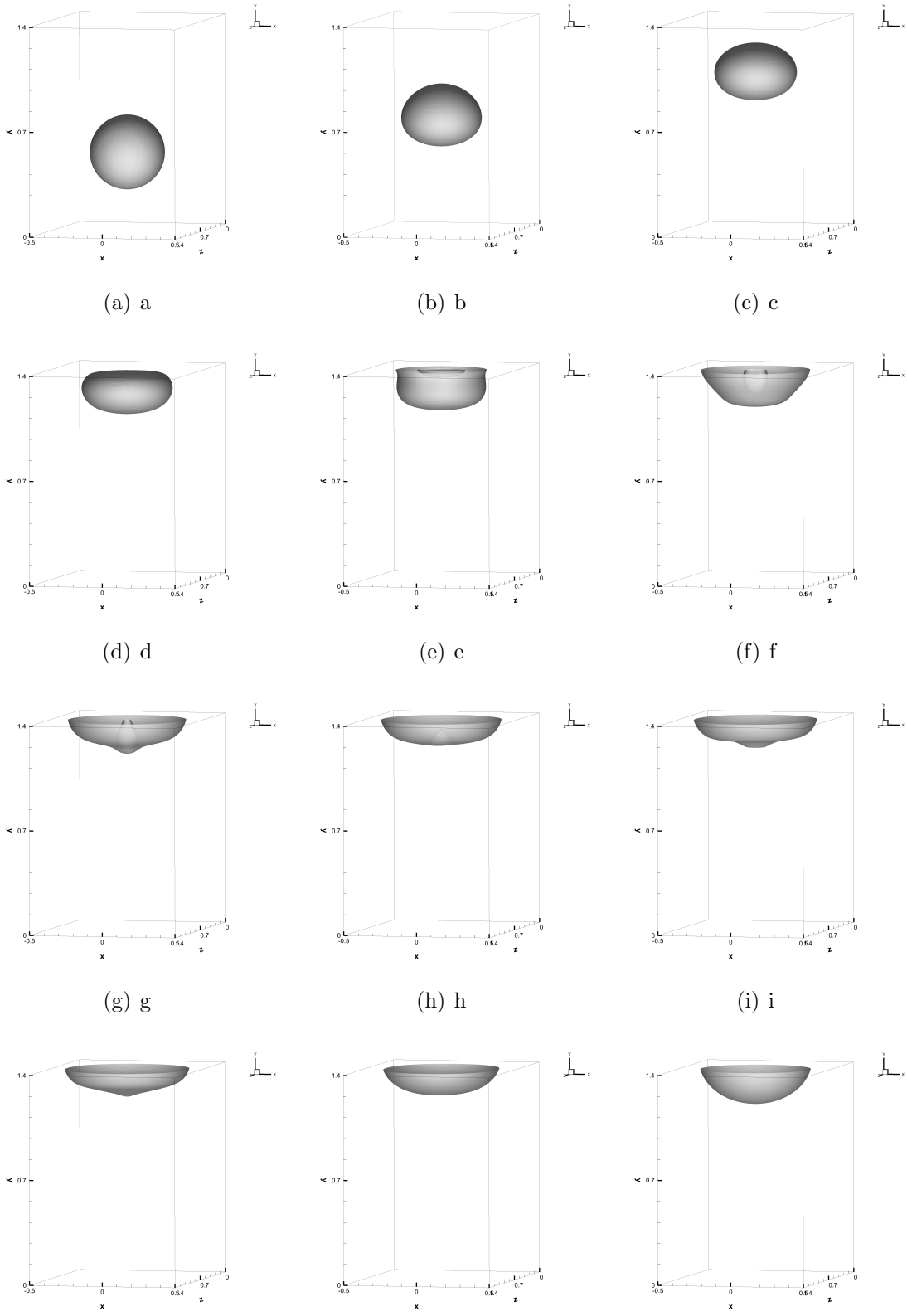

(a) a (b) b (c) c

(d) d (e) e (f) f

(g) g (h) h (i) i

(j) g (k) h (l) i

Figure 3.22.: Temporal sequence of snapshots of the air-water interface with $\theta_e = 105^0$: (a) t=0.06, (b) t=0.26, (c) t=0.44, (d) t=0.60, (e) t=0.63, (f) t=0.66, (g) t=0.70, (h) t=0.72, (i) t=0.75, (j) t=0.77, (k) t=0.90, (l) t=1.45.

4. CONCLUSIONS AND RECOMMENDATIONS

This thesis consists of two parts which focus on developing numerical algorithms for the simulations of incompressible single-phase and two-phase flows. In the first part of this thesis, we presented a modified consistent splitting scheme for incompressible single-phase flows in an unbounded domain together with a recently developed energy stable outflow boundary condition [3] in Chapter 2. This numerical scheme is capable of simulating incompressible single-phase flows in an open boundary at high Reynolds numbers, unlike a standard consistent splitting scheme, which is observed to be unstable at these Reynolds numbers. The essential feature that enables stable simulations at high Reynolds numbers lies in the reformulation of the viscous term. We employ C^0- continuous high order spectral-elements for the spatial discretization of the proposed algorithm in Section 2.3. Then we perform several numerical simulations to test the performance of the proposed method in Section 2.4. Based on the numerical convergence tests, we demonstrate that the proposed method has a spatial exponential convergence rate and a temporal second-order convergence rate for all the flow variables. To demonstrate the accuracy of the method, we have also compared the results of the numerical simulations with experimental values and other numerical simulation results from the literature for a flow past a circular cylinder in the two-dimensional flow regime. We have also conducted long-time simulations at high Reynolds numbers for two problems. These simulations show that the modified consistent-splitting scheme together with the open boundary condition presented in [3] can effectively overcome the backflow instabilities in the presence of strong vortices at the outflow boundary.

In Chapter 3 of this thesis, we presented a hybrid spectral element-Fourier spectral method for the spatial discretization of a recently developed numerical algorithm [53] for simulating wall bounded two-phase flows with static contact angle boundary con-

ditions in a three-dimensional domain which is homogeneous in at least one direction. All the flow variables are represented by Fourier spectral expansions in the homogeneous direction and by C^0 spectral element expansions in the non-homogeneous directions. The essential aspects of the spatial discretization technique proposed in Section 3.3 are: (1) It completely decouples the computations of the flow variables using Fourier spectral expansions in the homogeneous direction, (2) The algorithm to compute the flow variables consists of solving linear algebraic systems of two dimensional decoupled equations about the Fourier modes, which can be solved largely in parallel, (3) The coefficient matrices of these linear algebraic systems of equations are constant and can, therefore, be precomputed. We have conducted several simulations to demonstrate the performance of the proposed spatial discretization technique. The convergence tests show that the overall algorithm presented in Section 3.3 has a second-order convergence rate in time and an exponential spatial convergence rate for all the flow variables. To demonstrate the accuracy of the proposed method, we have considered a co-current two-phase flow system which has a physical solution and compared the numerical results with the theoretical results. To demonstrate the effectiveness of the proposed method in imposing static contact angles, we investigated the equilibrium shape of a liquid drop on a partially wettable wall without any external forces for various static contact angles and compared the numerical results (such as the spreading length of the drop) with the theoretical predictions. We have performed simulations of an air bubble trapped inside water with true values for the physical properties for various static contact angles to demonstrate the capability of the proposed method to simulate realistic flows and capture different complex interactions.

Future research can extend this spatial discretization technique for the two-phase flows with dynamic contact angle boundary conditions or even for solving a system of multi-phase flows. Further, we desire to use the method proposed in section 2.2 to simulate three-dimensional single-phase flows and study the performance of the method.

REFERENCES

[1] S. Dong and J. Shen. An unconditionally stable rotational velocity-correction scheme for incompressible flows. *Journal of Computational Physics*, 229(19):7013–7029, 2010.

[2] S. Dong and J. Shen. A pressure correction scheme for generalized form of energy-stable open boundary conditions for incompressible flows. *Journal of Computational Physics*, 291:254–278, June 2015.

[3] S. Dong. A convective-like energy-stable open boundary condition for simulations of incompressible flows. *Journal of Computational Physics*, 302(C):300–328, December 2015.

[4] R. L. Sani and P. M. Gresho. Rsum and remarks on the open boundary condition minisymposium. *International Journal for Numerical Methods in Fluids*, 18(10):983–1008, 1994.

[5] T. C. Papanastasiou, N. Malamataris, and K. Ellwood. A new outflow boundary condition. *International Journal for Numerical Methods in Fluids*, 14(5):587–608, 1992.

[6] Alexandre Joel Chorin. Numerical solution of the Navier-Stokes equations. *Mathematics of Computation*, 22(104):745–762, 1968.

[7] R. Tmam. Sur l'approximation de la solution des quations de Navier-Stokes par la mthode des pas fractionnaires (ii). *Archive for Rational Mechanics and Analysis*, 33(5):377–385, 1969.

[8] Jie Shen. On error estimates of the projection methods for the Navier-Stokes equations: Second-order schemes. *Mathematics of Computation of the American Mathematical Society*, 65(215):1039–1065, 1996.

[9] David L. Brown, Ricardo Cortez, and Michael L. Minion. Accurate projection methods for the incompressible navierstokes equations. *Journal of Computational Physics*, 168(2):464–499, 2001.

[10] J Kim and P Moin. Application of a fractional-step method to incompressible Navier-Stokes equations. *Journal of Computational Physics*, 59(2):308–323, 1985.

[11] J. L. Guermond and Jie Shen. On the error estimates for the rotational pressure-correction projection methods. *Mathematics of Computation*, 73(248):1719–1737, 2004.

[12] L. J. P. Timmermans, P. D. Minev, and F. N. Van De Vosse. An approximate projection scheme for incompressible flow using spectral elements. *International Journal for Numerical Methods in Fluids*, 22(7):673–688, April 1996.

[13] Lorenzo Botti. A pressure-correction scheme for convection-dominated incompressible flows with discontinuous velocity and continuous pressure. 230(3):572–586, February 2011.

[14] George Em Karniadakis, Moshe Israeli, and Steven A Orszag. High-order splitting methods for the incompressible Navier-Stokes equations. *Journal of Computational Physics*, 97(2):414–443, 1991.

[15] J.L. Guermond and Jie Shen. A new class of truly consistent splitting schemes for incompressible flows. *Journal of Computational Physics*, 192(1):262–276, 2003.

[16] Qingfang Liu, Yanren Hou, Zhiheng Wang, and Jiakun Zhao. A two-level consistent splitting scheme for the Navier-Stokes equations. *Computers and Fluids*, 140:167–174, November 2016.

[17] J.L. Guermond, P. Minev, and Jie Shen. An overview of projection methods for incompressible flows. *Computer Methods in Applied Mechanics and Engineering*, 195(44):6011–6045, 2006.

[18] J. L. Guermond, P. Minev, and J. Shen. Error analysis of pressure-correction schemes for the time-dependent Stokes equations with open boundary conditions. *SIAM Journal on Numerical Analysis*, 43(1):239–258, 2005.

[19] John C. Strikwerda and Young S. Lee. The accuracy of the fractional step method. *SIAM Journal on Numerical Analysis*, 37(1):37–47, 1999.

[20] J.P. Pontaza. A new consistent splitting scheme for incompressible Navier-Stokes flows: A least-squares spectral element implementation. *Journal of Computational Physics*, 225(2):1590–1603, August 2007.

[21] John Craske and Maarten van Reeuwijk. Robust and accurate open boundary conditions for incompressible turbulent jets and plumes. *Computers and Fluids*, 86:284–297, November 2013.

[22] M.Y. Forestier, R. Pasquetti, R. Peyret, and C. Sabbah. Spatial development of wakes using a spectral multi-domain method. *Applied Numerical Mathematics*, 33(1):207–216, 2000.

[23] P M Gresho. Incompressible fluid dynamics: Some fundamental formulation issues. *Annual Review of Fluid Mechanics*, 23(1):413–453, January 1991.

[24] Jayant Keskar and D. A. Lyn. Computations of a laminar backward-facing step flow at re =800 with a spectral domain decomposition method. *International Journal for Numerical Methods in Fluids*, 29(4):411–427, February 1999.

[25] M. A. Ol' Shanskii and V. M. Staroverov. On simulation of outflow boundary conditions in finite difference calculations for incompressible fluid. *International Journal for Numerical Methods in Fluids*, 33(4):499–534, June 2000.

[26] M. Behr, J. Liou, R. Shih, and T. E. Tezduyar. Vorticitystreamfunction formulation of unsteady incompressible flow past a cylinder: Sensitivity of the computed flow field to the location of the outflow boundary. 12(4):323–342, February 1991.

[27] Michael S. Engelman and MohammadAli Jamnia. Transient flow past a circular cylinder: A benchmark solution. *International Journal for Numerical Methods in Fluids*, 11(7):985–1000, November 1990.

[28] David K. Gartling. A test problem for outflow boundary conditionsflow over a backwardfacing step. *International Journal for Numerical Methods in Fluids*, 11(7):953–967, November 1990.

[29] John M. Leone. Open boundary condition symposium benchmark solution: Stratified flow over a backward-facing step. *International Journal for Numerical Methods in Fluids*, 11(7):969–984, November 1990.

[30] Jie Liu. Open and traction boundary conditions for the incompressible Navier-Stokes equations. *Journal of Computational Physics*, 228(19):7250–7267, 2009.

[31] C Taylor, J Rance, and J Medwell. A note on the imposition of traction boundary conditions when using the FEM for solving incompressible flow problems. *Communications in Applied Numerical Methods*, 1:113–121, May 1985.

[32] S. Dong and G.E. Karniadakis. Dns of flow past a stationary and oscillating cylinder at re = 10 000. *Journal of Fluids and Structures*, 20(4):519–531, 2005.

[33] S. Dong, G. E. Karniadakis, A. Ekmekci, and D. Rockwell. A combined direct numerical simulation particle image velocimetry study of the turbulent near wake. *Journal of Fluid Mechanics*, 569:185–207, December 2006.

[34] Charles-Henri Bruneau and P Fabrie. Effective downstream boundary conditions for incompressible Navier-Stokes equations. 19:693 – 705, 10 1994.

[35] Volker Gravemeier, Andrew Comerford, Lena Yoshihara, Mahmoud Ismail, and Wolfgang A. Wall. A novel formulation for Neumann inflow boundary conditions in biomechanics. *International Journal for Numerical Methods in Biomedical Engineering*, 28(5):560–573, 2012.

[36] Cristbal Bertoglio, Alfonso Caiazzo, Yuri Bazilevs, Malte Braack, Mahdi Esmaily, Volker Gravemeier, Alison L. marsden, Olivier Pironneau, Irene E. vignon-Clementel, and Wolfgang A. wall. Benchmark problems for numerical treatment of backflow at open boundaries. *International Journal for Numerical Methods in Biomedical Engineering*, 34(2):n/a–n/a, 2018.

[37] Mahdi Esmaily Moghadam, Yuri Bazilevs, Tain-Yen Hsia, Irene Vignon-Clementel, and Alison Marsden. A comparison of outlet boundary treatments for prevention of backflow divergence with relevance to blood flow simulations. *Computational Mechanics*, 48(3):277–291, 2011.

[38] David Jacqmin. Contact-line dynamics of a diffuse fluid interface. *Journal of Fluid Mechanics*, 402:57–88, 2000.

[39] Hang Ding and Peter D. M Spelt. Inertial effects in droplet spreading: a comparison between diffuse-interface and level-set simulations. *Journal of Fluid Mechanics*, 576:287–296, 2007.

[40] Elizabeth B. Dussan V. and Stephen H. Davis. On the motion of a fluid-fluid interface along a solid surface. *Journal of Fluid Mechanics*, 65(1):71–95, 1974.

[41] Ruben Scardovelli and Stphane Zaleski. Direct numerical simulation of free-surface and interfacial flow. *Annual Review of Fluid Mechanics*, 31(1):567–603, January 1999.

[42] C.W Hirt and B.D Nichols. Volume of fluid (VOF) method for the dynamics of free boundaries. *Journal of Computational Physics*, 39(1):201–225, 1981.

[43] James M. Hyman. Numerical methods for tracking interfaces. *Physica D: Nonlinear Phenomena*, 12(1):396–407, 1984.

[44] James Albert Sethian. *Level set methods : evolving interfaces in geometry, fluid mechanics, computer vision, and materials science*. Cambridge monographs on applied and computational mathematics ; 3. Cambridge University Press, Cambridge, 1996.

[45] J. A. Sethian and Peter Smereka. Level set methods for fluid interfaces. *Annual Review of Fluid Mechanics*, 35(1):341–372, January 2003.

[46] Stanley Osher and James A Sethian. Fronts propagating with curvature-dependent speed: Algorithms based on Hamilton-Jacobi formulations. *Journal of Computational Physics*, 79(1):12–49, 1988.

[47] Chun Liu and Jie Shen. A phase field model for the mixture of two incompressible fluids and its approximation by a fourier-spectral method. *Physica D: Nonlinear Phenomena*, 179(3):211–228, 2003.

[48] J. Lowengrub and L. Truskinovsky. Quasi-incompressible Cahn-Hilliard fluids and topological transitions. 454(1978):2617–2654, October 1998.

[49] David Jacqmin. Calculation of two-phase Navier-Stokes flows using phase-field modeling. *Journal of Computational Physics*, 155(1):96–127, 1999.

[50] G. Tryggvason, B. Bunner, A. Esmaeeli, D. Juric, N. Al-Rawahi, W. Tauber, J. Han, S. Nas, and Y.-J. Jan. A front-tracking method for the computations of multiphase flow. *Journal of Computational Physics*, 169(2):708–759, May 2001.

[51] S.O. Unverdi and G. Tryggvason. A front-tracking method for viscous, incompressible, multi-fluid flows. *Journal of Computational Physics*, 100(1), 1992.

[52] M. T. Mehrabani, M. R. H. Nobari, and G. Tryggvason. An efficient front-tracking method for simulation of multi-density bubbles. 84(8):445–465, July 2017.

[53] S. Dong. A time-stepping scheme involving constant coefficient matrices for phase-field simulations of two-phase incompressible flows with large density ratios. *Journal of Computational Physics*, 231(17):5788–5805, July 2012.

[54] S. Dong. On imposing dynamic contact-angle boundary conditions for wall-bounded liquid-gas flows. 247-248:179–201, November 2012.

[55] Lord Rayleigh. Xx. on the theory of surface forces. ii. compressible fluids. *The London, Edinburgh, and Dublin Philosophical Magazine and Journal of Science*, 33(201):209–220, 1892.

[56] J. Waals. The thermodynamic theory of capillarity under the hypothesis of a continuous variation of density. *Journal of Statistical Physics*, 20(2):200–244, 1979.

[57] John W. Cahn and John E. Hilliard. Free energy of a nonuniform system. i. interfacial free energy. *The Journal of Chemical Physics*, 28(2):258–267, 1958.

[58] V.E. Badalassi, H.D. Ceniceros, and S. Banerjee. Computation of multiphase systems with phase field models. *Journal of Computational Physics*, 190(2):371–397, 2003.

[59] E-mail: jinsong.hua@ife.no Hua Jinsong. Energy law preserving C0 finite element schemes for phase field models in two-phase flow computations. *Journal of Computational Physics*, 230(19), 2011.

[60] Pengtao YUe. A diffuse-interface method for simulating two-phase flows of complex fluids. *Journal of Fluid Mechanics*, 515:293–318, September 2004.

[61] Sebastian Aland and Feng Chen. An efficient and energy stable scheme for a phase-field model for the moving contact line problem. *International Journal for Numerical Methods in Fluids*, 81(11):657–671, August 2016.

[62] Yuezheng Gong, Jia Zhao, and Qi Wang. Second order fully discrete energy stable methods on staggered grids for hydrodynamic phase field models of binary viscous fluids. *SIAM Journal on Scientific Computing*, 40(2):528–553, 2018.

[63] Jie Shen and Xiaofeng Yang. Energy stable schemes for Cahn-Hilliard phase-field model of two-phase incompressible flows. *Chinese Annals of Mathematics, Series B*, 31(5):743–758, 2010.

[64] Pengtao Yue, Chunfeng Zhou, and James J Feng. Sharp-interface limit of the cahnhilliard model for moving contact lines. *Journal of Fluid Mechanics*, 645:279–294, 2010.

[65] J Argyris. Energy theorems and structural analysis: A generalized discourse with applications on energy principles of structural analysis including the effects of temperature and non-linear stress-strain relations. *Aircraft Engineering and Aerospace Technology*, 26(11):383–394, 1954.

[66] G. Karniadakis and S.J. Sherwin. *Spectral/hp Element Methods for Computational Fluid Dynamics: Second Edition*. OUP Oxford, 2005.

[67] Anthony T Patera. A spectral element method for fluid dynamics: Laminar flow in a channel expansion. *Journal of Computational Physics*, 54(3):468–488, 1984.

[68] B. A. (Barna Aladar) Szabo. *Finite element analysis*. Wiley, New York, 1991.

[69] N.B. Edgar and K.S. Surana. On the conditioning number and the selection criteria for p-version approximation functions. *Computers and Structures*, 60(4):521–530, 1996.

[70] R. Abdul-Rahman and M. Kasper. Higher order triangular basis functions and solution performance of the CG method. *Computer Methods in Applied Mechanics and Engineering*, 197(1):115–127, 2007.

[71] X. Zheng and S. Dong. An eigen-based high-order expansion basis for structured spectral elements. *Journal of Computational Physics*, 230(23):8573–8602, 2011.

[72] S.J. Sherwin and G.E. Karniadakis. A triangular spectral element method; applications to the incompressible Navier-Stokes equations. *Computer Methods in Applied Mechanics and Engineering*, 123(1):189–229, 1995.

[73] S. Dong, G.E. Karniadakis, and C. Chryssostomidis. A robust and accurate outflow boundary condition for incompressible flow simulations on severely-truncated unbounded domains. *Journal of Computational Physics*, 261(C):83–105, March 2014.

[74] O. A. (Olga Aleksandrovna) Ladyzhenskaia. *The mathematical theory of viscous incompressible flow.* Mathematics and its applications (Gordon and Breach Science Publishers) ; v. 2. Gordon and Breach, New York, rev. english ed.. edition, 1963.

[75] Ivo Babuka. The finite element method with Lagrangian multipliers. *Numerische Mathematik*, 20(3):179–192, June 1973.

[76] J. L. Guermond and L. Quartapelle. On stability and convergence of projection methods based on pressure Poisson equation. *International Journal for Numerical Methods in Fluids*, 26(9):1039–1053, May 1998.

[77] C H K Williamson. Vortex dynamics in the cylinder wake. *Annual Review of Fluid Mechanics*, 28(1):477–539, 1996.

[78] C Wieselsberger. New data on the laws of fluid resistance, 1922.

[79] Norman E Sorensen and Noel K Delany. Low-speed drag of cylinders of various shapes, 1953.

[80] R. K. Finn. Determination of the drag on a cylinder at low Reynolds Numbers, language = eng. *Journal of Applied Physics*, 24(6):771–773, 1953.

[81] D. J. Tritton. Experiments on the flow past a circular cylinder at low Reynolds numbers. *Journal of Fluid Mechanics*, 6(4):547567, 1959.

[82] Anatol Roshko. Experiments on the flow past a circular cylinder at very high Reynolds number. *Journal of Fluid Mechanics*, 10(3):345356, 1961.

[83] D. M. Anderson, G. B. McFadden, and A. A. Wheeler. Diffuse-interface methods in fluid mechanics. *Annual Review of Fluid Mechanics*, 30(1):139–165, 1998.

[84] S. Dong. An efficient algorithm for incompressible n-phase flows. *Journal of Computational Physics*, 276(C):691–728, 2014.

[85] E. Nogueira and R. Cotta. Heat transfer solutions in laminar co-current flow of immiscible liquids. *Wrme - und Stoffbertragung*, 25(6):361–367, November 1990.

[86] Pierre-Gilles de Gennes. *Capillarity and Wetting Phenomena Drops, Bubbles, Pearls, Waves.* 2004.